12-2022

The Characterization Of Natural Ingredients As Pharmaceutical Excipients In Paracetamol Tablets

Nigel Patrick Brooks Jr

THE CHARACTERIZATION OF NATURAL INGREDIENTS AS PHARMACEUTICAL EXCIPIENTS IN PARACETAMOL TABLETS

A Thesis

By

NIGEL PATRICK BROOKS JR.

Submitted to the Office of Graduate Studies of
Prairie View A&M University
in Partial fulfillment of the requirements of the degree of

MASTER OF SCIENCE IN ENGINEERING

December 2022

Major Subject: Chemical Engineering

THE CHARACTERIZATION OF NATURAL INGREDIENTS AS PHARMACEUTICAL EXCIPIENTS IN PARACETAMOL TABLETS

A Thesis

By

NIGEL PATRICK BROOKS JR.

Submitted to the Office of Graduate Studies of
Prairie View A&M University
in Partial fulfillment of the requirements of the degree of

MASTER OF SCIENCE IN ENGINEERING

Approved as to style and content by:

Dr. Sheena M. Reeves
Chair of Committee

Dr. Kazeem Olanrewaju
Committee Member

Dr. Merlyn Pulikkathara
Committee Member

Dr. Nabila Shamim
Committee Member

Assoc. Dean, College of Engineering

Dr. Pamela Obiomon
Dean, College of Engineering

December 2022

Major Subject: Chemical Engineering

ABSTRACT

The Characterization of Natural Ingredients as Pharmaceutical Excipients in Paracetamol Tablets.

(December 2022)

Nigel Brooks Jr, B.S. in Chemical Engineering, Prairie View A&M
University, Prairie View, Texas, United States
Chair of Advisor Committee: Dr. Sheena M. Reeves

Excipients used in pharmaceuticals are inactive ingredients that play a big role in drug formulations, and drug delivery systems. Binders are a type of pharmaceutical excipient that is crucial to the stability, physical characteristics, and cohesiveness of the tablet. Fully synthetic binders, such as polyethylene glycol (PEG), are commonly used due to their great formulation traits; however, these materials may have a slow dissolution rate, reduced bioavailability, or the potential to cause allergic reactions. Due to these limitations, natural excipients would be a great alternative due to their biocompatibility and faster dissolution rate. The purpose of this research was to characterize natural ingredients including d-sorbitol, d-allulose, tamarind gum, xanthan gum, guar gum, and pectin as pharmaceutical excipients with active pharmaceutical ingredient (API) paracetamol (APAP, acetaminophen). One excipient is used per tablet formulation with APAP to determine the influence on tablet characteristics. Another purpose of the research is to develop a better method for the formulation of 325 mg tablets. APAP tablets are created through wet granulation within 3D-printed molds, before being left to dry in a desiccant cabinet. After drying the tablets are characterized through image analysis with image pro software, dissolution using the BIO-DIS reciprocating Cylinder Apparatus, disintegration using 100 Disintegration Apparatus, Fourier-transform infrared spectroscopy (FTIR) absorbance accomplished with the Cary 630 FTIR, thermal stability with the Mettler Toledo DSC 3 STARe System, and crystal structure analysis with the XRD-7000 X-Ray Diffractometer Maxima. It has been concluded that natural excipients are compatible with APAP within the tablet matrix. 3D molds were an effective medium to produce granules through wet granulation due to the method's efficiency and yielding granules with consistent shapes. Sugar excipients were found to have a rapid disintegration time compared to polysaccharides and synthetic PEG. The dissolution test found that all the excipients except for xanthan gum had a faster rate of dissolution than PEG. Natural excipients also have little effect on APAP’s crystal structure and melting point temperature shown through XRD and DSC respectively. FTIR analysis has shown that natural excipients will have less of an impact on APAP’s structure than synthetic PEG.

DEDICATION

I would like to dedicate my thesis to my parents Mr. Nigel Brooks Sr. and Mrs. Latonya Brooks, my fiancée Carrie Conton, my brother Adonis Brooks, and Zipporah Williams who is like a sister to me, for their unfaltering support throughout my undergraduate and graduate career. If it was not for them, I would not be the man I am today.

ACKNOWLEDGMENTS

I would like to give my deepest and foremost thanks to God who has guided me on my graduate journey. I am also extremely grateful for Dr. Sheena M. Reeves, who has been my teacher, mentor, and thesis advisor. Giving me countless feedback, revisions, and unparalleled support throughout my research and graduate studies.

I would also like to thank Dr. Nabila Shamim, who has allowed me to use her lab and DSC equipment, offered me valuable advice, and is also on my defense committee. I am also thankful to Dr. Kazeem Olanrewaju, and Dr. Merlyn Pulikkathara for being on my defense committee and for their patience.

Many thanks to my colleagues who have supported me throughout the research. Berenice Rincon who designed the 3D molds and offered her knowledge of 3D printing, my brother Adonis Brooks for adding me by creating granules and compression test, and Sharnice Jones who also helped me create granules.

Lastly, I would like to acknowledge my family and friends who have been my greatest supporters. My parents Mrs. Latonya Brooks and Mr. Nigel Brooks Sr. have made me into the person that I am today. I appreciate their constant loving guidance, and for helping me keep my end goal in sight. My fiancée Carrie Conton helped me push through the toughest moments and kept me afloat. My brothers Adonis Brooks and Zee gave their constant never-ending support. My friends Daisaku Gicheha and Lashavio Little gave their moral support.

NOMENCLATURE

A, B, C	Coefficients of the Approximate Formula
A_b	Absorbance
APAP	Paracetamol
API	Active Pharmaceutical Ingredient
b	Integral Width of the Peak
C	Concentration of the Drug in the Bulk Solution
C_o	Initial Concentration of Drug in Solution
C_s	Concentration of the Drug in the Stagnant Layer
d	Spacing Between Planes of Atoms
DA	D-Allulose
dC/dt	Rate of Dissolution with respect to Concentration
D*hkl*	Represents the Particle Size Perpendicular to the hkl plane
DPM	Dips per Minute
DS	D-Sorbitol
DSC	Differential Scanning Calorimeter
dW/dt	Dissolution Rate of the Drug with respect to Weight
E_{vib}	Energy of the Vibration Levels of the Molecule

FTIR	Fourier-Transform Infrared Spectroscopy
GG	Guar Gum
h	Plank’s Constant
K	Dissolution Rate Constant
K_o	Zero Order Release Constant
K_S	Scherrer’s Constant
K_X	X-Ray Scattering
l	Power Transmitted by a Sample
l_a	Amorphous Intensity of the Sample
l_{cr}	Integral Intensity of the Sample
l_o	Radiant Power Incident on the Sample
l_o	Uncorrected Data Intensity
M_a	Amorphous Part of the Sample
M_{cr}	Crystalline Part of the Sample
M_o	Initial mass of the Tablet
M_t	Mass of the Tablet at time t
M_t/M_∞	Fraction of the Drug that Permeated into the Solution.
n	Integer

n_v	Vibrational Quantum Number
PC	Pectin
PEG	Polyethylene Glycol
PVP	Polyvinylpyrrolidone
Q_o	Initial Amount of Drug in the Solution at the start of Dissolution
Q_t	Amount of Drug Dissolved at Time t
R_{th}	Thermal Resistance of Sensor
T	Transmittance
t	Time of Dissolution
T_c	Oven Temperature
TM	Tamarind Gum
T_r	Reference Temperature
T_s	Sample Temperature
v	Vibrational Frequency
X	Crystalline Part of the Sample
XN	Xanthan Gum
XRD	X-Ray Diffraction
B	Integral Width

η	Grating Distortion
θ	Angular Position of the X-Ray Beam
θ_m	Bragg’s Angle of the Monochromator
λ	Wavelength of the X-Ray
φ	Heat Flow Given by DSC
φ_l	Heat Flow on Left Side of Plate
φ_r	Heat Flow on Right Side of Plate
$\boldsymbol{\varepsilon}$	Average Size of Crystal Particles

TABLE OF CONTENTS

CHAPTERS

LIST OF FIGURES

FIGURE **PAGE**

LIST OF TABLES

1. INTRODUCTION

Excipients are used in a variety of fields including powder technology and pharmaceuticals. Excipients are classified as either natural, semi-natural, or synthetic. In the pharmaceutical industry, excipients have a wide range of applications including binders, adhesives, and sweeteners in tablet formulations. In recent years, the solubility of synthetic excipients has decreased due to the increased complexity of the material. To achieve an improved, biocompatible status, a potential binding material must not cause an inflammatory or toxic response once inside the human body. Biocompatibility is important because this characteristic describes how easily the body can dispose of the excipient and reduce the chances of negative side effects caused by allergic reactions. The binding material must also have an acceptable shelf-life. To meet the standard requirements and improve upon these flaws, natural excipients are under consideration. Natural excipients are readily available and are produced more economically than certain synthetic materials. Natural excipients are also inert and do not interfere with the effectiveness of the active pharmaceutical ingredient or API.

The use of food-based materials, such as polysaccharides and monosaccharides in the pharmaceutical industry, has seen a steady increase in the past few years. Literature has shown the advantages of using natural polysaccharides and monosaccharides in tablet formulations due to improved biocompatibility. However, more studies are needed to determine the overall influence of individual excipients on tablet performance. An

---

This thesis follows the style of *Journal of Materials Science: Materials in Medicine* understanding of how the excipients interact with the API is important to establish better drug formulations and overall interactions in the future. This study investigated the overall performance of natural excipients in developing tablets of the API paracetamol (APAP). The overall research goals included:

1. Determining the effect of using various natural excipients to form APAP tablets.
2. Determining the effect of using a monosaccharide, sweetener versus a polysaccharide, gum as an excipient.
3. Determining the effect of increasing the amount of excipient dissolved in the liquid binders during drug formation.
4. Determining whether natural excipients are sufficient replacements for the synthetic binder polyethylene glycol (PEG)

The research goals were accomplished by completing the following tasks:

Task: 1. Developing a more efficient method for formulating 325mg APAP tablets.

Task: 2. Performing disintegration analysis by recording disintegration times.

Task: 3. Performing dissolution analysis and determining the dissolution characteristics of the APAP tablets.

Task: 4. Analyzing the crystal structure of the APAP tablets using X-ray diffraction (XRD).

Task: 5. Determining structural analysis using Fourier transform infrared spectroscopy (FTIR) to analyze how the excipients affect the chemical structure of APAP.

Task: 6. Performing thermal analysis using differential scanning calorimetry (DSC) to analyze how excipients affect the thermal characteristics of the APAP.

In Chapter 2, a literature review is provided with background information regarding tablet formulation and each tablet analysis method. Chapter 3 highlights the different materials, instruments, and methods used while completing Tasks 1 - 6. Chapter 4 details the experimental results and discusses applicable trends and correlations seen in the data. Chapter 5 supplies a summary of all conclusions concerning the overall research goals.

2. LITERATURE REVIEW

2.1 Tablet Formation Process

Granulation, which is a type of agglomeration, is a size enlargement process where smaller particles come together to form larger granules [1]. In this process, the small particles are still identifiable in the larger granule since no chemical reaction is taking place. Granulation is an important process in any industry where particulate solids are produced, especially in the pharmaceutical, food, and agricultural industries [2]. Industrial granulation utilizes processes that specialize in particle agglomeration using agitation or compression methods. Industrial processes are usually in the form of batch or continuous processes that include fluid bed, drum, mixer granulators [2], compression, and extrusion equipment [3]. The feed of these processes includes the active pharmaceutical ingredient (API) in the form of a fine powder and other key ingredients such as lubricants, fillers, surfactants, flow aids, and even taste modifiers. Wetting agents and binders are also introduced in the feed that is responsible for the wet granulation process. After successful granulation, the granules are normally tableted into a final product through compression [2] as shown in Figure 1.

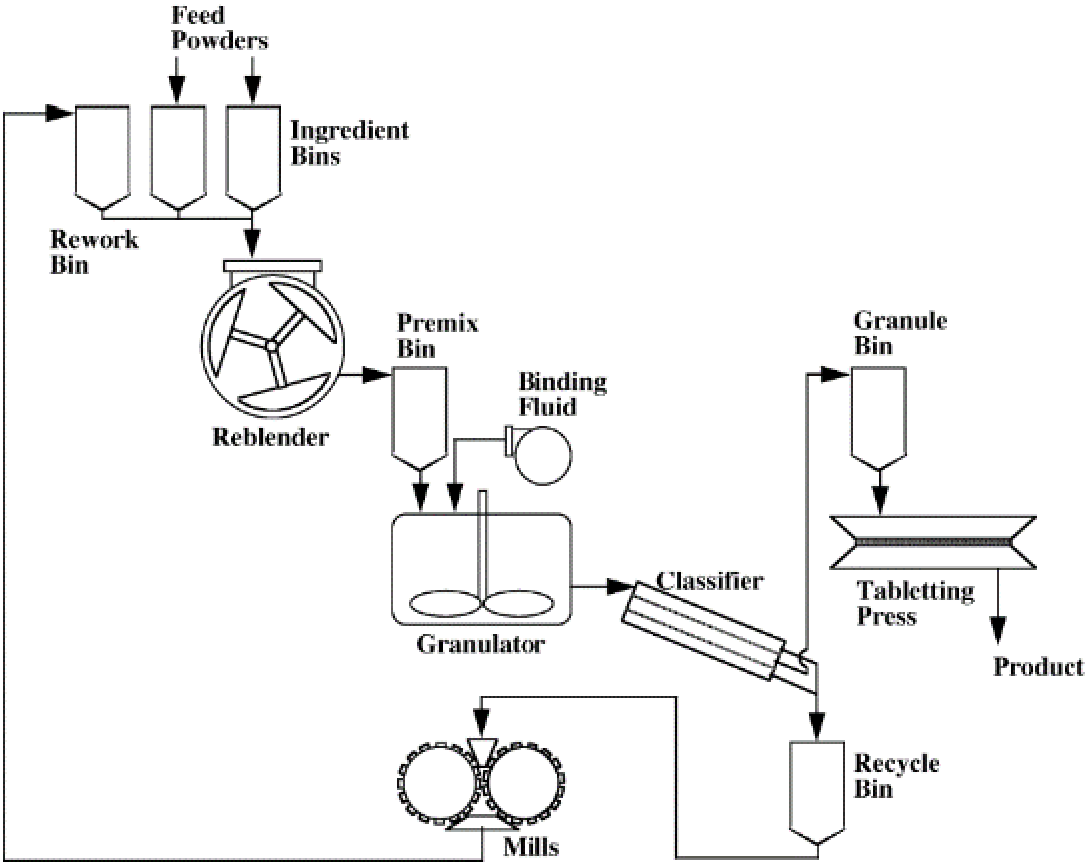

Figure 1: Agglomeration Circuit involving Granulation and Compression [2]

During the granulation process, the original particles are still distinguishable since wet granulation is not a chemical reaction. Instead, the particles are simply rearranged with stronger intermolecular bonds [2]. The wet granulation method utilizes a liquid binder solution that is applied to solid particles, initiating the granulation process [1]. As the liquid solution evaporates, the solid binder within the original solution cements the particles together forming a granule as shown in Figure 2. The wet granulation process follows multiple steps that utilize interparticle forces including wetting and nucleation, coalescence, consolidation, and breakage [1]. These steps are depicted in Figures 3 – 5.

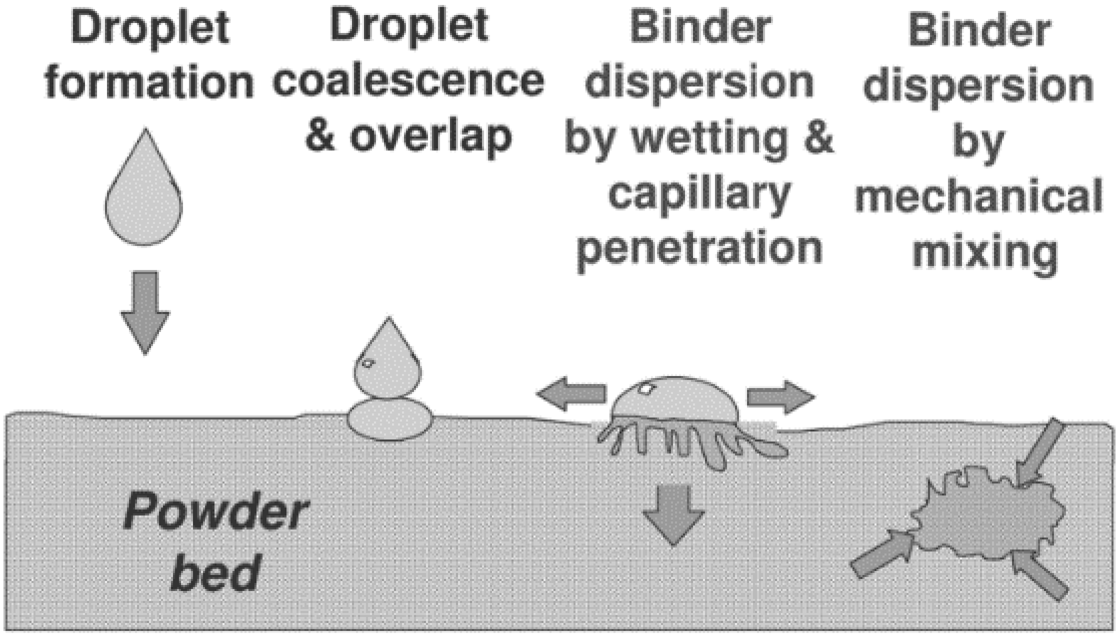

Figure 2: Wet Granulation Method [4]

2.2 Wetting and Nucleation

Wetting and nucleation are important steps that would decide the success of wet granulation shown in Figure 3. The binder solution is responsible for wetting the powdered drug to initiate the granulation process, where air voids between particles are replaced by the binder solution [1]. For industrial processes where mixers and other agitators are involved, the binder solution must have the strength to resist the forces of agitation. In situations where agitation is unable to distribute the liquid binder, or solid-liquid forces are not strong enough, the powder is immersed in the liquid binder droplets [3]. When the liquid binder evaporates, the solid-liquid bridges replace the liquid-liquid bridges between particles. In this case, the size of the liquid drop is important, whereas, in a high-shear mixer, agitation is responsible for spreading the liquid binder. Nucleation involves the liquid bridges that form capillary forces between particles once they are wetted which is influenced by the binder [2]. The resulting surface tension pulls the particles together forming an agglomerate partial which is also known as nuclei. There are three regimes of nucleation including drop-controlled, intermediate, and mechanical dispersion [1]. Drop controlled occurs at low spray flux and fast penetration time of the drops. At low spray flux, the spray solution has a low density, and there is a small chance of droplets overlapping. Fast penetration is the result of the drops penetrating the powder bed before touching new drops from the sprayer. With higher penetration time and spray flux, mechanical dispersion is needed. This is usually the case for viscous and poor-wetting binders. The Intermediate regime exists between drop-controlled and mechanical dispersion regimes [1].

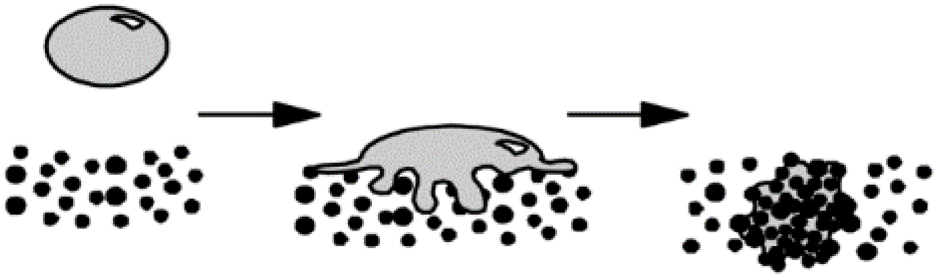

Figure 3: Wetting and Nucleation stage of Wet Granulation [4]

2.3 Coalescence and Consolidation

Coalescence is a factor that plays a part in molecular interactions during granule formation caused by colliding agglomerates shown in Figure 4. When the agglomerates collide, a molecular bond is formed between the particles at the area of contact [1]. The molecular force must also be stronger than the moment of the particles caused by mass and velocity influences. Fine particles with a wide, size distribution will have higher agglomerate strength because of the increased chance of particle collisions. To increase the chance of coalescence the presence of free liquid is necessary to increase the liquid surface area on the particles during granulation [3]. Consolidation during the granulation process takes place during the evaporation of the liquid binder [1]. The evaporation of the liquid binder leads to an increase in surface tension and capillary pressure. The characteristics of the particle and the amount of liquid have a significant role in how consolidation takes place [3]. When the particles are immersed in the liquid binder, the particles have the freedom to move around leading to improved packing configurations. The freedom to move leads to strengthen molecular bonding during the consolidation process. The particle characteristics including the size distribution, shape, and roughness affect the rate of consolidation [3].

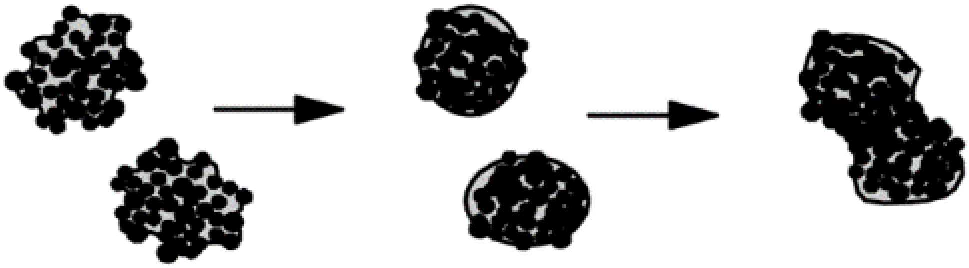

Figure 4: Particle collision and coalescence [4]

2.4 Attrition and Breakage

Breakage, a principal factor in high-shear granulators, occurs when a granule breaks in a granulator. Attrition occurs when dried granules fracture within the granulator, drier, or during handling of the granule shown in Figure 5 [4]. Breakage is controlled through changes in the granulation process including choice of binder, agitation intensity, and other factors [1]. However, breakage has not been studied in wet granulation as much as nucleation and granule growth. Attrition is a principal factor when granulation and drying are occurring at the same time, especially in wet granulation. Factors affecting attrition include fracture toughness, structural flaws, and crack size in the granule [4].

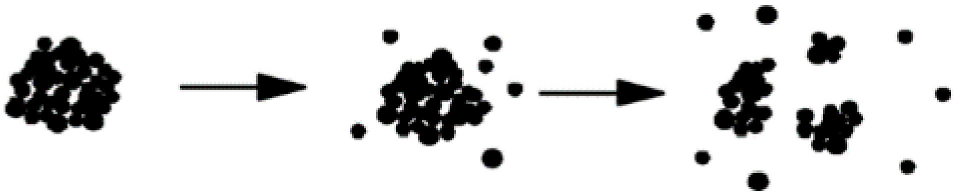

Figure 5: Granule Attrition and Breakage

2.5 Interparticle Forces

Granulation depends on key interparticle interactions in the formation process, including van der Waals forces, absorbed liquid layers, liquid bridges, electrostatic forces, and solid bridges. These forces are not chemical reactions but physical interactions between molecules, where each molecule is still identifiable after granulation. Interparticle forces are the core of the granulation process allowing smaller particles to come together to form larger masses.

2.5.1 Van der Waals Forces

Van der Waals force is an attractive force that exists between all solids and has a larger range than a chemical bond [1]. The force plays a significant role in solid surface interactions and interparticle adhesion in fine particles. The van der Waals forces influence the tablet's tensile strength and viscoelasticity during deformation [5].

2.5.2 Absorbed Liquid Layers Forces

When solid particles encounter a vapor, a thin liquid film is formed on the surface. Bonding forces between two particles in the vapor will be the result of the overlapping liquid films on the particle's surface [1]. The strength of the bond between two absorbed liquid layers is based on the contact between two liquid films and the resulting tensile strength due to the contact. The partial pressure of the vapor can influence the thickness of the liquid films, which would result in a stronger interarticular force due to increased contact. At a specific critical partial pressure, the absorbed liquid film would then lead to the formation of liquid bridges [1].

2.5.3 Liquid Bridges Forces

Liquid bridges are responsible for improving the interparticle forces by smoothing out imperfections on the particle surfaces through thin liquid films [1]. Solid bridges form on an atomic level between two particle surfaces with a range of 1 nm [6] therefore, increasing particle surface contact with one another. There are four types of liquid states (Figure 6) that are associated with liquid bridges including pendular, funicular, capillary, and droplet states [1]. Pendular state liquid bridges are individually defined between particles, due to the bridges being independent of one another. A funicular state on the other hand has an increased amount of liquid compared to a pendular state resulting in a decrease of voidage between particles. The funicular state also has a smaller force of attraction than a pendular state due to the decrease in voidage. In a capillary state, there is enough liquid to fill any voidage resulting in zero clearly defined liquid bridges, unlike in pendular and funicular states. The granule strength is weaker in a capillary than in pendular and funicular states due to the lack of liquid films on the solid particle surface for interarticular forces to act on. In the case of a droplet state, there is no liquid film on the solid surface due to the particles engulfed by the liquid, resulting in low levels of attraction between particles [1].

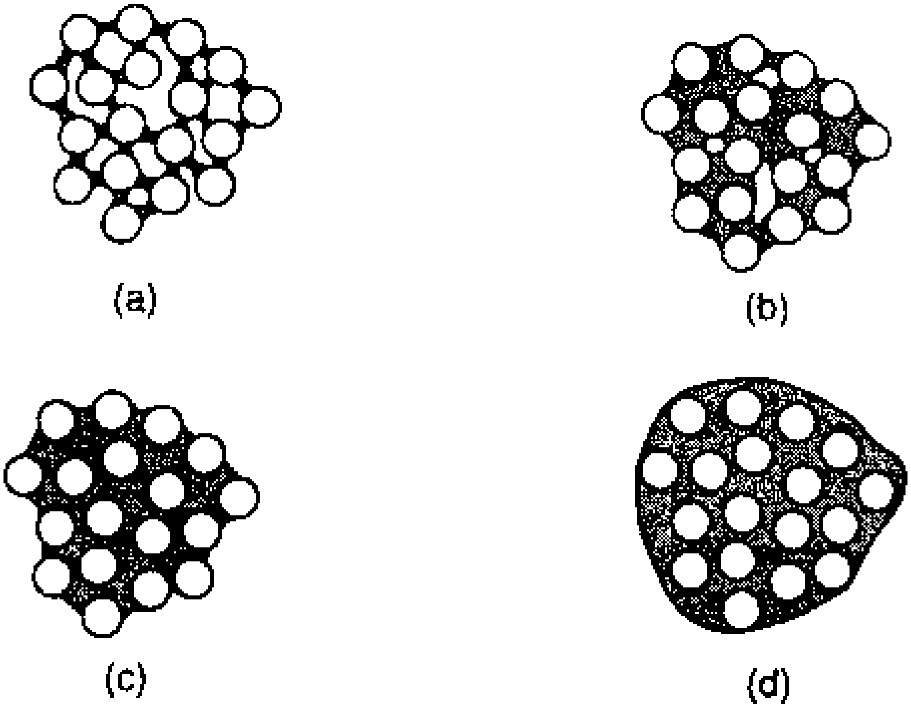

Figure 6: Liquid Bonding Types: Pendular (A); Funicular (B); Capillary (C); Droplet (D)

2.5.4 Electrostatic Forces

Electrostatic forces between particles are due to friction and collision between each other and the equipment resulting in charged particles due to moving electrons. Once the charge is formed, contact is not needed between particles for the force to be active. Electrostatic forces also have a longer range then forces due to adhesion, where a stronger charge results in a stronger force [1].

2.5.5 Solid Bridge Forces

Solid bridges form as liquid bridges evaporate, resulting in a more permanent bonding at the end of granulation [1]. Solid bridges can be classified as crystalline, liquid, or solid binder bridges. For a crystalline bridge to form, the particles need to be soluble in the liquid that the particle is in [1]. As the liquid evaporates from the liquid bridges, high-strength pendular bridges are formed before the formation of crystals. The liquid used in granulation could also contain a liquid or solid binder that acts like glue that takes effect as the solvent evaporates. When a solid binder is used in the liquid solution, the binder will act as cement to hold the particles together as the solvent evaporates [1].

2.6 Ingredients in Pharmaceuticals

The use of natural ingredients has been increasing over the last few years in pharmaceutical and other industries since these materials are usually biocompatible, economically friendly, easily accessible, and non-toxic. Excipients are an important factor in wet granulation and are typically used as binders, adhesives, and sweeteners in tablet formulations [7]. As formulations have become more advanced, so have synthetic excipients including polyvinyl pyrrolidone (PVP) and polyethylene glycol (PEG). Synthetic binders are known for having physical and chemical stability; however, the binders may cause cytotoxicity and bio-incompatibility [8]. Due to the bio-incompatibility of synthetic excipients, they have a chance of causing side effects including skin irritations and other allergic reactions [8]. Synthetic excipients are complex causing them to have a high cost when compared to natural excipients [7] [8]. The use of natural excipients will aid in improving the solubility of poorly soluble drugs and improving bioavailability [9].

Two materials are considered for this thesis – sweeteners, and gums. Natural polysaccharides are formed from monosaccharides linked together by O-glycosidic linkages. Gums are known as a type of polysaccharide that is extracted from plants including the seed epidermis, leaves, and plant bark [8]. Gums also have hydrophilic molecules that form gel-like hydrocolloid solutions when in the presence of water [8]. Some gums greatly increase the viscosity of a solution at small concentrations [10]. Polysaccharides have a wide range of uses in the pharmaceutical industry, including granule coatings, tablet formulations to target the gastrointestinal tract [9], thickeners, emulsifiers, suspending agents, and wound-healing agents [10]. Sweeteners are monosaccharides that are also used in the pharmaceutical, food, and cosmetic industries. Monosaccharides are primarily used as stabilizing agents, sweetening agents, plasticizers, and tablet diluents [11]. Chemicals used in the research are shown in Table 1 with chemical properties.

Table 1: Chemical Data Table

Binder	Abbreviation	Type	Formula	Molecular Weight	Density (g/cc)	Reference
Polyethylene Glycol	PEG	Synthetic	$HO(CH_2CH_2)_n$-H	~8000	1.13	[12]
Xanthan Gum	XN	Natural	$(C_{35}H_{49}O_{29})_n$	933.7	1.5	[13]
Pectin	PC	Natural	$(C_7H_{10}O_7)_n$	20,000 – 400,000	~	[14]
Guar Gum	GG	Natural	$(C_6H_{12}O_6)_n$	50,000-8,000,000	~	[15]
Tamarind Gum	TM	Natural	~	720 – 880 x 10^3	~	[16] [17]
D-Allulose	DA	Natural	$C_6H_{12}O_6$	180.16	1.59	[18] [19]
D-Sorbitol	DS	Natural	$C_6H_{14}O_6$	182.2	1.49	[11]

2.6.1 Acetaminophen (APAP)

Acetaminophen ($C_8H_9NO_2$) also known as paracetamol (APAP) is an API primarily used in pain [20] [21], and fever-reducing medications [22]. More specifically, in minor to moderate pain in non-inflammatory conditions, due to APAP's ineffectiveness to reduce swelling. APAP is also recommended for patients that are prone to cause gastric damage and coagulation disorder. Paracetamol was first synthesized in 1878 by Morse [23], because the drug was believed to have been less toxic than phenacetin which was a competing drug at the time. However, paracetamol was not widely used until the 1950s to replace phenacetin although its usage was discouraged due to its discovered nephrotoxicity [23]. Paracetamol is believed to function by inhibiting the enzyme COX-3 [24], which is responsible for regulating pain responses and fever in the brain [25]. The chemical structure of APAP is shown below in Figure 7, consisting of hydroxyl, amide, and aromatic function groups. Hydrogen bonding between the hydroxyl groups and oxygen atom on the carbonyl group is responsible for APAP's chemical structure [26]. Other hydrogen bonds between the nitrogen and the hydroxyl group also influence the crystal structure, resulting in folded layers for form I, or flat layers for form II of APAP. Form I is the more stable form (and what is observed in this paper), and form II is a less stable form [26].

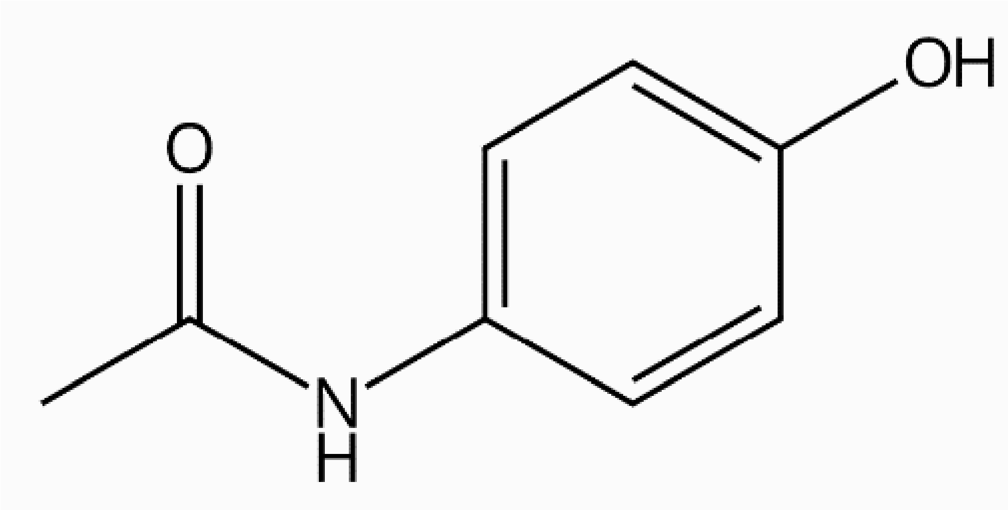

Figure 7: APAP Chemical Structure

2.6.2 Polyethylene Glycol (PEG)

PEG ($\mathrm{H(OCH_2CH_2)_nOH,}$) (Figure 8) is a fully synthetic binder that is used as a plasticizer, solvent, tablet/capsule lubricant, and suppository base in the pharmaceutical industry [12]. PEG is applied to a wide variety of drug formulations including topical, oral, and rectal preparation. In addition to the current use of PEG, it was included in experiments for controlled-release systems using biodegradable polymeric matrices. PEG is also known to enhance the solubility and dissolution of poorly soluble drugs, and for its stability [12].

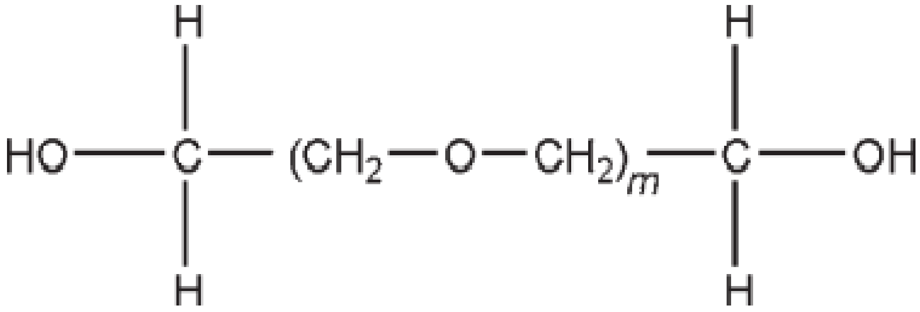

Figure 8: PEG Molecular Structural Formula [12]

2.6.3 D-Sorbitol

D-sorbitol ($C_6H_{14}O_6$) (Figure 9) is a sugar-free sweetener and well-known linear sugar alcohol [27]. D-sorbitol is also known as D- glucitol, which is a D-enantiomer of glucitol [28]. D-sorbitol contains 60% sweetness of sucrose with only two-thirds of the calories [27]. The sweetener is also used as a tablet and capsule diluent, humectant, plasticizer, and excipient in pharmaceutical formulations [11]. Sorbitol is found in a wide range of fruits and is produced from the hydrogenation of d-glucose [27]. The chemical is also relatively inert and stable [27], making d-sorbitol compatible with other excipients and resistant to fermentation improving shelf life [11]. D-sorbitol was also found to enhance the dissolution of indomethacin. At elevated temperatures, sorbitol does not char and decompose when amines are present. Sorbitol is also very soluble in water and requires a preservative in an airtight container due to being hygroscopic. [11].

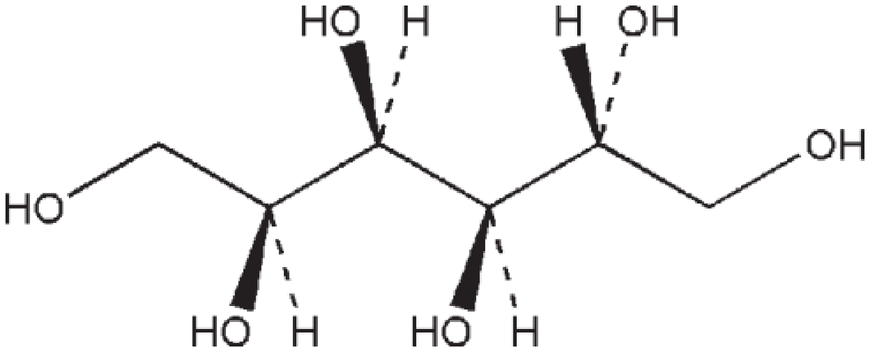

Figure 9: D-Sorbitol Chemical Structure [11]

2.6.4 Guar Gum

Guar gum $(C_6H_{12}O_6)_n$ (Figure 10) is a galactomannan polysaccharide that is extracted from the endosperms of *Cyamopsis tetragonolobus* (also known as the guar plant) grown in arid zones of India, Pakistan, Sudan, and the US [10]. Guar gum is typically used in the cosmetics, food, and pharmaceutical industries. The primary functions of guar gum include a suspending agent, disintegrant, tablet binder, and viscosity-increasing agent [15]. Guar gum is also used to create sustained-release matrix tablets to target specific locations in the colon and the gastrointestinal tract [29]. Guar gum will form colloidal solutions and hydrate in the presence of water, where small concentrations of the gum make highly viscous solutions [15]. The gum is formed of hydroxyl groups that are responsible for hydrogen bonding in aqueous solutions. Guar gum solutions need to be preserved with a preservative or be used in the first 24 hours [15].

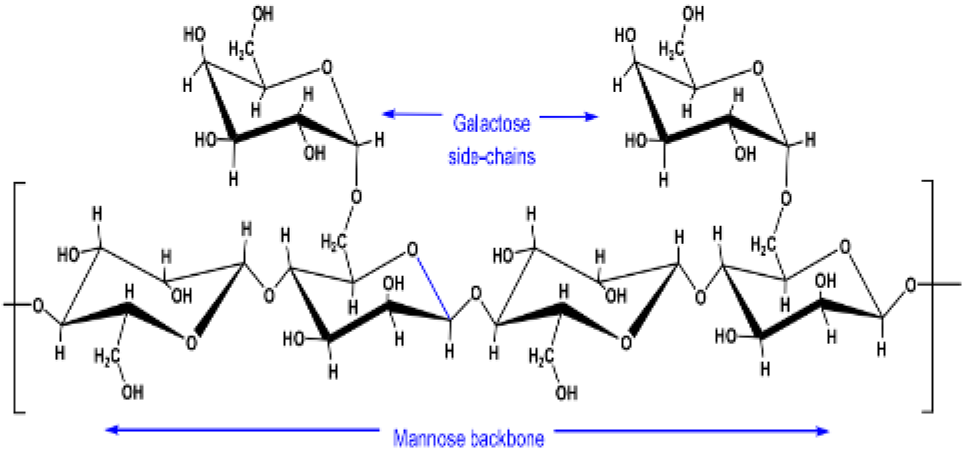

Figure 10: Guar Gum Chemical Structure [10]

2.6.5 Pectin

Pectin (Figure 11), a complex polysaccharide, is a primary component of a plant's primary cell wall and is obtained from citrus fruits and apple pomace. Pectin's structure consists of galacturonic acid chains linked as 1,4-α-glucosides and has a molecular weight between 30,000 Da and 100,000 Da. [30] [14]. In industry, pectin is used as a gelling agent, thickening agent, adsorbent, emulsifying agent, and stabilizing agent. In pharmaceuticals, pectin is used in formulations aimed at diarrhea, constipation, and obesity [14]. Experimentally, pectin has shown the ability to improve a tablet's drug release to target the gastrointestinal tract. [14].

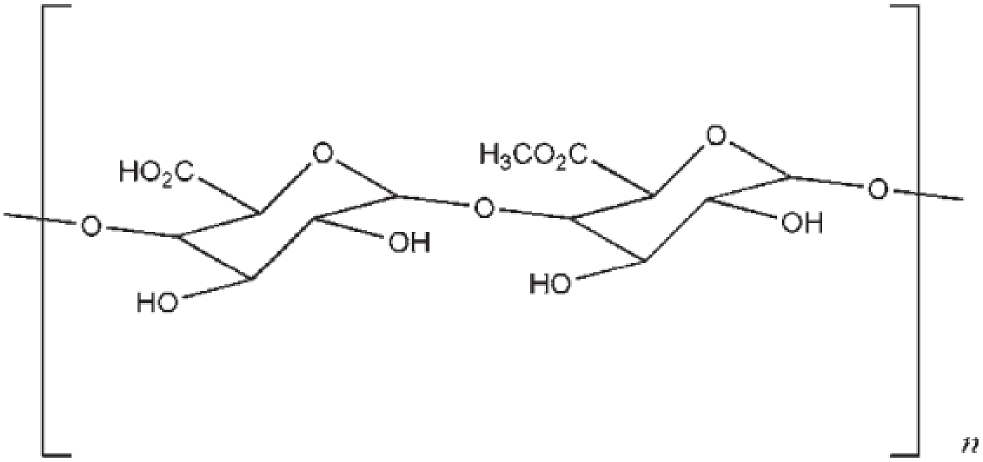

Figure 11: Pectin Chemical Structure [14]

2.6.6 Tamarind Gum

Tamarind gum (Figure 12) is a polysaccharide that is obtained from plant seeds from the Leguminosae family, found in Southeast Asia, India, Bangladesh, Myanmar, Sri Lanka, Thailand, and Malaysia. Tamarind gum consists of glucose, xylose, and galactose with a molecular ratio of 3:2:1 respectively per unit, where glucose forms the backbone of the chain. [16]. Tamarind gum is commonly used in the food and textile industry, but recent research shows that the gum is used in pharmaceutical formulations to control drug release. It is known that tamarind has a high swelling index, high thermal stability, and high drug-holding capacity, making the gum more desirable for drug delivery systems. Tamarind is soluble in water creating a viscous hydrocolloid solution. [17]. Tamarind gum has been applied to a wide range of applications in pharmaceuticals including the role of a stabilizes, thickener, viscosity enhancer, suspending agent, and emulsifying agent [17].

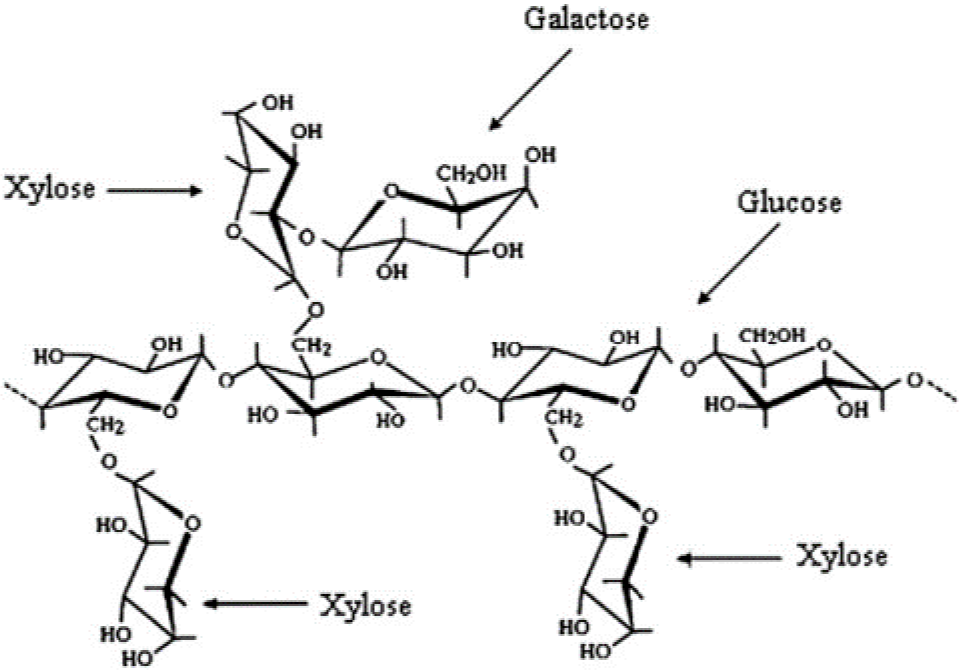

Figure 12: Tamarind gum chemical structure [16]

2.6.7 Xanthan Gum

Xanthan gum $(C_{35}H_{49}O_{29})_n$ (Figure 13) is a high molecular weight polysaccharide and is cultured from bacteria known as *Xanthomonas campestris*. Each unit of xanthan gum contains 5 sugar residues that consist of two glucose and mannose and one glucuronic acid. The two glucose sugars are responsible for the backbone of xanthan gum [13] [31]. Xanthan gum is used in the pharmaceutical, food, and cosmetics industries. Xanthan gum functions as a gelling, stabilizing, suspending, sustained release, and viscosity agent. When xanthan gum is combined with water a viscous hydrocolloid solution is formed that has pseudoplastic behavior. In tablet formulations, xanthan gum is used as a suspending agent, and to create sustained-release tablets [13].

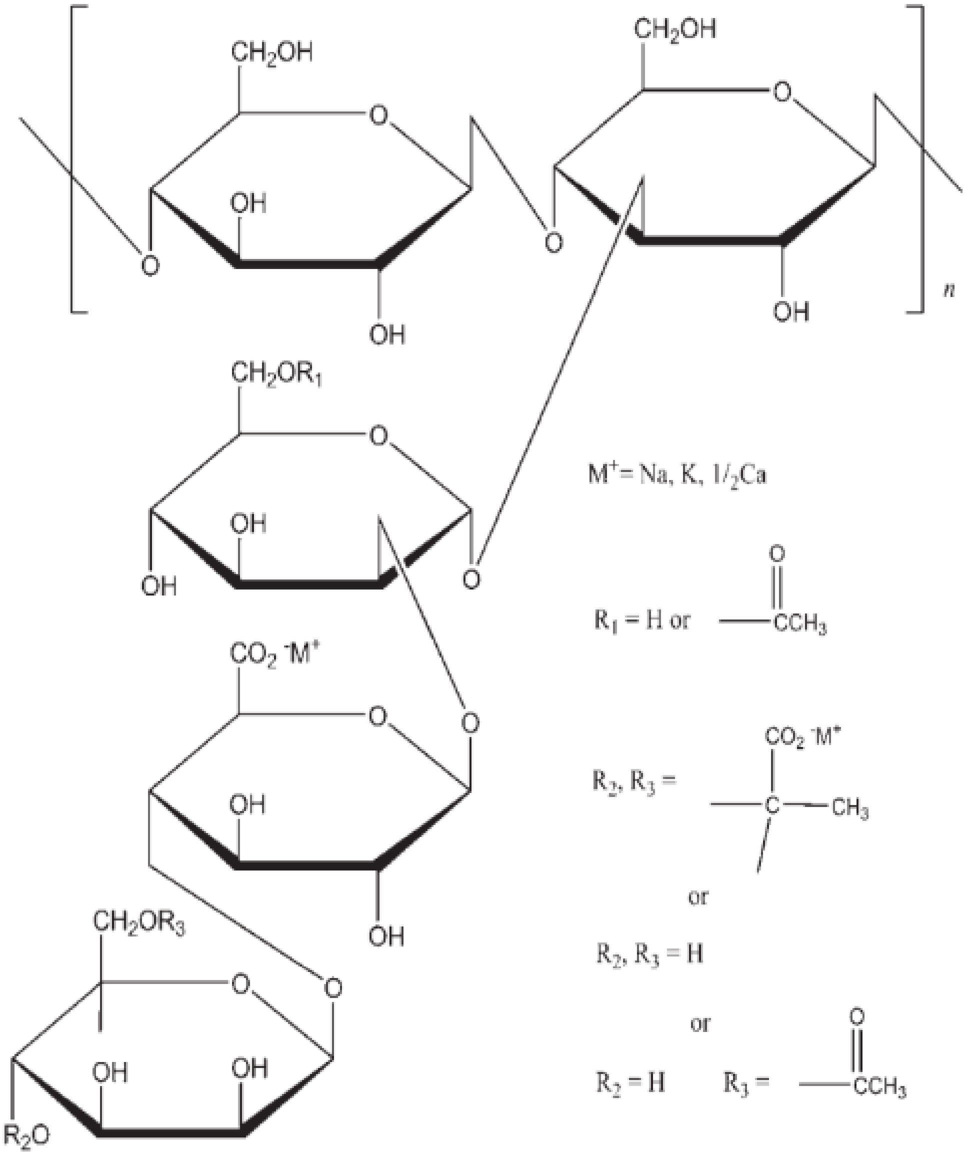

Figure 13: Xanthan Gum Chemical Structure [13]

2.6.8 D-Allulose

D-allulose ($C_6H_{12}O_6$) (Figure 14) is a monosaccharide sugar alcohol that is rarely found in nature in a few species including the Itea plant [18]. D-allulose is also capable of regulating physiological functions in the body including suppressing blood glucose elevation and reducing fat accumulation. While the sweetness of d-allulose is only 70%

sucrose, the calorie content is 0.4 kcal/g [18]. Research also found that d-allulose decreases sugar absorption in rats and increases insulin sensitivity in humans after taking maltodextrin [32]. The current use of d-allulose includes improving food gelling behavior and producing pleasant taste in the food industry.

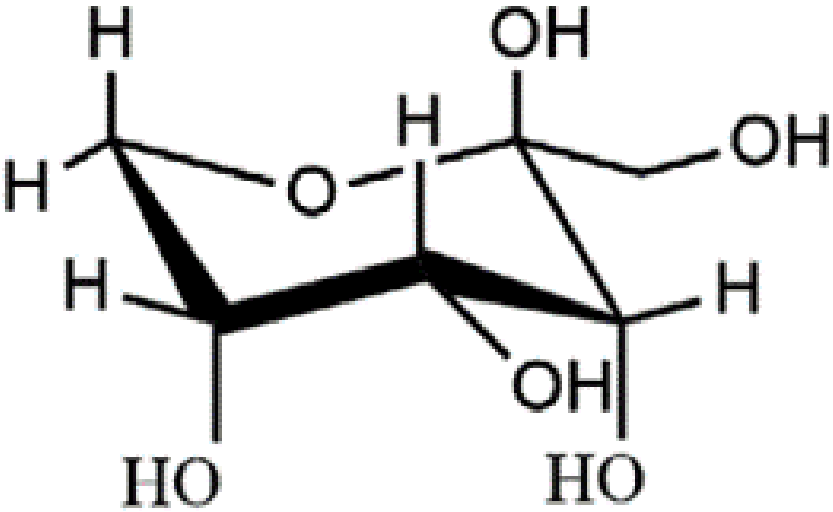

Figure 14: D-Allulose Chemical Structure [18]

2.7 Dissolution

Dissolution and solubility are both key factors for a pharmaceutical drug. Solubility is the ability of a solute to dissolve in a pure solvent, while dissolution is the process of the solute dissociating into a solvent. While both factors are related, solubility will not always reflect the dissolution rate and vice versa. For example, an elevated level of solubility with the solvent does not mean that the dissolution rate would be fast and vice versa. Solid-liquid solubility is important for pharmaceutical tablets and is important to understand the dissolution characteristics of the tablet. While the solid tablet is in the solvent, the tablet will break down into aggregates, and then into smaller segments of fine particles. At every level of breakage, dissolution will occur forming a solution [33].

2.7.1 Factors affecting Dissolution

The formulation of a drug has a strong effect on the dissolution characteristics. Gum excipients have been used to extend the period of dissolution, while others speed up the dissolution process. The tablet dissolution characteristics are due to the wet granulation process by modifying the crystal structure in the final production. The structures will fall under two categories including amorphous and crystalline structures. Amorphous structures have short-range atomic arrangements, only showing a particular order over a short distance (1 to 10Å). Crystalline structures on the other hand contain both short and long-range atomic arrangements, showing 3D patterns that repeat over long distances (10nm to cm). The amorphous form of hydrophobic tablet formulations is known to improv dissolution in aqueous media compared to the crystalline form. Unfortunately, amorphous structures lack the long-term stability and phase-transformation found in crystalline structures in pharmaceutical tablets. Due to this, crystalline structures are preferred over amorphous structures. In pharmaceutical tablets, formulations are considered eutectic mixtures because the molecules do not react chemically with one another. Therefore, how crystal structures interact with one another plays a large role in dissolution kinetics. These interactions form microstructures and interfacial disorders that enhance the drug’s dissolution rate [34] [35].

2.7.2 Dissolution Kinetic Models

Drug dissolution test is important to understand how solid and semisolid dosage drugs release over time, accomplished in an *in vitro* setting. Values gained from the dissolution experiments are then applied to dissolution kinetic models that are responsible for mathematically describing the dissolution process. Popular models include zero order, first order, the Hixon-Crowell cube root model, and the Korsmeyer-Peppas Model [36].

2.7.2i Zero Order Model

The zero-order model reflects drugs that release a constant amount of active ingredient with respect to time, which is ideal for drugs that require a prolonged drug release. The zero-order model is reflected by the following equation:

$$Q_t = Q_o + K_o t \qquad \text{Equation (1)}$$

where Q_t is the amount of drug dissolved in time t, Q_o is the initial amount of drug in the solution at the beginning of dissolution, K_o is the zero-order release constant. The model is plotted with the amount of drug released versus time. This model could be applied to drugs with transdermal systems, and with drugs that have low solubility, coated forms, and osmotic systems [36].

2.7.2ii First Order Model

The first-order model was developed to consider the surface action of dissolution. Noyes and Whitney developed a differential equation in 1897 that related the rate of dissolution on a solid surface to the concentration of solute from the surface to the solvent shown in the following equation:

$$\frac{dC}{dt} = K(C_s - C) \qquad \text{Equation (2)}$$

where $\frac{dC}{dt}$ is the dissolution rate of the drug, K is the dissolution rate constant, C_s is the concentration of the drug in the stagnant layer, and C is the concentration of the drug in the bulk solution. The equation was then modified by Brunner to include the solid area accessible to dissolution, and further modified by Hixson and Crowell to develop the following equation:

$$\frac{dW}{dt} = KS(C_s - C) \qquad \text{Equation (3)}$$

Where S is the solid area accessible to dissolution, and $\frac{dW}{dt}$ is the dissolution rate of the drug. Further modification results in the first-order equation shown below:

$$\ln\left(\frac{C_s}{C_o}\right) = Kt \qquad \text{Equation (4)}$$

2.7.2iii Hixon-Crowell Cube Root Model

The Hixon-Crowell model was designed to model dissolution based on the weight of the tablet. This is done by cube-rooting the mass of the tablet and comparing it to the rate constant multiplied by time as shown in the following equation:

$$M_o^{1/3} - M_t^{\frac{1}{3}} = kt \qquad \text{Equation (5)}$$

where M_o is the initial mass of the tablet, M_t represents the mass of the tablet at time t, k is the dissolution constant, and t is the time of dissolution [36].

2.7.2iv Korsmeyer-Peppas Model

The Korsmeyer-Peppas (K-P) model is commonly used with non-linear diffusion kinetics. Similar to the Hixon-Crowell model, the K-P model uses mass as a base for its formula as shown in the following equation:

$$\frac{M_t}{M_\infty} = Kt^n \qquad \text{Equation (6)}$$

Where $\frac{M_t}{M_\infty}$ represent the fraction of the drug that permeated into the solution, K is the transport constant, t is the time of dissolution, and n is the transport exponent that depends on the diffusional release mechanism [37] [36].

2.8 Disintegration

Disintegration is the disaggregation of a tablet into multiple particles and increases the solubility of APIs [38]. It is also used to study the mechanical breakup of a tablet during ingestion, and the breakdown of interparticle bonds formed during wet granulation [6]. Disintegration increases the surface area of a tablet for dissolution increasing the rate of dissolution. Therefore, it is important to know the disintegration characteristics of the tablet to understand the tablet's drug release. Disintegration characteristics controls whether the drug will be quickly released when in contact with bodily fluids or slow dissolve to target the gastrointestinal tract [6]. For disintegration to occur, a force needs to be stronger than the intermolecular forces that can overcome the interparticle forces [6] [38]. Some natural polysaccharides are slightly soluble, increasing the viscosity of a penetrating medium, and slowing disintegration [38]. On the other hand, the swelling behavior of natural polysaccharides in the presence of water could result in material disintegration if the swelling overcomes intermolecular forces. Binder characteristics affecting dissolution include solubility, hydrophilic properties, and wettability [38]. Figure 15 shows how disintegration is associated with dissolution. With increasing disintegration, more surface area is exposed to the gastrointestinal fluids.

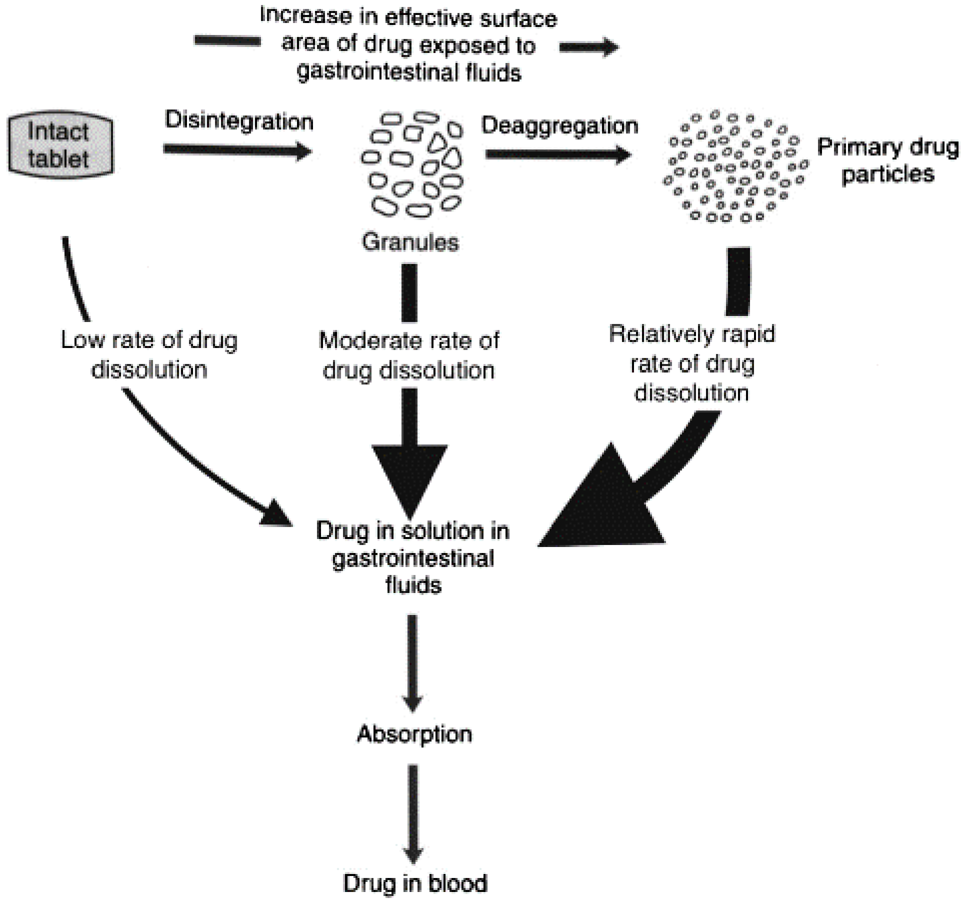

Figure 15: Drug Release process through disintegration and dissolution [6].

2.9 Analysis Methods

2.9.1 X-Ray Diffraction

X-ray diffraction (XRD) is a powerful tool for characterizing inorganic nanoparticles and is non-destructive allowing the sample to be reused for another experiment. XRD is used to perform phase identification, crystallite size, sample purity, morphology studies, and crystal structure analysis, but studies are limited to the crystalline aspect of the material. XRD is also used for phase characterization of materials that have multiple crystal phases known as polymorphs. While other chemical analysis methods evaluate a chemical's empirical formula, they are unable to determine what phase a chemical is in or if it is a mixture of phases. The sample size of XRD samples varies but for x-ray powder diffraction the sample would be in the form of a loose fine powder. The size of the fine powder is important since powder XRD relies on x-ray signals from different orientations of the crystallites. Bragg's Law is used to analyze the sample during XRD analysis as shown in the following equation:

$$n\lambda = 2dsin\theta \qquad \text{Equation (7)}$$

Where θ is the angular position of the x-ray beam, d is the spacing between planes of atoms in the crystalline phase, λ is the wavelength of the x-ray, and n is an integer.

2.7.1i Crystallinity Calculations

Crystallinity calculations from XRD are used to measure the concentration part of the crystal in a sample. Resulting in the ratio between the amorphous and crystalline parts of the sample. The method uses Lorentz polarization factor correction calculation that corrects the intensity from the data shown in the following equation:

$$Post - Corrected\ Data\ Intensity = lo\left(\frac{2}{1+cos^2(2\theta_m)cos^2(2\theta)}\right)$$ Equation (8)

Where lo is the uncorrected data intensity, and θ_m represents the Bragg's angle of the monochromator. After the intensity is corrected the crystallinity is then calculated. The following equation relates the crystalline and amorphous ratio with the crystalline level:

$$\frac{Mcr}{Ma} = \frac{X}{1-X}$$ Equation (9)

Where Mcr is the crystalline part of the sample, Ma is the amorphous part of the sample, and X is the crystalline level in the sample. The next equation relates the ratio between the crystalline and amorphous with the crystalline integral intensity and the intensity of x-ray scattering shown in the following equation:

$$\frac{Mcr}{Ma} = \frac{lcr}{K_X * la}$$ Equation (10)

Where lcr is the integral intensity of the crystalline part, and K_X is the x-ray scattering from the crystalline part. Combining equations 9 and 10 results in the following equation:

$$X = \frac{1}{1+K_X * \frac{la}{icr}}$$ Equation (11)

2.7.1ii Crystallite size & Lattice Strain (Scherrer's Method)

Scherrer's method calculates the sample's crystallite size and lattice strain at specific peak locations. The method uses the following equation shown below:

$$\beta = \frac{K_S * \lambda}{Dhkl * cos\theta} \qquad \text{Equation (12)}$$

Where β is the integral width, K_S is Scherrer's constant (usually 1.05 but is different depending on the crystal), λ is the wavelength of the x-ray, and $Dhkl$ represents the particle size perpendicular to the (hkl) plane.

2.7.1iii Crystallite Size & Lattice Strain (Hall's Method)

Similar to Scherrer's method, Hall's method calculates the crystallite size and lattice strain at a specific peak location. Hall's method uses the following equation listed below:

$$\frac{\beta cos\theta}{\lambda} = \frac{1}{\varepsilon} + 2\eta * \frac{sine\theta}{\lambda} \qquad \text{Equation (13)}$$

Where ε is the average size of crystal particles, and η is the grating distortion. The relationship between the average size of crystal particles and particle size is shown:

$$Dhkl = K\varepsilon \qquad \text{Equation (14)}$$

To use Hall's method, the integrated width curve needs to be calculated using the following equation:

$$b^2 = A(tan\theta)^2 + Btan\theta + C \qquad \text{Equation (15)}$$

Where b is the integral width of the peak, and A, B, and C are coefficients of the approximate formula.

2.9.2 Fourier-Transform Infrared

Fourier-Transform Infrared (FTIR) spectroscopy utilizes infrared radiation (IR) that is found between the frequencies 14300 and 20cm^{-1}, which is also considered electromagnetic radiation. Mid IR range between the frequencies 4000 to 400 cm^{-1} is considered the most practical for organic chemistry. FTIR operates by applying IR to a sample and measuring the amount absorbed by the molecular vibrations within the sample. The vibration of a molecule depends on the chemical bond between other atoms and the mass of the atom. Due to this, FTIR is ideal for identifying functional groups in molecules and handles a variety of sample types including gas, liquid, powder, and nanomaterials. The use of FTIR requires simple sample preparation with little to no solvent use depending on the application [39] [40] [41].

When a molecule absorbs infrared radiation, there is a transition in vibrational energy states. Therefore, the vibration of a molecule will determine the infrared radiation that will be absorbed. When the energy is absorbed by the vibrations, there will also be a change in the rotational energy states. This will result in the IR absorption band given by the FTIR. The energy vibration levels are described by the following equation:

$$E_{vib} = \left(n_v + \frac{1}{2}\right) hv \qquad \text{Equation (16)}$$

Where E_{vib} is the energy of the vibration levels of the molecule, n is the vibrational quantum number, h is Planck’s constant, and v is the vibration frequency. The FTIR’s infrared spectra are represented by absorbance and transmittance as shown in the following equation:

$$A_b = \log\left(\frac{1}{T}\right) = -logT = -\log\left(\frac{I}{I_o}\right) \qquad \text{Equation (17)}$$

Where A_b is the absorbance, T is the transmittance, I is the power transmitted by a sample, and I_o is the radiant power incident on the sample.

2.9.3 Differential Scanning Calorimetry

Differential Scanning Calorimetry (DSC) is a popular tool for thermal analysis and has been used in the pharmaceutical industry to study excipients and Deoxyribonucleic acid (DNA) drugs. DSC can analyze a sample's thermodynamic property, the energetics of phase transitions, temperature dependence characteristics [42], exothermic/endothermic effects, phase transition enthalpies, and measure specific heat capacity [43]. DSC works by measuring the heat flow in and out of a sample while heating, cooling, or holding a constant temperature isothermally. The furnace of a DSC has two locations where a crucible is placed on top of a glass ceramic material called the interface. One crucible is for the sample, while the other is for reference. The furnace also contains an inlet for purge gas, while the heater is located below the furnace shown in Figure 16. The furnace itself is made of pure silver [43].

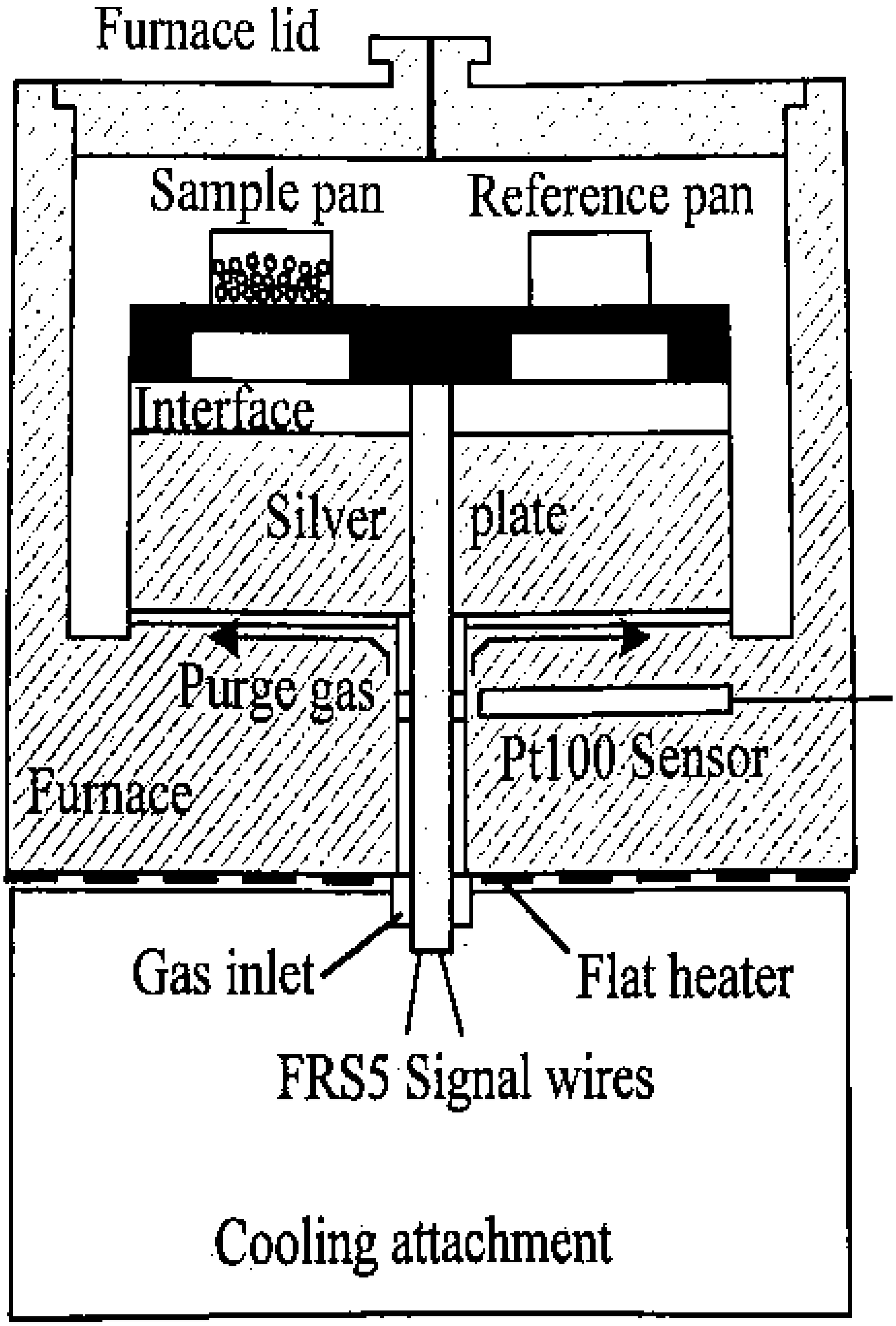

Figure 16: DSC Furnace Overview [43]

Heat flow to the sample flows radially through a disk located below the crucible where two temperature sensors are found. The temperature sensor below the sample crucible is named Ts, while the sensor below the reference crucible is named Tr. The sensor located on the outside of the crucible is called Td. A fourth temperature sensor Tc is in the silver plate below the crucible as shown in Figure 17 and is responsible for recording the furnace temperature [43].

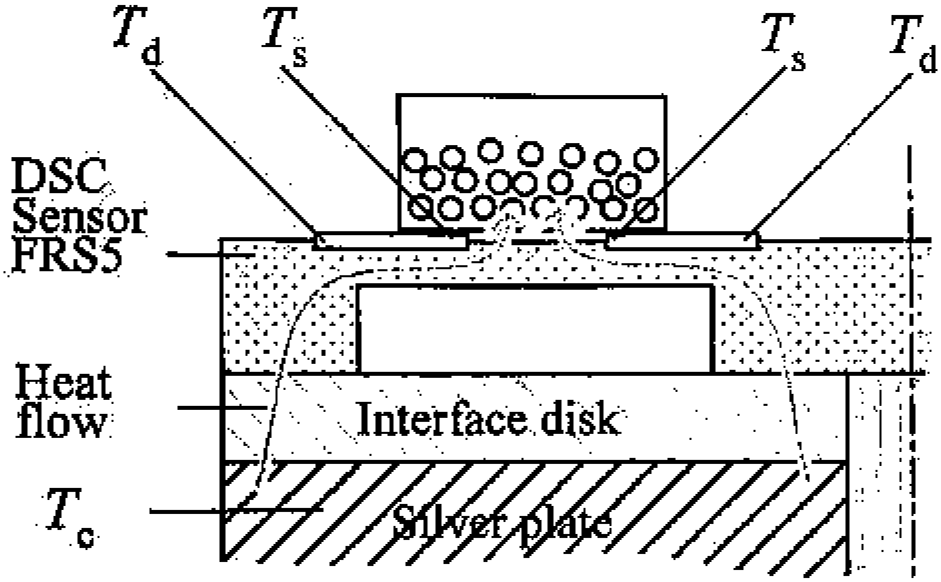

Figure 17: DSC Furnace Temperature Sensors on Sample side of Plate [43]

The following equation represents the heat flow on the left side with the sample crucible:

$$\varphi_l = \frac{T_s - T_c}{R_{th}} \qquad \text{(Equation 18)}$$

Where, φ_l is the heat flow on the left side and R_{th} is the thermal resistance of the sensor plate. The following equation is for the right side with the reference crucible:

$$\varphi_r = \frac{T_r - T_c}{R_{th}} \qquad \text{(Equation 19)}$$

Where, φ_r is the heat flow on the right side of the plate. Subtracting equation 19 from 20 would give us the DSC heat flow signal as shown:

$$\varphi = \varphi_l - \varphi_r = \frac{T_S - T_C}{R_{th}} - \frac{T_r - T_C}{R_{th}} = \frac{T_S - T_r}{R_{th}} \qquad \text{(Equation 20)}$$

Where φ is the heat flow signal given by the DSC.

3. MATERIALS AND METHODS

3.1 Materials

The granule matrix was formulated using the API 4-acetaminophenol, 98% (Acros Organics), also known as APAP. The tablet matrix consisted of APAP and one of the following excipients: d-sorbitol (Fisher Bioreagents), guar gum powder (Aqua Solutions), commercial allulose, commercial xanthan gum, polyethylene glycol 8000 (Fisher Bioreagents), and pectin (Acros Organics). Three-dimensional (3D) molds for forming the tablets were produced using MakerBot Repicator+ and Flashforge Guider II 3D printers. PLA and ABS filaments of varying colors were used.

3.2 Solution Creation: Full Synthetic and Sweeteners

The liquid solution used for wet granulation was made using a known amount of one excipient and deionized water. Fully synthetic and sugar solutions were made using saturation percentages to determine the amount of excipient used in the solution. For example, a solution containing d-sorbitol (DS) at 25% of the maximum saturation will be named DS25; for 50% saturation the solution will be named DS50; and so on. This method is used with excipients that are soluble in deionized water including the synthetic and sugar excipients used in experiments. When creating the solution, a known mass of a single excipient is added to a flask before adding a known amount of deionized water. A stir bar was used to agitate the solution until the excipient fully dissolved. It should be noted that while experiments were done in saturation, the tablets will be referenced in weight percentage for easier comparison. Table A.1 shows the weight percentage equivalent to the tablet saturation.

3.3 Solution Creation: Polysaccharides

Polysaccharides, also known as gums, absorb water when in an aqueous solution rather than dissolving. Therefore, water absorption capacity (WAC) was used rather than max saturation. WAC test used model 642VES Centrifuge (Horizon), Oak Ridge Centrifuge Tube 10ml (Thermo Scientific), Precision Compact Oven (Thermo Scientific), and Touch Mixer Model 231 (Fisher Scientific). An empty 10 mL centrifuge tube was weighed before loading a known mass of excipient into the tube. The weight of the tube with the excipient was recorded before loading about 8 mL of deionized water into the tube. The excipient was completely wet before being loaded into the centrifuge, where the centrifuge was set to run for 1 hour at 3800 rpm. After centrifuging, the supernatant was removed from the tubes and into a compact oven at 50°C for 20 minutes to remove any unabsorbed water. The test tubes were removed from the oven, and the final weight of the tubes are recorded. Equation 3.1.3 was used to calculate the WAC as shown in the equation below:

$$WAC\ \left(\frac{DI\ Water\ (g)}{Gum\ (g)}\right) = \frac{W_{Final} - W_{Tube}}{W_{gum}} \qquad \text{Equation (21)}$$

where “Final” represents the weight of the tube after being placed in the oven, and “Tube” represents the weight of the tube and the gum excipient before centrifuging. Once the WAC of the excipient was known, the WAC would be used in place of the saturation percentage. For example, if guar gum (GG) is at 50% of its WAC in a solution, then the solution would be GG50. To create the solution, a known amount of excipient was added to a known amount of deionized water, and a mixer is used until a uniform hydrocolloid solution is formed.

3.4 Granule Formation

The wet granulation method took place in 3D-printed polymer molds. A mass of 325mg of APAP was placed into each hole, and the mold was tapped onto a surface to remove any voids in the powder. A volume of 500µL excipient solution was added to each of the holes before placing the mold into an oven at 50°C to aid in the drying processes. After drying, the granules were removed from the mold by tapping the mold on a solid surface. The granules were stored in a desiccant cabinet until they are further characterized.

3.5 Image Analysis

Image analysis was accomplished using a Dino-Lite microscope camera for imaging, and Image-Pro Premier software for image processing. Before using the Image-Pro software it needed to be calibrated for accurate measurements. This was accomplished by taking a picture of the ruler using the Dino-Lite microscope at the same position that would be used for image analysis. The image of the ruler was then transferred to the Image-Pro software, where the calibration was made. After calibration, images of the tablets were taken using the microscope, where the image was transferred to the software for analysis. Using the software, the area, aspect ratio, perimeter, roundness, and diameter was analyzed for each tablet.

3.6 Dissolution and UV-Vis

Dissolution testing was accomplished using the Agilent Technologies BIO-DIS Reciprocation Cylinder Apparatus 3 shown on the left in Figure 18. The 7.0 pH phosphate buffer solution served as the solvent and was obtained from Acros Organics.

Figure 18: BIO-DIS Reciprocation Cylinder Apparatus (Left), UV-1280 Multipurpose UV-Visible Spectrophotometer (Right)

The water bath in the dissolution apparatus was used as a heat transfer medium at 37°C. A phosphate buffer volume of 250ml was placed into the outer media tubes of the dissolution apparatus and left to sit in the water bath until the buffer reaches 37°C. A single granule obtained from wet granulation was weighed before being placed into a sample tube. Before placing the granule into the tube, it was analyzed using the Image-Pro Premier software where the area, perimeter, and height were recorded. The mass of the granules was also recorded before disintegration analysis. The apparatus was programmed to dip the sample tube into the outer tube at 10 dips per minute (dpm). Samples from the outer tube were aliquots taken at 5, 10, 15, 30, 45, and 60 minutes with a volume of 5 mL each. Fresh buffer solution of 5ml was added back to the sample tube after each removal. Each tablet was weighed before being placed into the dissolution apparatus.

Spectroscopy (UV-Vis) analysis was conducted using a Shimadzu UV-1280 Multipurpose UV-Visible Spectrophotometer shown on the right in Figure 18. Before sample analysis was analyzed using UV-Vis, a reference curve known as the standard curve, was obtained. The curve allowed the calculation of the concentration of APAP within dissolution samples. The curve was obtained using 5 different samples containing 0.1, 0.2, 0.3, 0.4, and 0.5g of APAP, while each sample had a set amount of phosphate buffer at 250ml. The resulting concentration of each sample was 400, 800, 1200, 1600, and 2000 µg/mL respectively. Each sample was diluted by taking 1 mL of the sample and mixing it with 99ml of deionized water, resulting in a 100mL solution. Dilution was repeated 3 times per sample where the diluted samples were analyzed and averaged in triplicates. The diluted samples were added to the UV-Vis, where the absorbance was recorded at 243nm (peak responsible for APAP) resulting in the curve shown in Figure 19.

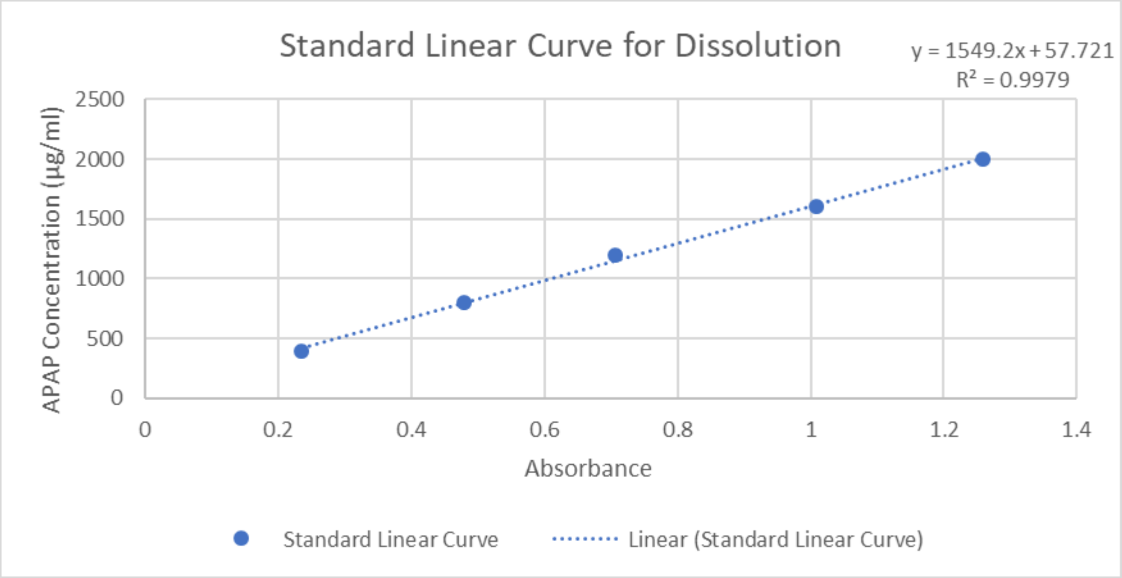

Figure 19: Standard Linear Curve for Dissolution

Applying the raw data to Excel, a calibration curve was established using the trend line feature with over 99% accuracy. The calibration equation allowed the determination of the concentration of APAP for liquid samples from the dissolution experiments.

3.7 Disintegration

Disintegration was accomplished using an Agilent 100 Disintegration Apparatus as shown in Figure 20. Experiments with the disintegration apparatus ran for 5 minutes at 30 dpm. To begin, a 1000mL beaker was filled with 900ml of DI water and inserted into a water bath that was maintained at 37°C. Six tablets were used for each experiment and weighed individually (1 tablet per tube). If some tablets did not disintegrate by the end of the first experiment, the experiment was repeated 2 more times.

Tablets were considered fully disintegrated if the residue of the remaining tablet left on the screen and the surface of the disk was a soft mass that did not have a firm core [44]. Before disintegration, the mass of each tablet was measured and averaged for each set. During the disintegration test, the time was recorded for each of the six tablets and averaged. Criteria for disintegration were met if all six granules disintegrated within 5 minutes for single runs, or if 16 of the 18 granules disintegrated if 3 runs were required.

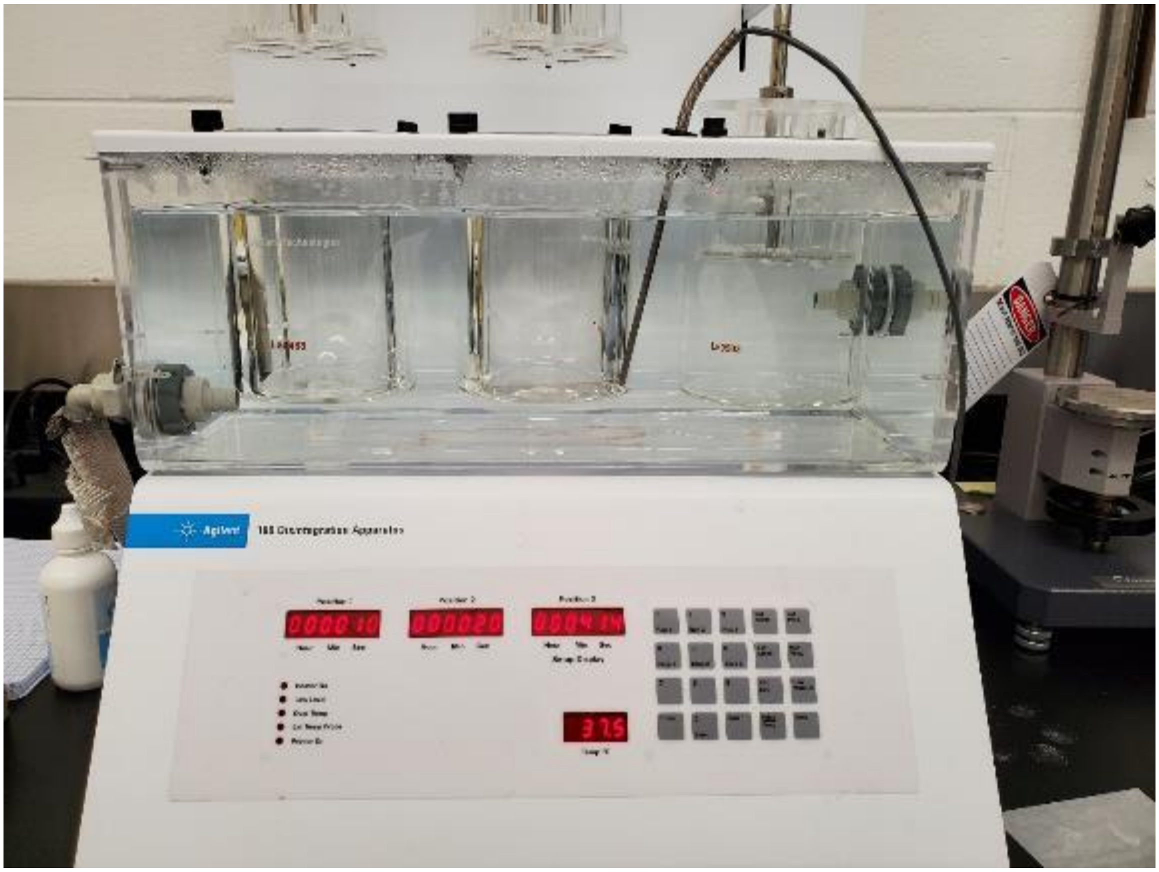

Figure 20: 100 Disintegration Apparatus

3.8 XRD

XRD analysis was accomplished using XRD-7000 X-Ray Diffractometer Maxima (Shimadzu) shown in Figure 21. The XRD was controlled using a computer supported by various applications provided by Shimadzu (Basic Process, Hall’s Method, Crystallinity, Integrated Width Curve). The granules were prepared by grinding for analysis using a mortar and pestle until powder form was achieved. Silica powder (99%) was provided by Shimadzu with the XRD that was used for calibration in Scherrer's and Hall’s methods.

Figure 21: XRD-7000 X-Ray Diffractometer Maxima

The XRD used a copper (Cu) x-ray tube set at a voltage of 40.0 kV and a current of 30.0 mA. The slit used has a divergence and scattering angle of 1.0°, where the receiving slit is 0.30mm. When scanning, the XRD was set to have a theta-2theta drive axis and a scan range of 10° to 80° with a continuous scan speed. The scan speed was set to 2 deg/min for quick analysis, while a slow scan speed of 0.5 deg/min was used for more detailed scans. The sampling pitch was set to 0.0189°, with the preset time set to 4.54 seconds. Sample preparation began by using a motor and pestle to grind the sample to a powdered form (unless the sample is already a fine powder). After grinding, the sample was placed on an aluminum sample plate for the XRD where the sample was flattened using a glass slide. Once the sample was prepared, it was placed into the XRD unit. The measurement conditions are set using the ‘Right Gonio Condition’ window.

After scanning the sample using the ‘Right Gonio Analysis’ application window, the raw data were processed using the ‘Basic Process’ application window, which was required before further processing. The conditions for this processing were as follows:

1) Smoothing is set to manual with smoothing points set to 17.
2) B.G. subtraction is set to manual with sampling points and repeat times set to 19 and 30 respectively.
3) Ka1-a2 separate is set to manual where the Ka1 a2 ratio was set to 50%.
4) System error correction is set to yes.

After processing the data was saved in the same folder. Then, the updated data was available for analysis in different applications.

3.8.1 Crystallinity

The ‘Crystallinity’ application required the usage of the updated data from the previous process to analyze the crystallinity percentage and the crystal/amorphous intensities of the sample. These measurements were made in $kcps * deg$. The K_x parameter condition is set to 1.05 under conditions. After setting the K_x parameter, the crystallinity is measured and recorded.

3.8.2 Integral Width Curve

In the next step, the integral width curve was determined. In this process, a standard sample was analyzed using silica powder. The silica powder analysis occurred using the same method as all XRD samples under analysis. To perform the analysis the angles determined during the basic processing were applied. Next, the silica data was transferred to the integral width curve application window which produced the necessary curve. This information was then utilized in the Hall’s Method window by selecting “integral width curve” from the menu. The sample angle data from the basic process was then set using an error of 0.2 for processing. After the conditions were set, the sample data was dragged and dropped into the application for processing. Next, the application calculated the average crystallite size and lattice strain depending on the points given. This information was recorded in a spreadsheet for each sample.

3.8.3 Crystallite Size and Lattice Strain (Scherrer’s Method)

Scherrer’s method required the use of a standard (Si powder), which was analyzed using the same Basic Processing conditions. in “Basic Process” as the sample. The scan speed was set to 0.50 deg/min once the standard and the sample were processed, and the information was added to the application. Unlike Hall's method, the peaks of the standard and the sample were pre-determined for the conditions. The sample peak to be analyzed was selected based on the resulting scans. The type of experiment must also be set (crystallite size or lattice strain) to process the data.

3.9 FTIR-ATR

From FTIR analysis, an Agilent Technologies Cary 630 FTIR unit with DATR attachment and a ZnSe window was utilized. An image of the instrument is shown in Figure 22. FTIR was used to analyze how the excipient influenced the chemical characteristics of the API's function groups. All samples were ground into a fine powder before analysis.

Figure 22: Cary FTIR with ATR attachment

The following procedure was followed for the FTIR scans:

1) Clean scans before collecting a background scan are set to 4 with a threshold of 0.002, where the background valid time limit is set to 30 minutes.
2) Method type is set to “components”, and the Y-axis units are set to “Absorbance”.
3) The spectral range is set to $4000cm^{-1}$ to $650cm^{-1}$, and background scans and sample scans are set to 140. The resolution is set to $16cm^{-1}$.
4) Apodization is set on HappGenzel, and the sampling subtype is set to “1-Bounce”.
5) Sample data is stored in a folder on the computer desktop.

3.10 DSC

DSC testing was completed using a Mettler Toledo DSC 3 STARe System. The system layout is shown in Figure 23. To begin, samples were placed inside an aluminum 40μL crucible for analysis. The aluminum crucible with lid is weighed before placing a known weight of the sample into the crucible between 3.0 mg and 3.5 mg. A background scan was also conducted using an empty crucible. Both crucibles were placed into the DSC unit. The following procedure was used for the DSC software setup and analysis:

1) Heat flow is set to 10°C/min with a starting temperature of 30°C, and a maximum of 250°C.
2) The DSC is programed to reach maximum temperature and hold for 5 minutes.
3) Temperature is reduced to minimum temperature and held for 5 minutes.
4) Steps 2 and 3 are repeated three times for each sample.
5) Scans were saved to a flash drive for future analysis.

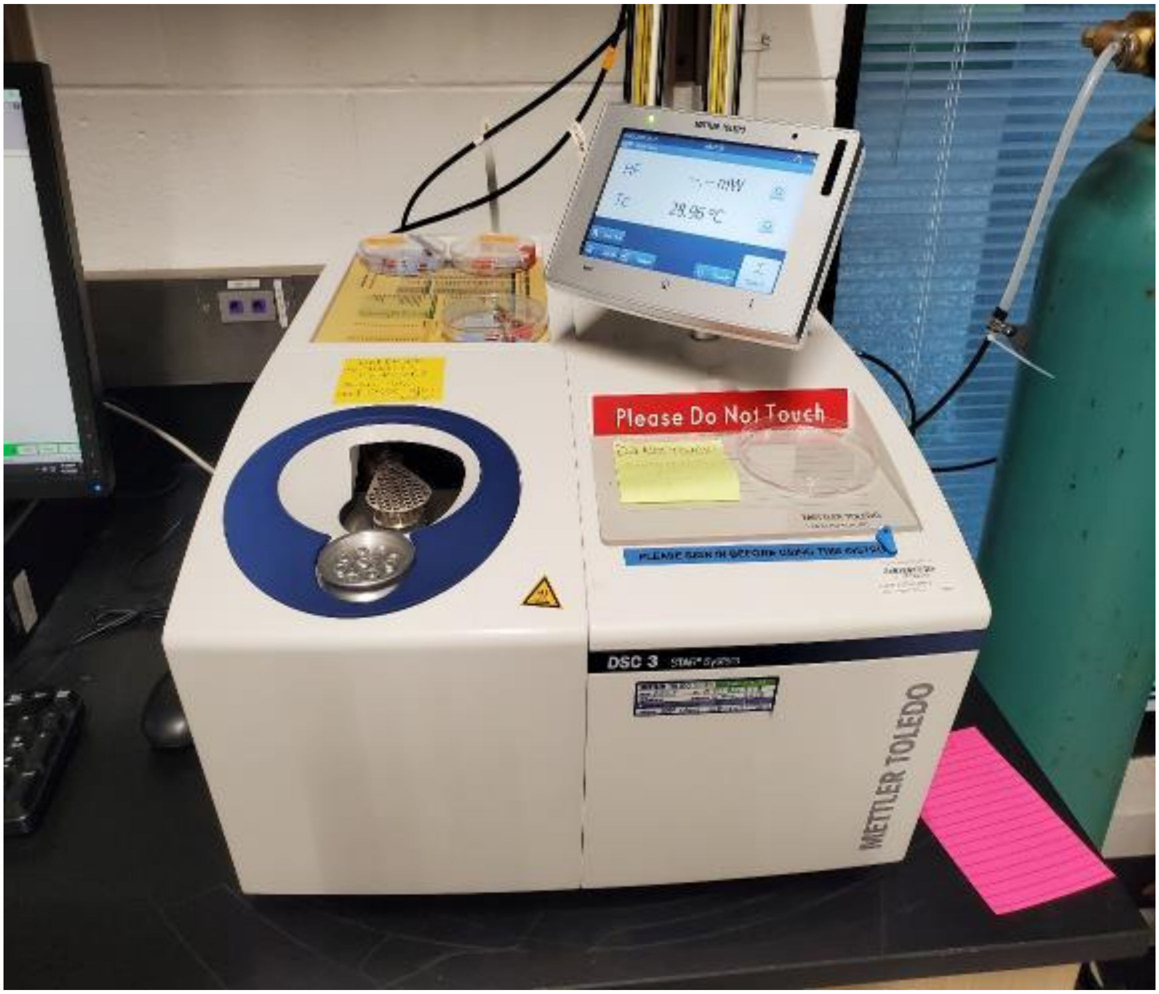

Figure 23: DSC STARe System

4. RESULTS AND DISCUSSIONS

4.1. Task 1: Wet Granulation Method

The wet granulation method used in the research has undergone multiple revisions. The revisions to the method include, where the wet granulation will take place, and how the granules will dry after adding the liquid binder. Wet granulation was originally conducted in Petrie dishes of APAP powder to produce a maximum of 14 granules. This resulted in inefficient use of APAP, where the left-over APAP was designated as waste to limit cross contamination of binder excipients. Granules produced using the trays were ununiformed in size and shape. Therefor the use of 3D molds was implemented to limit the use of APAP and to produce more uniformed granules as shown in Figure 24.

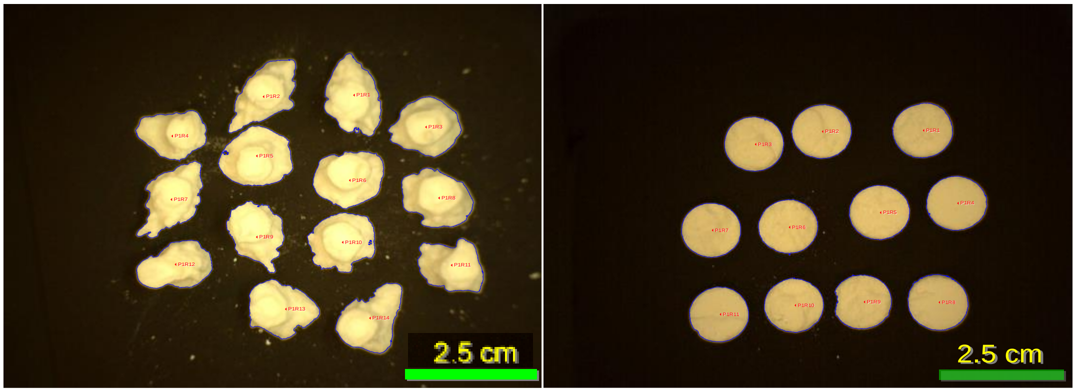

Figure 24: DS 8.67wt% Granules: Petri Dish method (left), 3D Mold Method (Right)

The 3D mold method uses 0.325g of APAP per granule, with a total of 3.9g of APAP being used per 3D mold. Each 3D mold has produced up to 12 granules max shown in Figure 25. The 3D tablet molds used in the lab were designed by Rincon et. al including prototype 6 mentioned in the following literature [45].

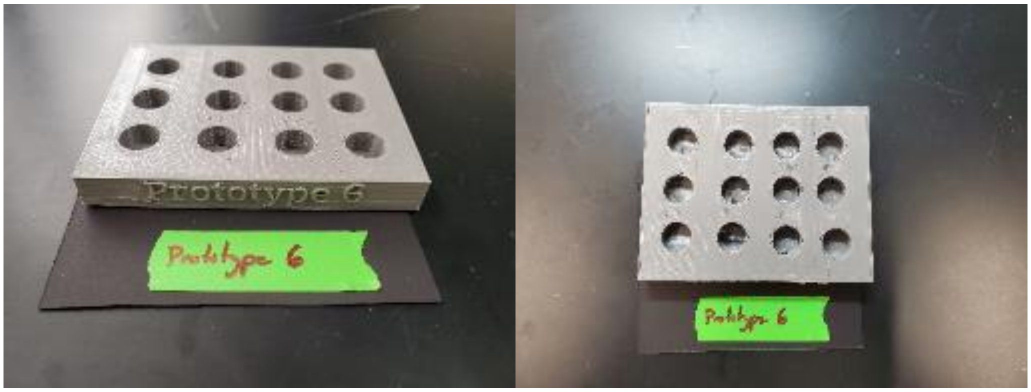

Figure 25: Prototype 6 3D Mold, Angled View (Left), Top View (Right)

The application of the 3D molds significantly improved the wet granulation method by producing granules that were more uniform in shape and size. The use of 3D molds also significantly reduced the amount of APAP waste compared to the use of trays. The granules produced by the 3D molds also appeared to be more tablet-like than the granules formed for the petri dish method. Table 4.1 shown below shows the average dimensions of DS 8.67wt% tables created by both the petri dish and 3D mold methods. Table 2 shows the average size of DS 8.67wt% produced from the tray method and the 3D mold method, while Tables A.2 and A.3 show the averages of the tablets for both methods. A review of Table 2 for DS 8.67wt% tablets proved that roundness and aspect ratio values were closer to 1.0 for the 3D method than the Petri method. The standard deviation was also lower for the 3D method than the Petri method showing that the tablets were more unified. The diameter and the area of the 3D tablets were lower than the tray tablets, signaling that the 3D tablets were more uniform and consistent. Due to the tray tablets not having their diameter measured, the major axis was used in its place, which is the horizontal length of the tablet used in Table 2. Figure 26 shows the compression test between three DS tablet concentrations for 3D and tray methods. The 3D molded tablets were observed to handle significantly higher stress than the tablets produced from the tray method.

Table 2: DS 8.67wt% Tablet Comparison between 3D Mold and Petri Dish Method

Tablet	**Area (mm^2)**	**Diameter (mm)**	**Aspect Ratio**	**Roundness**
DS 8.67wt% 3D	115.2 ± 2.3	12.3 ± 0.3	1.0	1.0
DS 8.67wt% Petri	117.9 ± 10.2	13.9 ± 1.5	1.3	1.3

Different drying methods were also used with the 3D molds to improve the drying times of the granules. Drying method experimentation was necessary due to humid lab conditions and the limited air flow through the molds. While the molds improved the overall shape of the tablets, excipients with high viscosity such as synthetic and sweetener excipients, took much longer to dry. Three drying methods were used including a desiccant cabinet, a convection oven, and a vacuum oven. Vacuum oven drying took place between 25-28 in. Hg, and 60°C, resulting in faster drying times then ambient oven and desiccant drying methods. Unfortunately, the success rate of granules forming was exceptionally low. The granules formed easily shattered while being removed from the mold. In Figure 27, the left image shows the tablet breakage while the right image shows the improved tablet production.

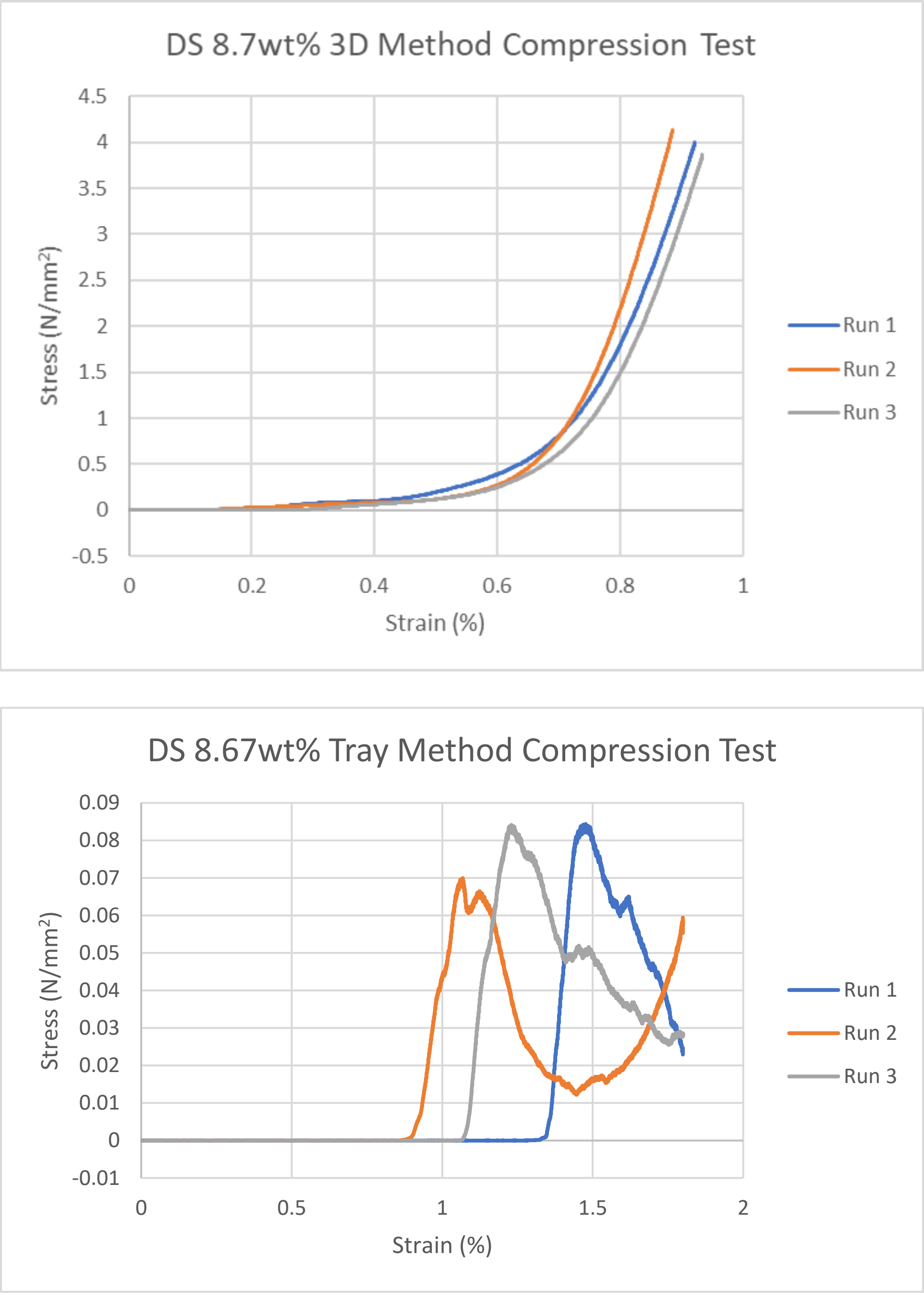

Figure 26: DS Compression Test Comparison Between 3D (Top) and Tray Method (Bottom)

.

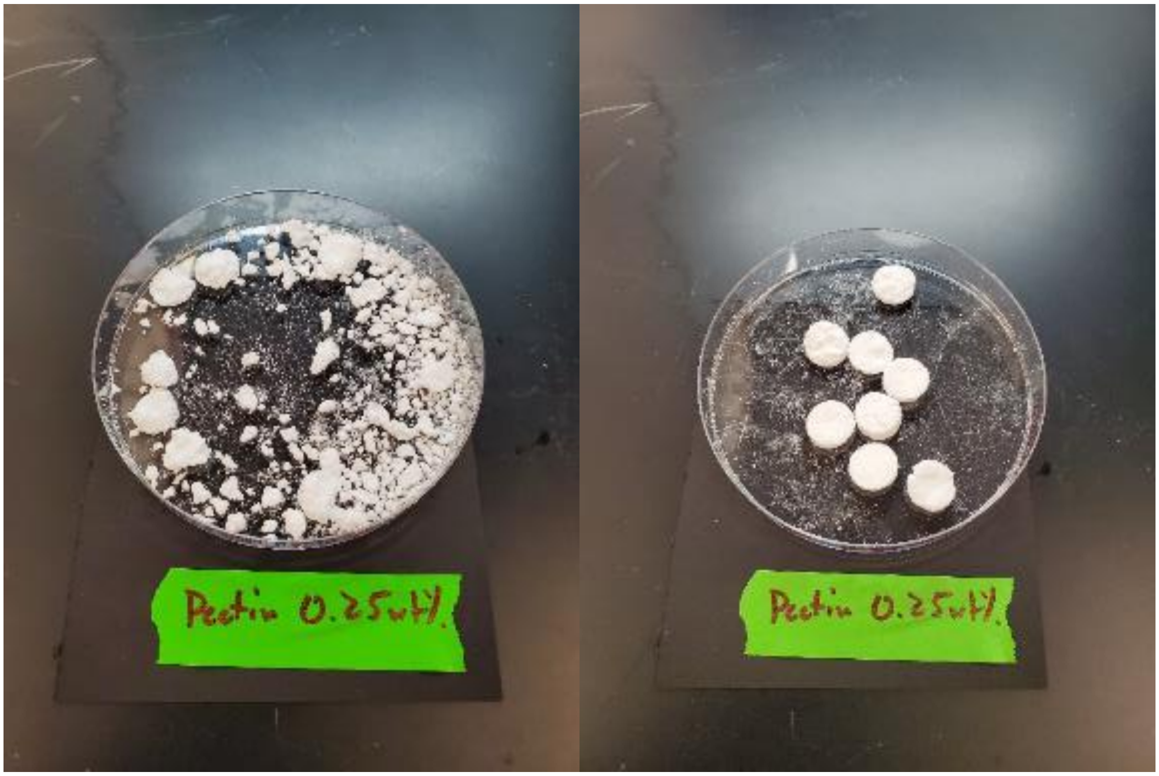

Figure 27: Shattered PC 0.25wt% Granules from Vacuum Oven Method (Left), Uniform Granules from Desiccant Method (Right)

Based on observation, the convection oven and desiccant cabinet method had a higher success rate for wet granulation. Convection oven drying took place between 40-50°C with moderate to high lab humidity (50-85% relative humidity). While the convection oven was more successful than the vacuum oven, there was a chance that granules would burn on the surface producing tablet browning. Granules were also slightly brittle when removed from the mold, resulting in granules breaking upon removal. Both breakage and tablet browning were observed when polysaccharide binders were used. Desiccant drying presented the longest granule drying period with some trials taking an additional 2-3 days. However, the granules were more cohesive, especially with polysaccharide excipients. Observations that part of the tablet stuck to the 3D mold, resulting in a weight reduction when the tablet was removed. This was more prevalent in some granules than others depending on the excipient used and the drying method. Polysaccharide tablets were more likely to stick to the bottom of the 3D mold than sugar and synthetic tablets. With the use of an auto-desiccant cabinet, the severity of the tablet bottom sticking to the 3D mold was reduced. Unfortunately, the 3D mold could not dry tablets that contained a high amount of sugar or synthetic excipients with a high solubility including PEG and DA using a desiccant cabinet. This limited the amount of PEG and DA we could use in the binder solution limiting PEG to 15% and DA to 5% saturation.

4.2 Task 2: Dissolution

Disintegration results, shown in Table 3 show that sugars have almost instant disintegration time followed by synthetic and polysaccharide tablets. DS tablets show rapid disintegration, where the disintegration time shows no correlation with DS concentration. DA tablets also show rapid disintegration where all the tablets disintegrated before 6 seconds. Synthetic PEG tablets had longer disintegration times than sugar tablets, but there was no correlation between disintegration time and PEG concentration. TM tablets showed a correlation between disintegration time and concentration, where TM 0.5wt% had a longer disintegration time than DS and PEG tablets. PC and GG tablets also had longer disintegration times than polysaccharide and synthetic tablets excluding PEG 3wt% which lasted longer than PC 0.5wt%. The first run using XN 0.25wt% had 1 of the 6 granules that did not disintegrate fully by the end of the 5-minute experiment, therefore two more experiments needed to be run. The second and third runs of XN 0.25wt% resulted in two and one granules that did not disintegrate respectively. Therefore 4 of the 18 granules tested did not disintegrate, which did not meet the disintegration criteria.

Table 3: Summary of Disintegration Results

	Sample	Wt. (mg)	Average Disintegration Time (s)	Number of Experiments	Number of Granules Disintegrated
Synthetic	PEG 3wt%	324 ± 4	82.0 ± 73.9	1	6 of 6
	PEG 6wt%	332 ± 8	21.8 ± 31.0	1	6 of 6
	PEG 9wt%	349 ± 4	28.3 ± 7.7	1	6 of 6
Sugars	DS 4.33wt%	323 ± 5	5.8 ± 4.1	1	6 of 6
	DS 8.67wt%	317 ± 13	2 ± 0	1	6 of 6
	DS 13wt%	332 ± 14	8.3 ± 4.7	1	6 of 6
	DA 13.86wt%	327 ± 30	4.7 ± 0.9	1	6 of 6
Polysaccharides	TM 0.10wt%	247 ± 22	45.5 ± 13.1	1	6 of 6
	TM 0.25wt%	259 ± 8	52.5 ± 22.7	1	6 of 6
	TM 0.50wt	266 ± 15	120.8 ± 39.1	1	6 of 6
	PC 0.50wt%	227 ± 16	74.8 ± 20.3	1	6 of 6
	GG 0.36wt%	234 ± 11	106.7 ± 32.9	1	6 of 6
	XN 0.25wt%	279 ± 31	213.2 ± 92.7	3	14 of 18

4.3 Task 3: Dissolution

Dissolution and disintegration of sweeteners within the tablet matrix occurred much faster than polysaccharide tablets, while polysaccharides displayed more controlled dissolution. PEG tablets also had a rapid dissolution for PEG 10 and 15, but PEG 5's dissolution was slower than the higher concentrations. An increased concentration of DS in the tablet matrix reduced the amount of APAP that dissolved into the phosphate buffer solution as shown in Figure 28. Polysaccharide tablets including PC, and XN had slower dissolution than sugar tablets containing DS and DA, while TM and GG tablets had a similar rate to DA shown in Figure 31.

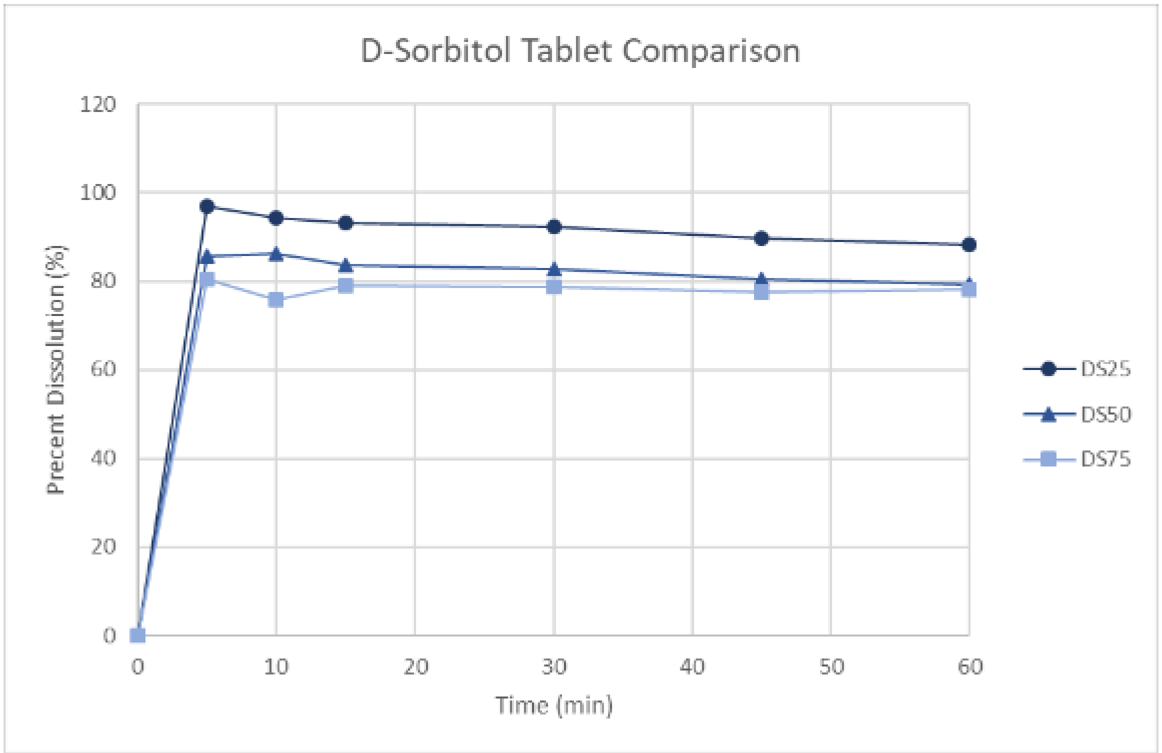

Figure 28: D-Sorbitol Tablet Comparison

Although, dissolution of the DS tablets fully dissolve by 5 minutes regardless of concentration of d-sorbitol. TM tablets had a slower and more controlled dissolution compared to DS and PEG tablets although the TM concentration within the tablet did not correlate with the dissolution characteristics shown in Figure 29.

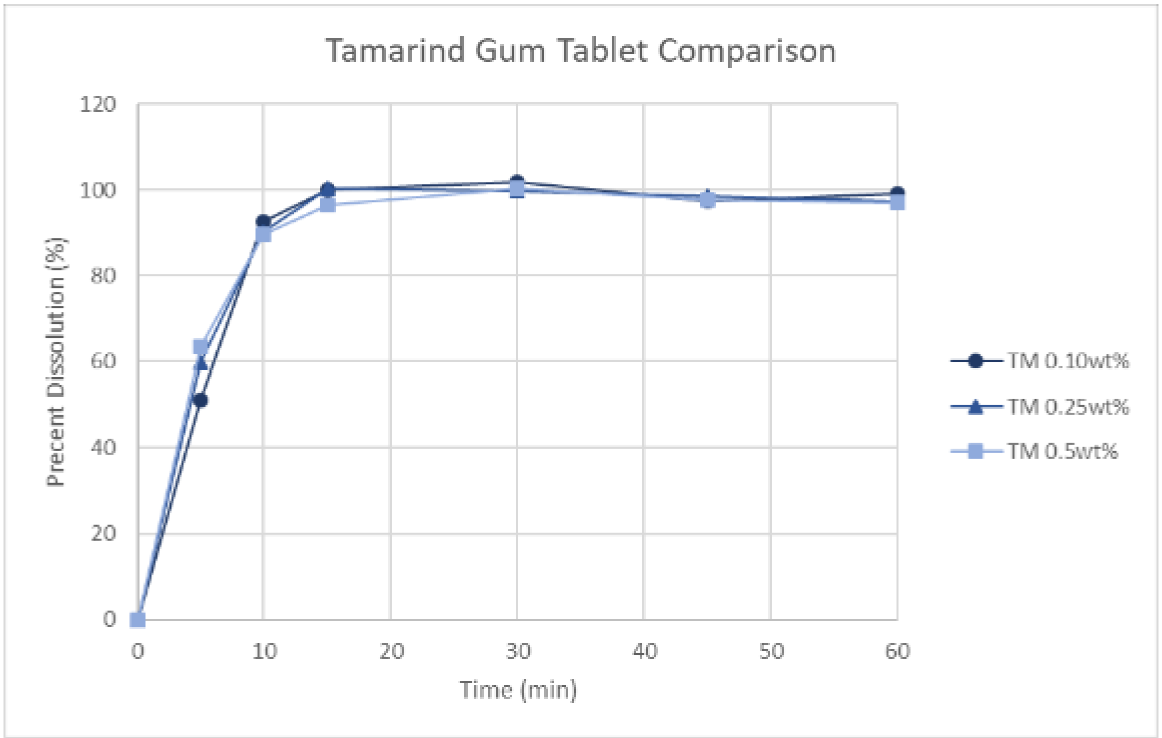

Figure 29: Tamarind Gum Tablet Comparison

PEG 5 maintained a constant rate of dissolution rate for the first 15 minutes before slowing down and reaching its peak at 30 minutes, while PEG 10 and 15 had fast dissolution rates shown in Figure 30. PEG initially showed dissolution comparable to XN0.25wt% for the first 10 minutes, showing a similar characteristic to polysaccharide tablets, but slower than sugar tablets as shown in Figure 31. XN 0.25wt% had the slowest dissolution among all the tablets tested, with DS tablets having the fastest rate of dissolution as shown in Figure 30.

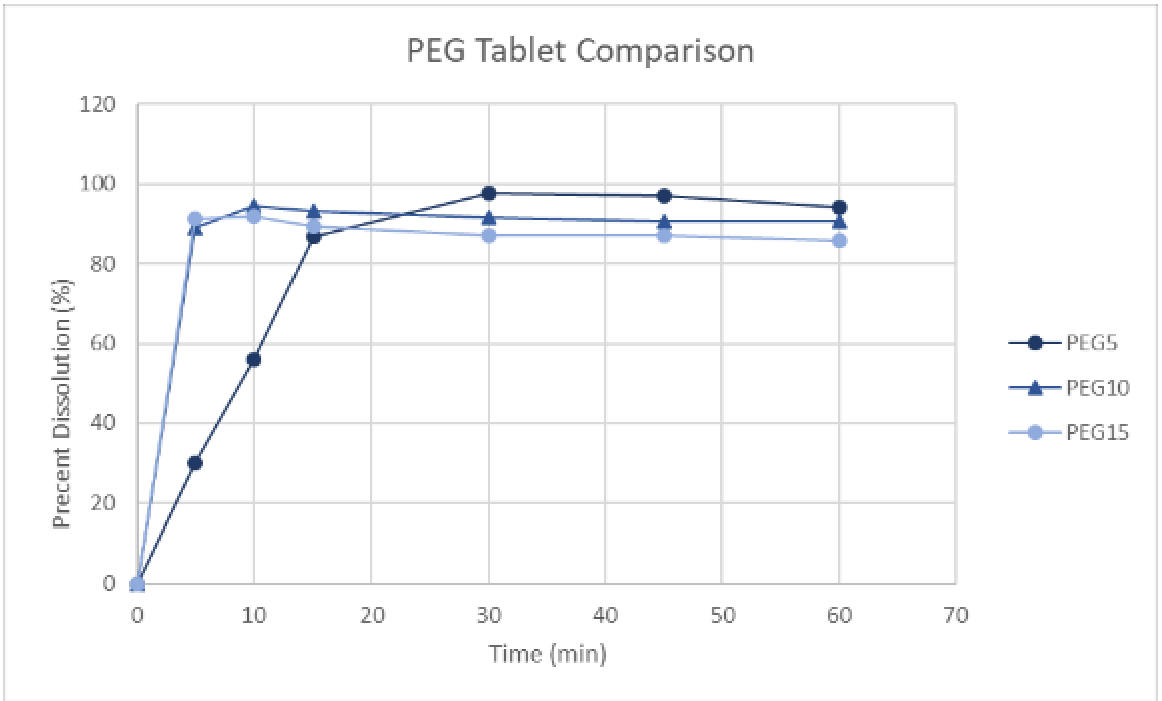

Figure 30: PEG Tablet Dissolution Comparison

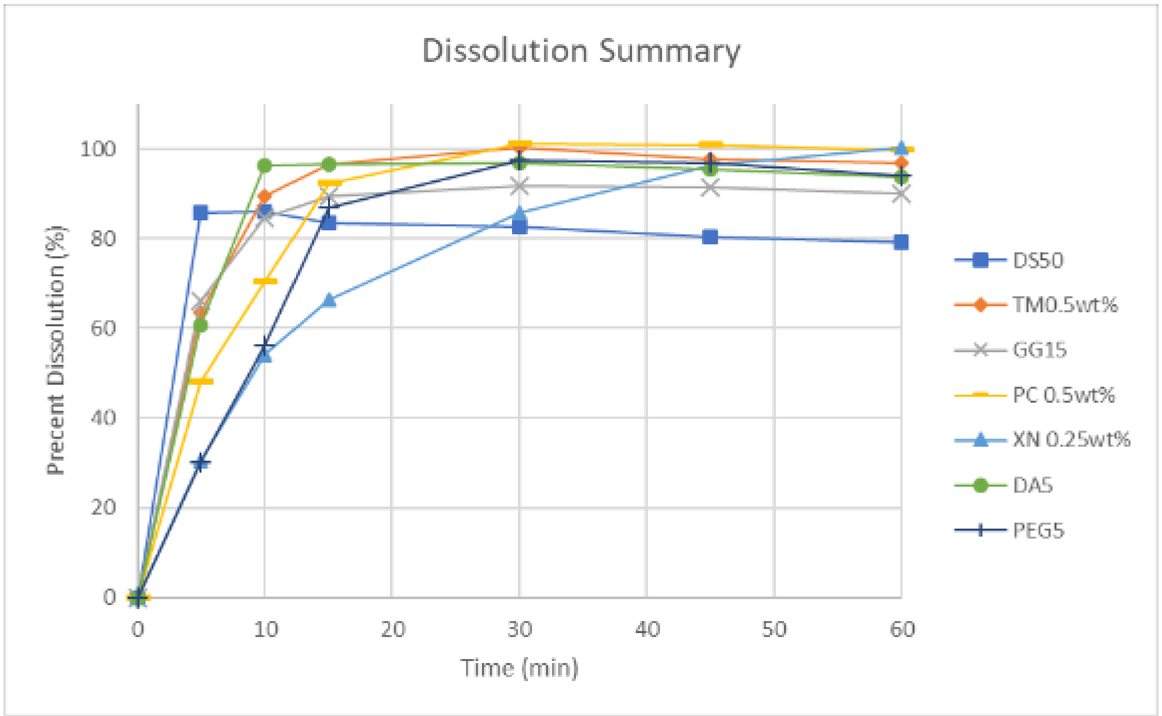

Figure 31: Dissolution Summary

Dissolution kinetic models were also created for one concentration for each excipient. For Zero order kinetics, XN0.25wt% best fits the model with a coefficient of determination (R^2) of 0.798 shown in Figure 32.

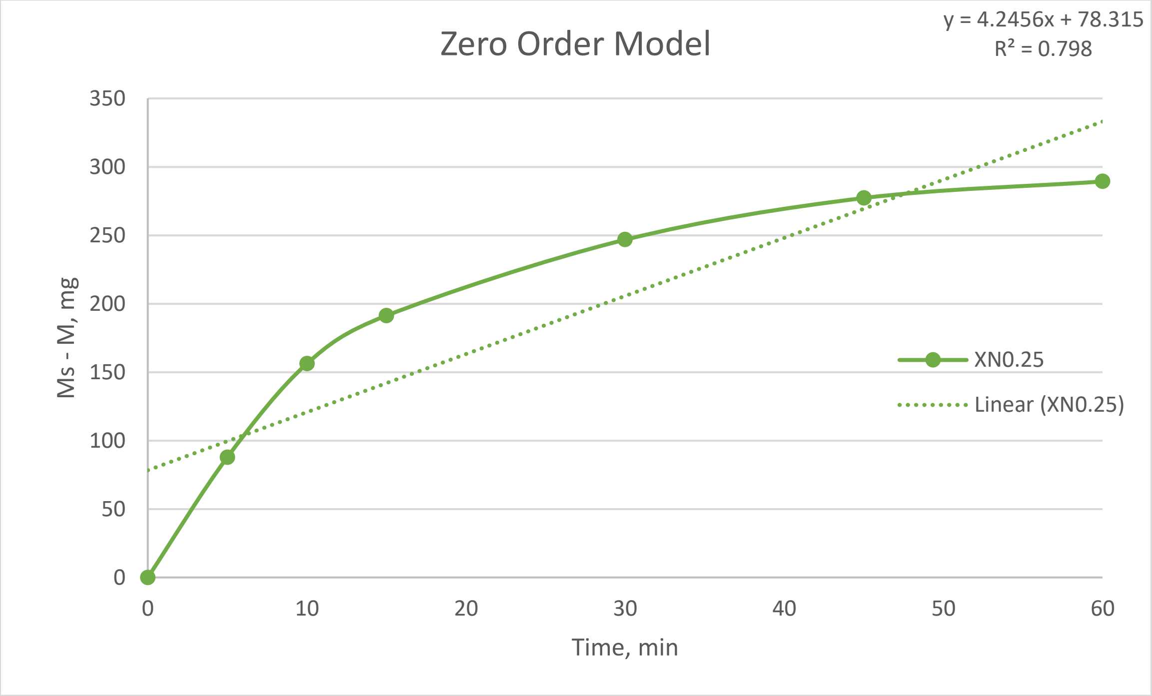

Figure 32: XN 0.25wt% Zero Order Model

For the First Order Model DS8.67wt% (DS50) had the highest R^2 value of 0.946 followed by XN0.25wt% with an R^2 value of 0.727 seen in Figure 33. For the Cubic Root Model XN0.25wt% had the best fit the model with an R^2 value of 0.923 (Figure 35) followed closely by DS8.67wt% (DS50) with an R^2 value of 0.952 (Figure 36). The Korsmeyer-Peppas Model best reflects DS8.67wt% (DS50) with an R^2 value of 0.944 (Figure 38), followed by XN0.25wt% with an R^2 value of 0.762 (Figure 39).

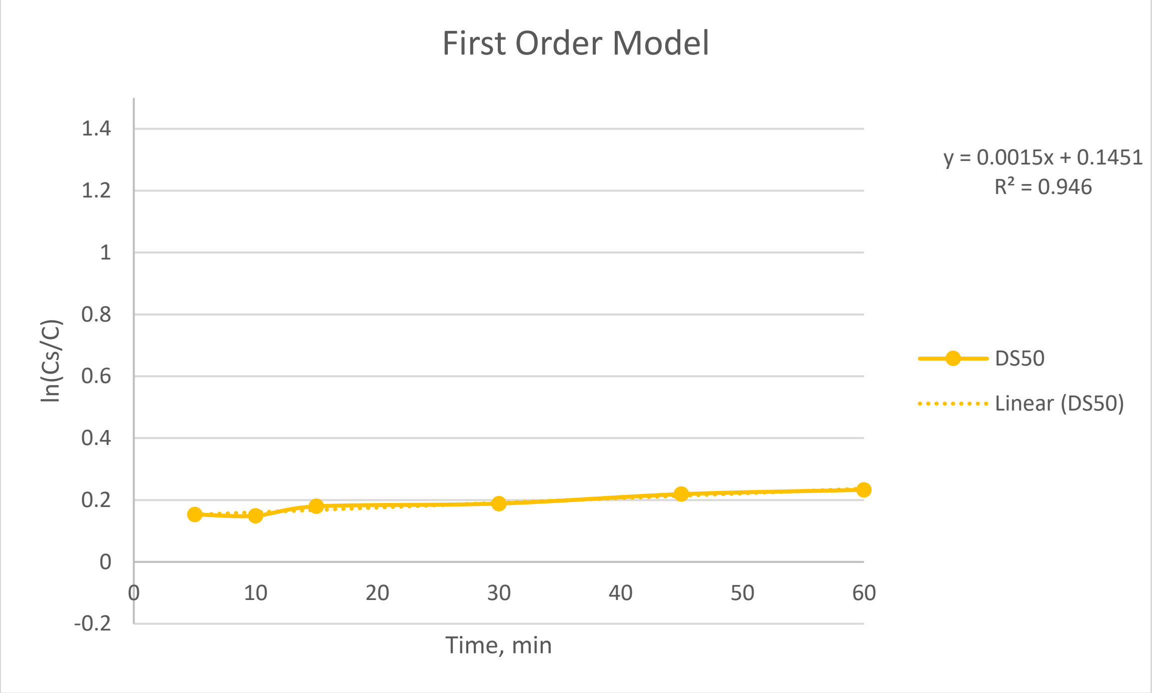

Figure 33: DS50 First Order Model

Figure 34: XN 0.25wt% First Order Model

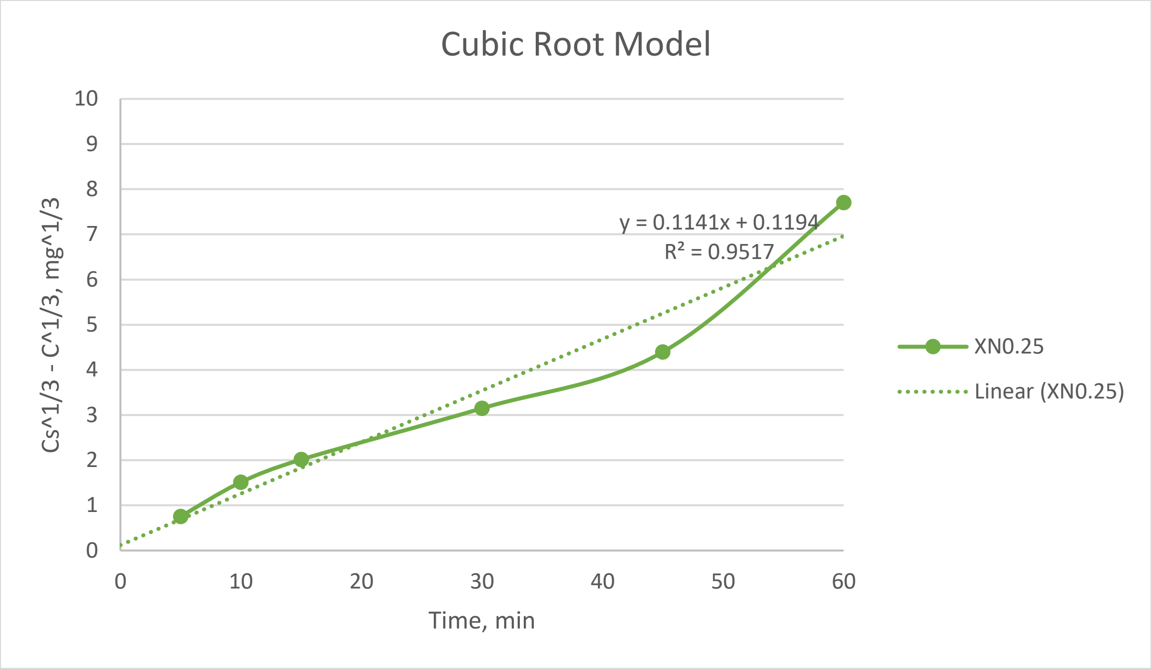

Figure 35: XN 0.25wt% Cubic Root Model

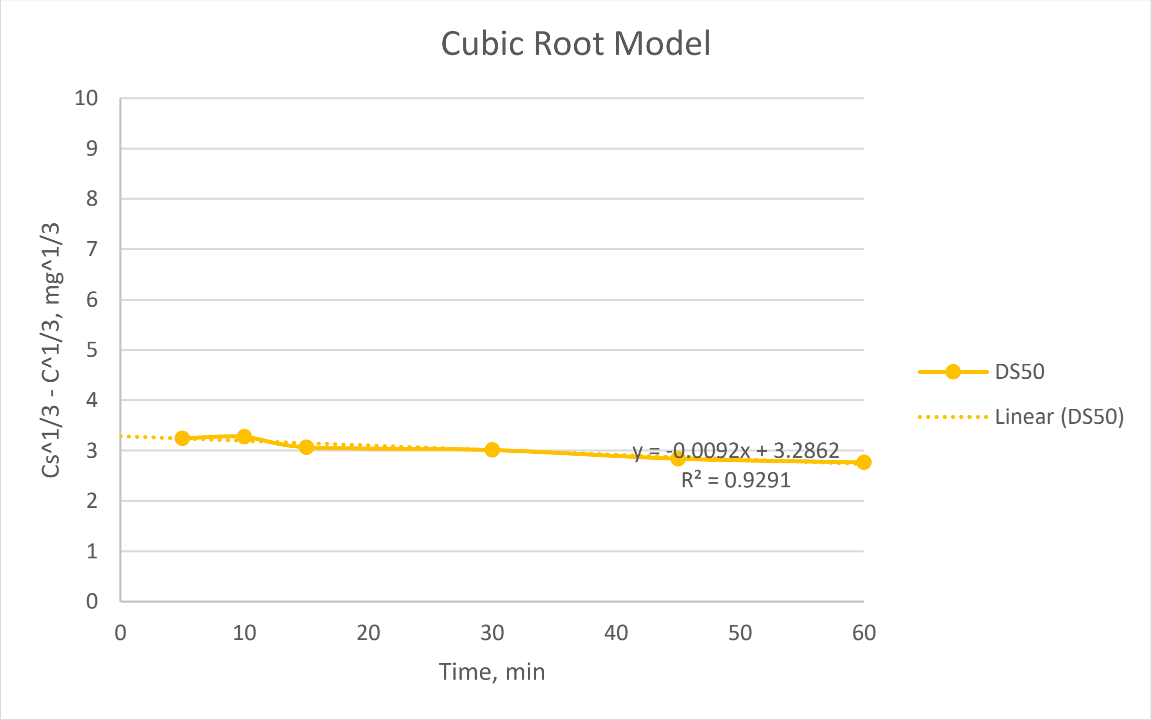

Figure 37: DS50 Cubic Root Model

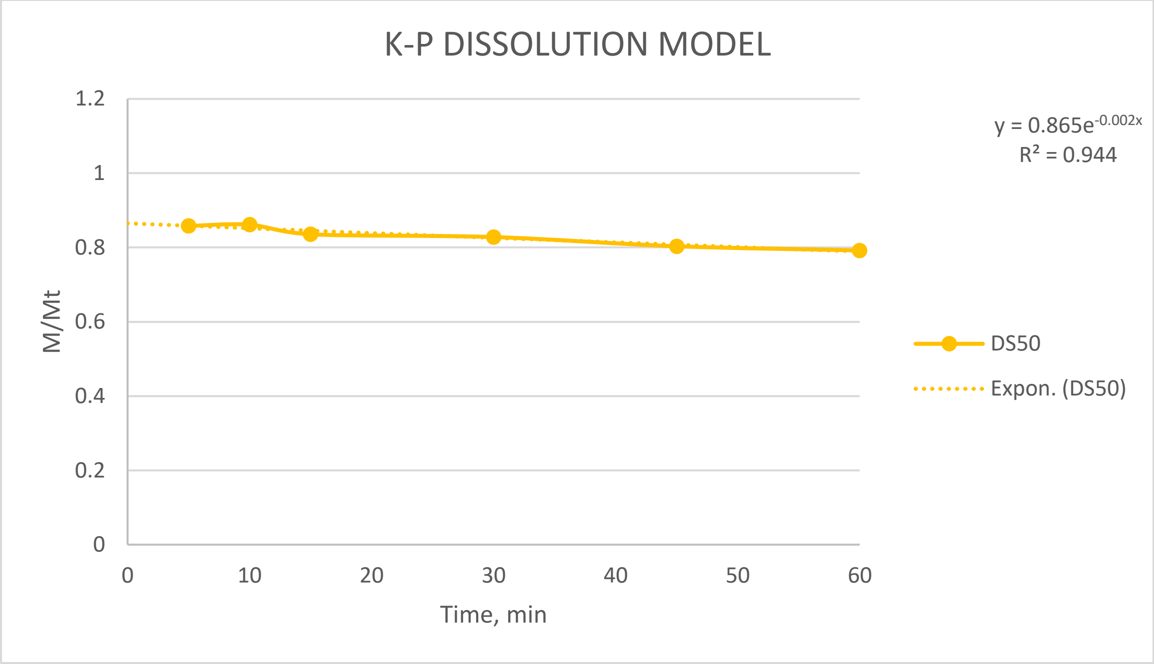

Figure 38: DS50 Korsmeyer-Peppas Model

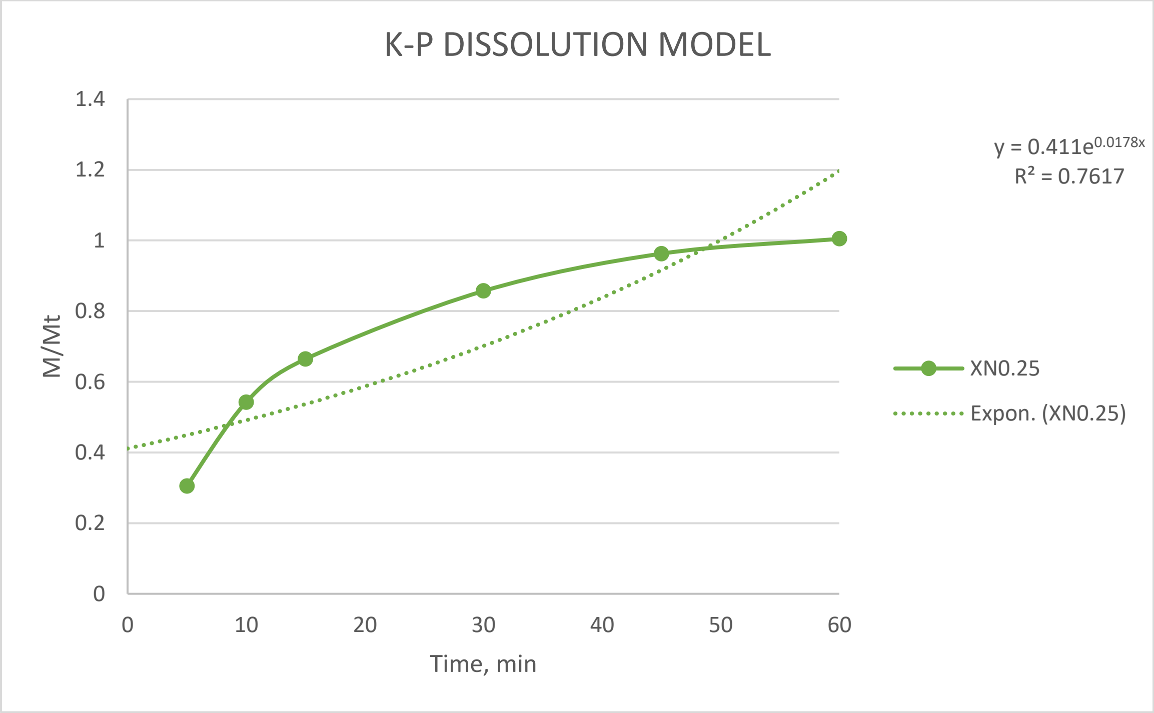

Figure 39: XN 0.25wt% Korsmeyer-Peppas Model

4.3 Task 4: XRD

XRD scans were taken of APAP raw materials and tablets that consisted of one excipient with APAP. Scans show that the excipients do not alter the peak locations of APAP, therefore was no chemical reaction observed between the excipient and APAP. On the other hand, the excipients affect the peak characteristics including peak width and intensity; which is observed using lattice strain, crystal size, and crystallization of APAP. The XRD scans shown in this chapter will be between 10° and 30° to improve the viewability of the data, but the full scans between 10° and 80° are found in the appendix. The raw scan of APAP is shown in Figure 40.

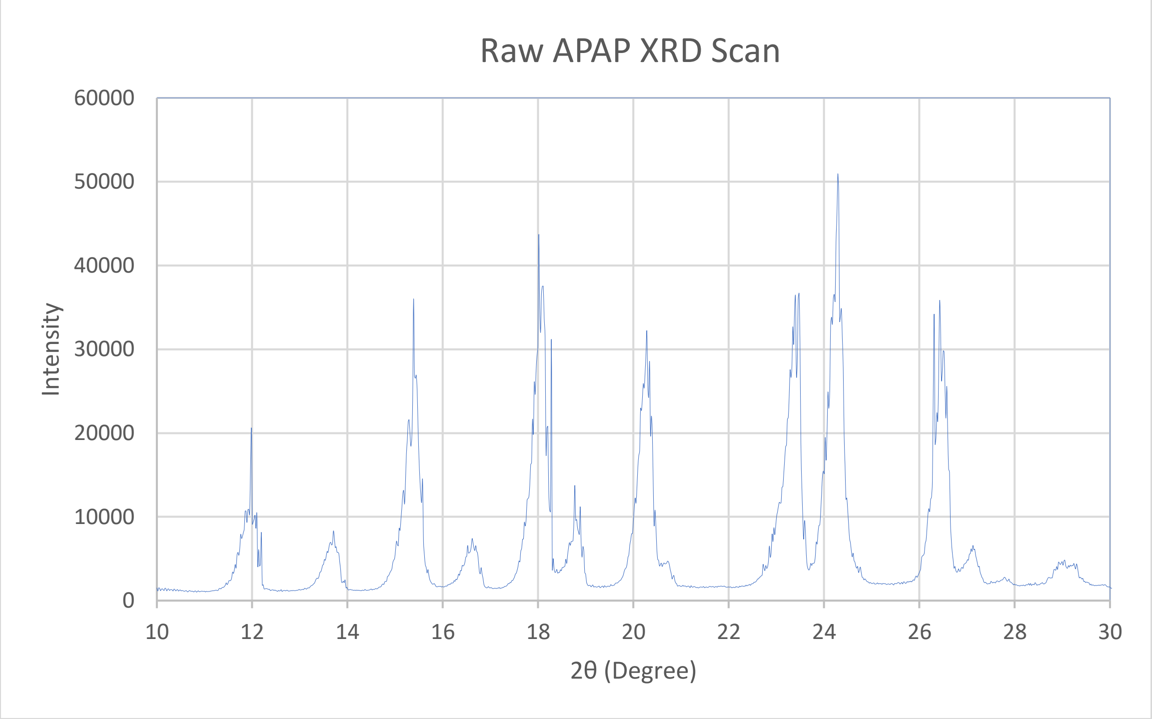

Figure 40: Raw APAP XRD Scan 10° ≤ 2θ ≤ 30°

Table 4: APAP Peak Information

Peak	Relative Intensity	(hkl)
12.09	23	(0,1,1)
13.81	9	(-1,0,1)
15.52	52	(1,0,1)
16.74	9	(-1,1,1)
18.18	72	(1,1,1)
18.91	31	(0,2,0)
20.37	59	(0,2,1)
20.81	5	(-1,1,2)
23.08	9	(1,1,2)
23.48	59	(-1,2,1)
24.36	100	(0,2,2)
26.56	47	(-1,2,2)
27.20	6	(-2,1,1)
29.07	5	(2,1,1)
29.31	4	(1,1,3)

After analyzing APAP using the Basic Data Process application, the strongest 3 peaks are located at 18.104°, 23.402°, and 24.276° with the highest relative intensity. Due to the peak intensity, they were used for Scherrer's method calculations and were also comparable to the literature [46]. The APAP data were also processed using the Crystallinity application giving a crystallinity of 69.513%, crystal intensity of 44.645, and amorphous intensity of 19.581. The hkl values were matched and obtained from the XRD database [46].

PEG tablets (Figure 41) show no new peaks compared to pure APAP, but a change in relative peak intensity. Peaks located at 15.5, 23.4, and 26.5° show a higher intensity than pure APAP, while peaks located at 18.9 and 20.3° intensities decreased. Crystallinity calculations do not show a significant difference for PEG 6wt% and PEG9wt%, but PEG 3wt% shows an increase in crystallinity in Table 4. Scherrer's method in Table 5 shows that the lattice strain of peaks 18.1° show decreased strain while 23.4° show an increase in lattice strain. Peak located at 24.3° show an increase in lattice strain for PEG 9wt%, but a lower strain for PEG 3wt% and 6wt%. The inverse is true for crystallite size. Hall's method shows that PEG 3wt% has a higher average crystallite size and lattice strain between 10 and 30°, while PEG 6wt% and 9wt% show a lower average crystallite size and lower lattice strain than pure APAP. Overall there is no significant change that would interpret a chemical reaction, or that a new compound was formed.

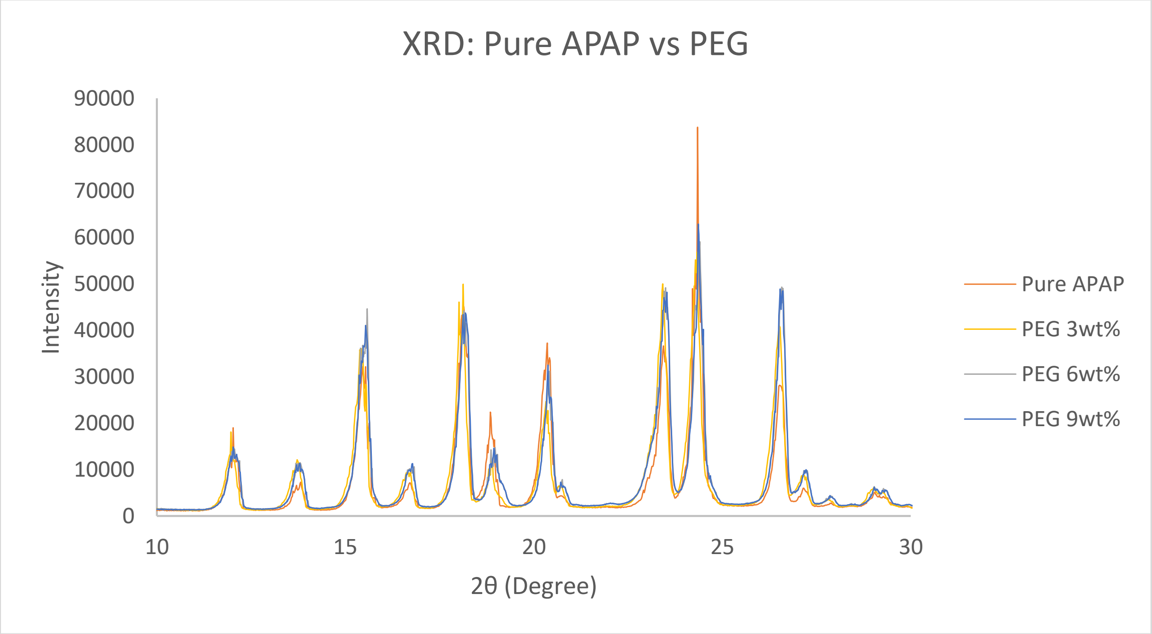

Figure 41: XRD Comparison of Pure APAP vs PEG Tablets at 10° ≤ 2θ ≤ 30°

D-sorbitol (Figure 42) resulted in peak broadening and a reduction in crystallinity from pure APAP, and an increase in crystal and amorphous intensities shown in Table 4. Small changes in peak intensity were also observed, with a significant increase of 26.5 13.8, and 15.5° relative peak intensity. Percent crystallinity decreased significantly to 67.44%, 62.40%, and 60.61% for DS 4.33wt%, 8.67wt%, and 13wt% respectively. Crystal intensity was similar between DS 4.33wt% and DS 8.67wt% but decreased in DS13wt%, while amorphous intensity was lowest for DS 4.33wt% but higher in both DS 8.67wt% and DS 13wt%. The XRD results of DS 4.33, 8.67, and 13wt% show similar peak broadening and peak intensities, but the baseline rises with increasing concentration of d-sorbitol shown in Figure 42. Scherrer's calculation also shows that d-sorbitol affects the lattice strain and crystallite size of APAP in Table 5. PEG 4.33 and 8.67wt% have a higher lattice strain at 18.1° while PEG 13wt% has a lower strain than pure APAP. All three DS tablets have a lower lattice strain at 23.4°, while at 24.3° DS 4.33 is the only tablet with a higher strain. Hall's Method shows that all three concentrations of DS have a lower crystallite size and higher lattice strain average between 10 to 30° compared to APAP.

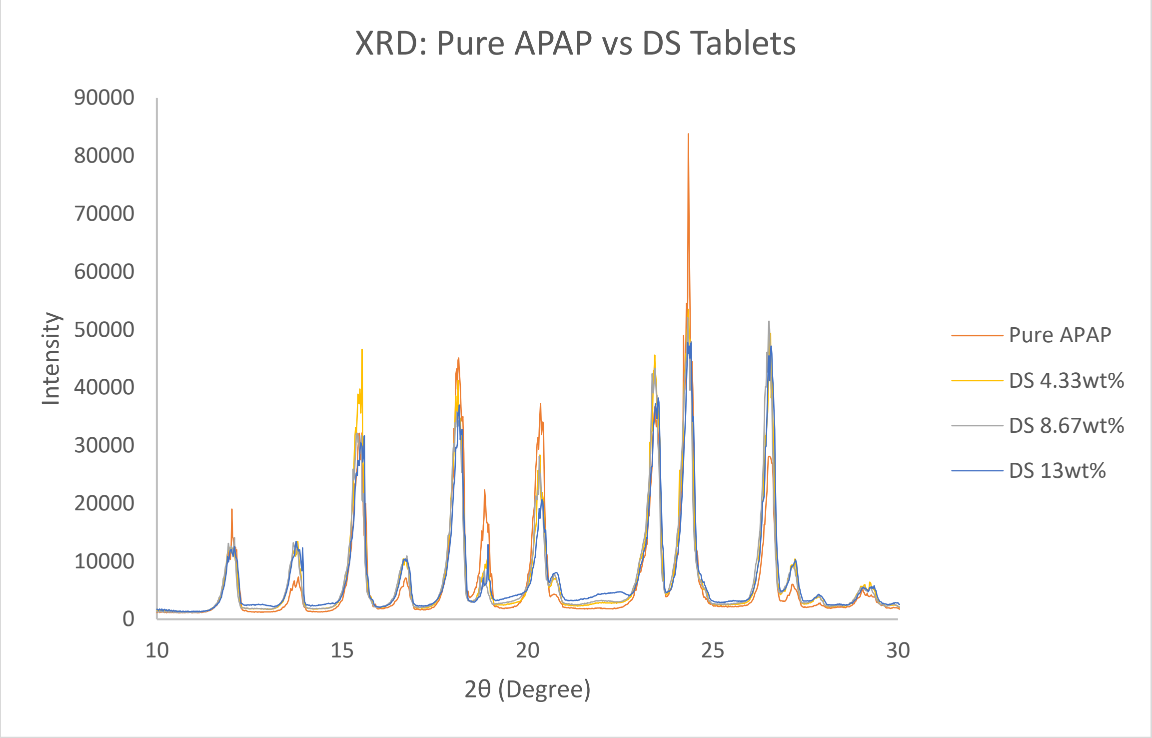

Figure 42: XRD Comparison of Pure APAP and DS Tablets at 10° ≤ 2θ ≤ 30°

TM tablets (Figure 43) show an increase in relative peak intensity at 15.4 and 26.5°, while a decrease in relative peak intensity decreases at 18.8° compared to APAP. All concentrations of TM tablets are higher than pure APAP at 67.44%, 62.40%, and 60.61% for TM 0.1wt%, 0.25wt%, 0.5wt% respectively, although there is no correlation between crystallinity percentage and TM concentration. Scherrer's Method from Table 5 shows that TM 0.1 and 0.5wt% tablets have a lower lattice strain at 18.1°, while TM 0.25wt% lattice strain is higher. At 23.4°, TM 0.25wt% has a lower lattice strain, whereas TM 0.5wt% is higher. Peak 24.3° shows that all TM concentrations have a lower lattice strain than APAP. Hall's method shows that TM 0.1 and 0.5wt% have a lower crystallite size than pure APAP, and TM 0.25wt% is higher. While TM 0.1wt% has a lower lattice strain, and TM0.25 and 0.5wt% lattice strain is higher.

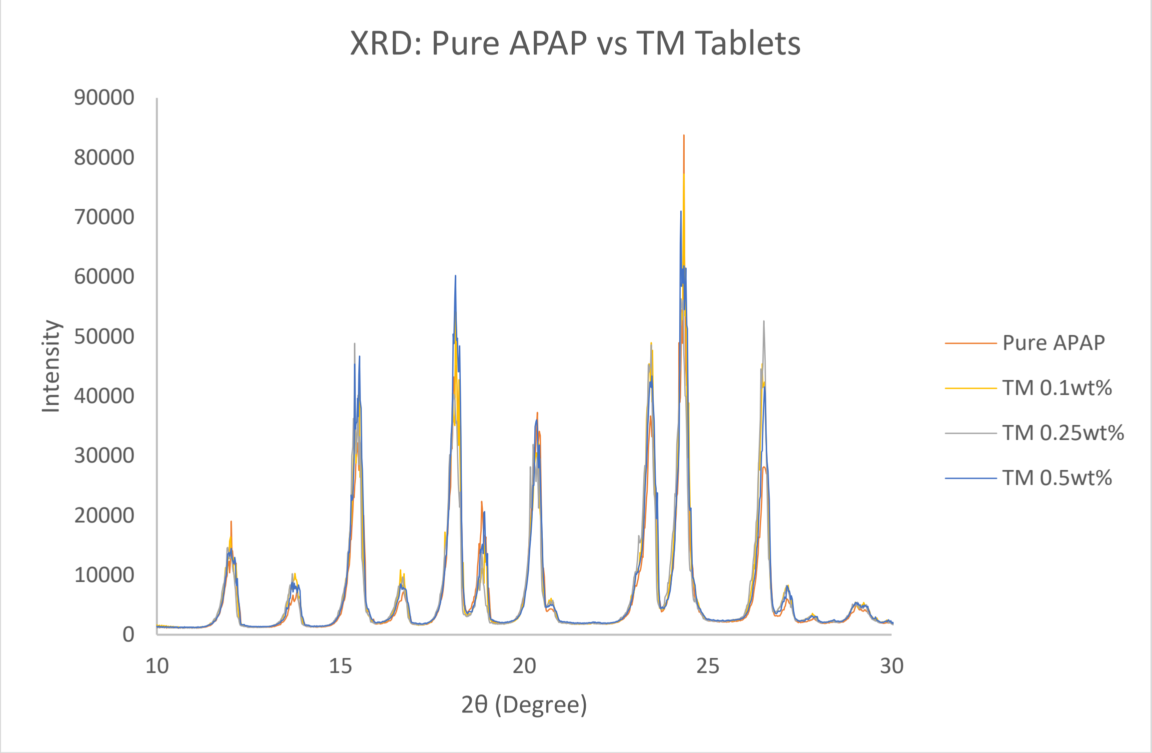

Figure 43: XRD Comparison of Pure APAP vs TM Tablets between 10°≤ 2θ ≤ 30°

Peak broadening is observed in xanthan gum tablet XN0.25wt% as shown in Figure 44. Crystallinity calculations have shown that xanthan gum increased the crystallinity of APAP to 71.067%. Crystal and amorphous intensities also increased to 53.707 and 21.789 respectively. Scherrer's method also shows that xanthan gum decreases lattice strain and increases crystallite size in APAP's 3 largest peaks. Hall's method shows that XN 0.25wt% has a lower crystallite size and lattice strain average compared to APAP between 10 to 30°.

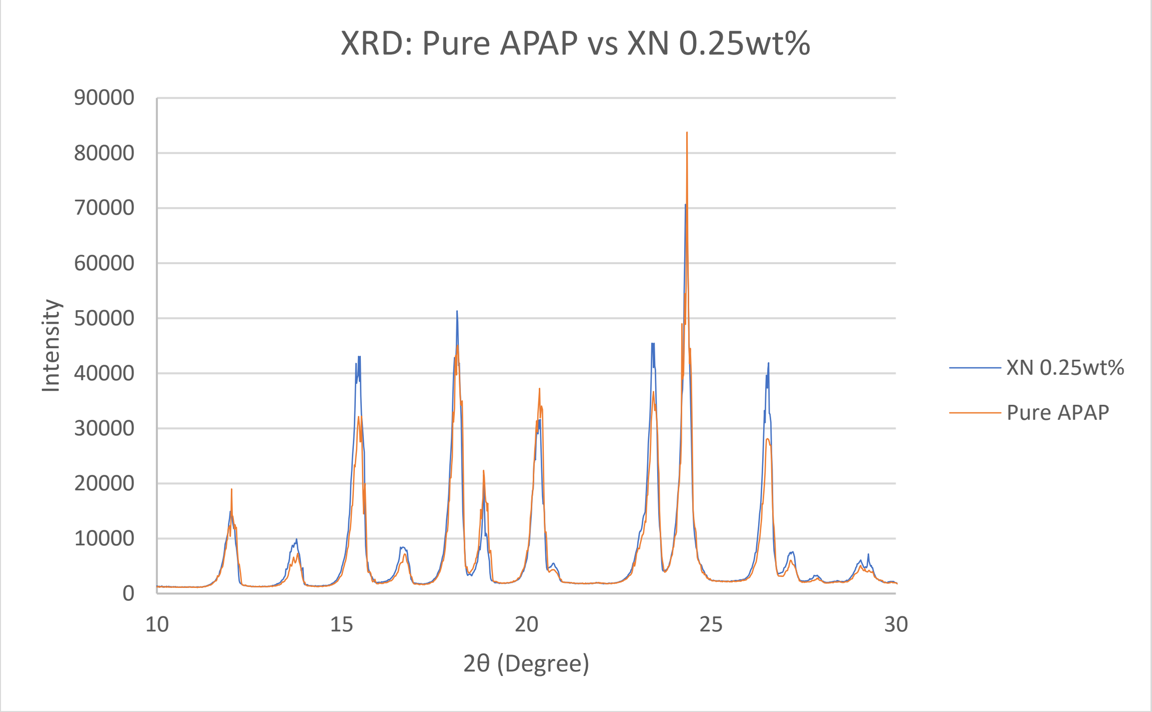

Figure 44: XRD Comparison of Pure APAP and XN 0.25wt% between 10° ≤ 2θ ≤ 30°

Pectin (Figure 45) also shows peak broadening and higher relative intensities at 15.5°, 23.5°, and 26.5°. Crystallinity calculations show that pectin does not have much effect on APAP's percent crystallinity, only increasing it to 69.604% although, pectin increases the crystal and amorphous intensity to 51.479 and 22.481 respectively. Scherrer's method shows that pectin decreases the lattice strain, and increases the crystal size of APAP peaks located at 18.104° and 24.276°. For the peak located at 23.402°, the lattice strain slightly increases, and crystallite size decreases.

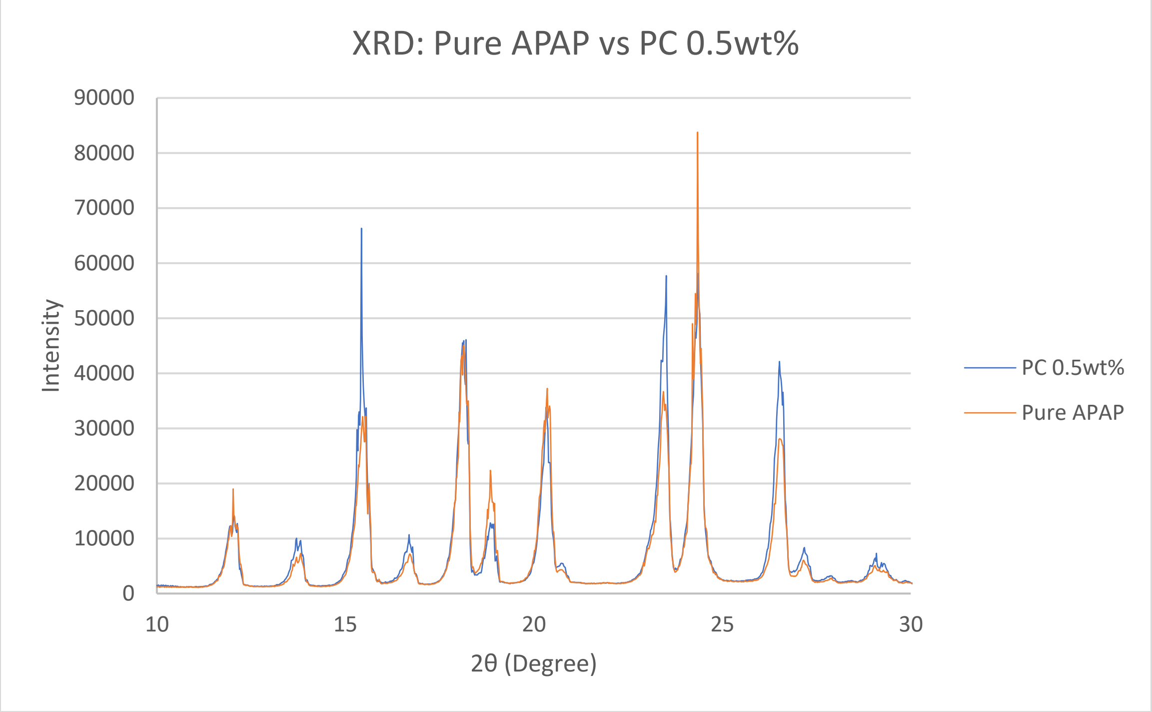

Figure 45: XRD comparison of Pure APAP and PC 0.5wt% between 10° ≤ 2θ ≤ 30°

Guar gum tablet GG 0.36wt% (Figure 46) shows slight increases in relative intensities at 15.5°, 18.2°, 23.5°, and 26.5°. GG 0.36wt% shows a slight increase in crystallinity in Table 4. Scherrer's Method shows that GG 0.36wt% has a higher lattice strain at 23.4° and 24.3° than APAP but a lower strain at 18.1° from Table 5. The crystallite size is higher than APAP at 18.1°, but lower at 23.4 and 24.2° peaks also from Table 5. Hall's method shows that GG 0.36wt% has a lower crystallite size and lattice strain average between 10 and 30° compared to APAP in Table 6.

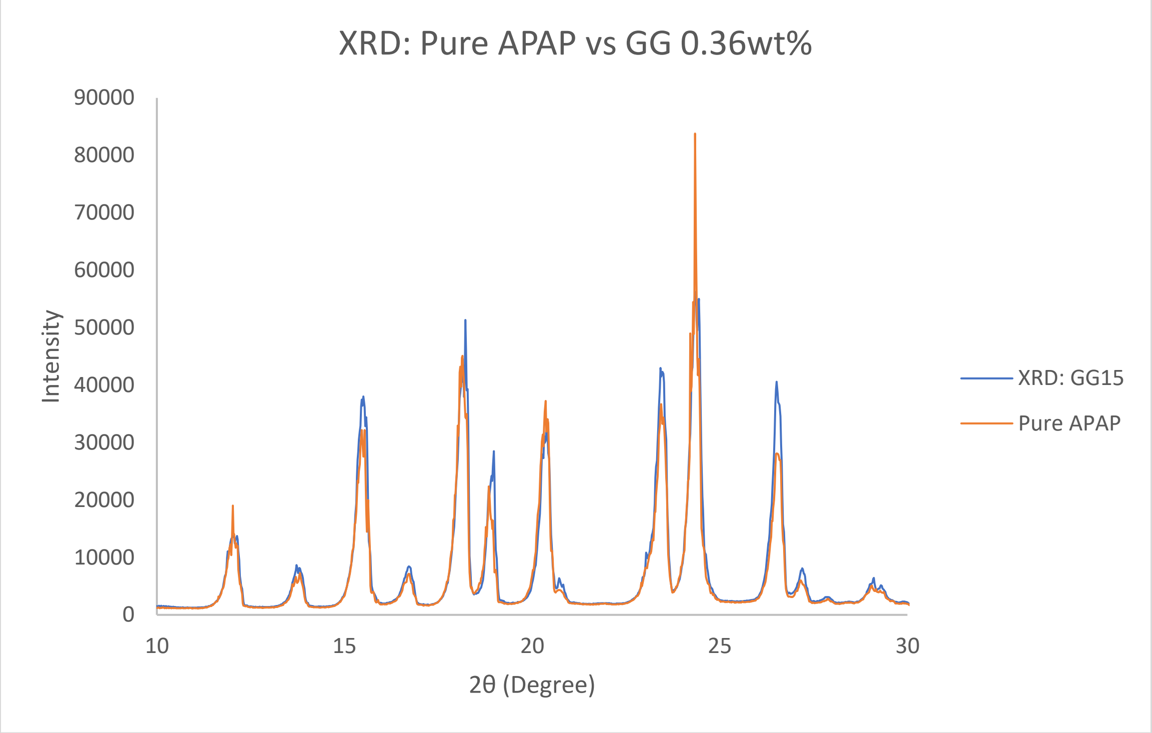

Figure 46: XRD Comparison of Pure APAP and GG 0.36wt% between 10° ≤ 2θ ≤ 30°

D-allulose tablet DA 13.86wt% (Figure 47) shows higher relative intensities at 15.5, 18.2, and 26.5° peak locations. Crystallinity calculations show that DA 0.13.86wt%'s crystallinity percentage is only slightly lower than pure APAP at 65.74% shown in Table 4. Scherrer's Method shows that the DA tablet has a higher lattice strain at 18.1 and 23.4°, while the strain is lower at 24.3° in Table 5. Crystallite size on the other hand is the opposite, where the crystallite size is larger at 18.1 and 23.4°, but lower at 24.3° shown in Table 6. Hall's Method calculations show that DA 13.86wt% has a lower crystallite size and lattice strain average between 10 and 30° in Table 7.

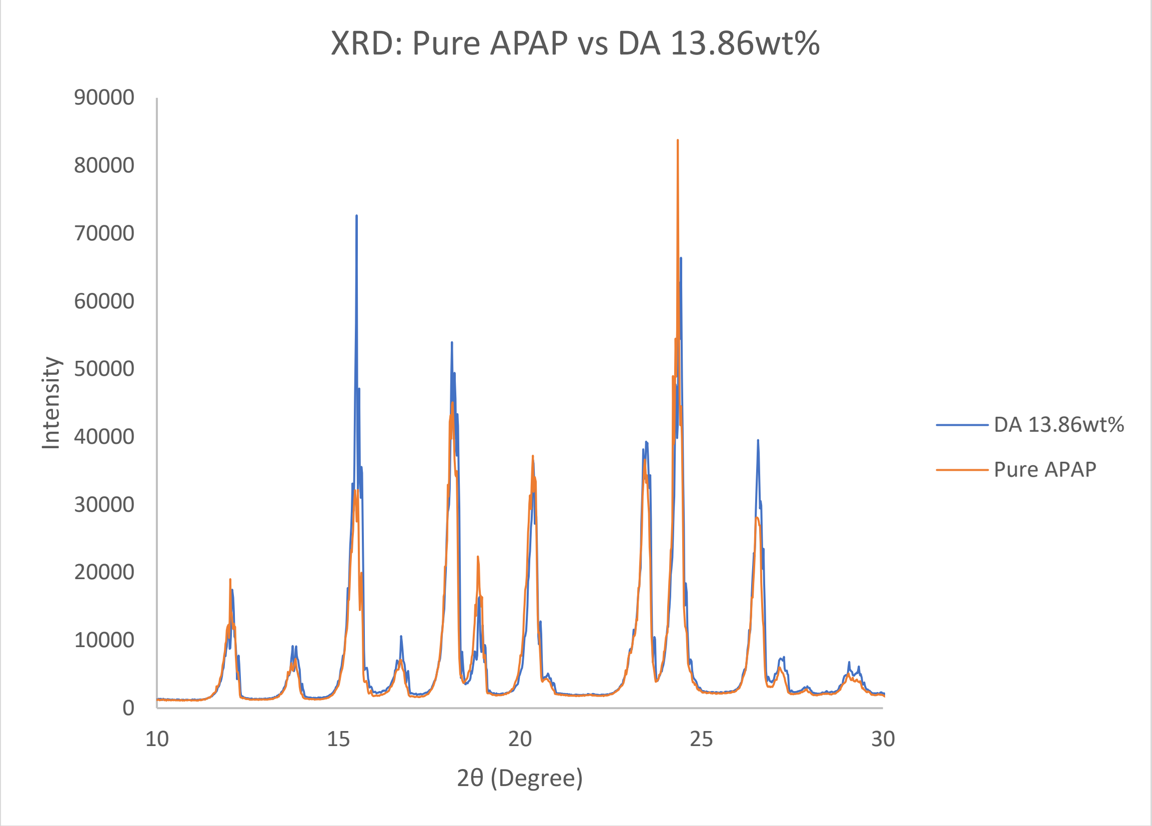

Figure 47: XRD Comparison of Pure APAP and DA 13.86wt% between 10° ≤ 2θ ≤ 30°

Table 4: Crystallinity Calculation Summary

		Crystallinity Calculation		
		Crystallinity (%)	Crystal Icr (kcps*deg)	amorphous Ia (kcps*deg)
API	APAP	66.97	51.20	25.26
Synthetic	PEG5	69.97	51.86	22.27
	PEG10	66.37	55.78	28.27
	PEG15	66.10	55.43	28.43
Sugars	DS25	67.44	51.68	24.96
	DS50	62.40	49.85	30.04
	DS75	60.61	45.96	29.90
	DA5	65.74	54.35	28.33
Polysaccharides	TM0.1wt%	71.44	54.45	21.77
	TM0.25wt%	67.92	53.97	25.50
	TM0.50wt%	68.72	56.87	25.88
	XN0.25wt%	68.70	55.34	25.21
	PC0.25wt%	70.45	53.78	22.56
	GG15	69.97	55.45	23.80

Table 5: Scherrer’s Method Lattice Strain

		Lattice Strain		
	Nearest Peak (2θ):	18.104	23.402	24.276
API	APAP	7.83E-03	4.37E-03	5.60E-03
Synthetic	PEG5	6.83E-03	5.83E-03	5.17E-03
	PEG10	7.17E-03	5.93E-03	5.57E-03
	PEG15	7.07E-03	5.40E-03	5.87E-03
Sugars	DS25	8.67E-03	4.33E-03	5.77E-03
	DS50	8.87E-03	3.87E-03	4.77E-03
	DS75	7.03E-03	4.10E-03	4.13E-03
	DA5	7.97E-03	5.13E-03	3.87E-03
Polysaccharides	TM0.1wt%	7.53E-03	4.33E-03	5.23E-03
	TM0.25wt%	8.23E-03	2.50E-03	3.63E-03
	TM0.50wt%	5.30E-03	4.53E-03	4.37E-03
	XN0.25wt%	7.20E-03	3.37E-03	4.00E-03
	PC0.5wt%	7.27E-03	2.77E-03	6.07E-03
	GG15	7.13E-03	4.63E-03	6.27E-03

Table 6: Scherrer's Method Crystallite Size

		Crystallite Size (Å)		
	Nearest Peak (2θ):	18.104	23.402	24.276
API	APAP	656.7	905.0	682.4
Synthetic	PEG5	672.5	783.7	729.6
	PEG10	719.2	684.0	687.3
	PEG15	726.6	742.3	651.0
Sugars	DS25	592.9	934.0	667.3
	DS50	582.9	1033.1	836.5
	DS75	734.2	979.4	951.2
	DA5	648.9	777.2	990.5
Polysaccharides	TM0.1wt%	683.6	934.4	733.1
	TM0.25wt%	626.2	1577.2	1083.2
	TM0.50wt%	985.5	886.1	891.0
	XN0.25wt%	718.2	1197.4	966.7
	PC0.5wt%	710.8	1381.7	635.2
	GG15	722.7	856.7	611.8

Table 7: Hall’s Method Results

	Sample	Crystallite Size (Å)	Lattice Strain
API	APAP	547.2	-2.13E-03
Synthetic	PEG 3wt%	738.2	2.70E-03
	PEG 6wt%	416.7	-3.97E-03
	PEG 9wt%	450.2	-3.67E-03
Sugars	DS 4.33wt%	495.7	-3.40E-03
	DS 8.67wt%	448.6	-4.30E-03
	DS 13wt%	330.6	-7.50E-03
	DA 13.86wt%	446.4	-4.17E-03
Polysaccharides	TM 0.1wt%	530.5	-2.07E-03
	TM 0.25wt%	560.6	-2.87E-03
	TM 0.5wt%	494.6	-3.40E-03
	GG 0.36wt%	417.8	-5.40E-03
	XN 0.25wt%	469.5	-4.30E-03
	PC 0.5wt%	501.3	-3.43E-03

4.5 Task 5: FTIR Results

Pure excipients were also analyzed using FTIR to better understand the chemical structure, and how they may influence APAP during the wet granulation process.

The raw scan of APAP was taken between 4000 cm^{-1} and 650 cm^{-1} shown in Figure 48. O-H stretching is observed at 3326 cm^{-1}, while CH3 stretching is found between 3156-3037 cm^{-1}. The C=O and aromatic ring stretching (C=C-C) are observed at 1649 and 1612 cm^{-1} respectively. N-H amide bending appears at 1560 cm^{-1}, while the C-H bond appears at 1507 cm^{-1}. C-C stretching appears at 1432 cm^{-1}. C-H symmetrical bending appears at 1373 and 1328 cm^{-1}. C-N aryl stretching appears at 1254 and 1224 cm^{-1}. C-O stretching and C-N amide stretching appear at 1172 and 970 cm^{-1} respectively.

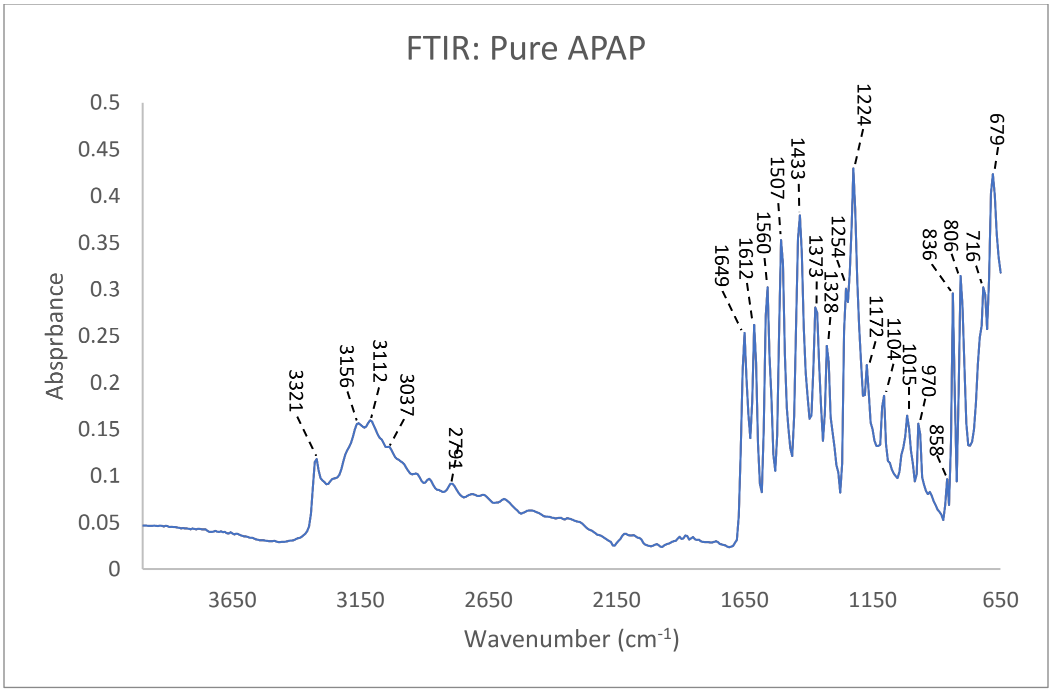

Figure 48: FTIR Spectra of Pure Paracetamol

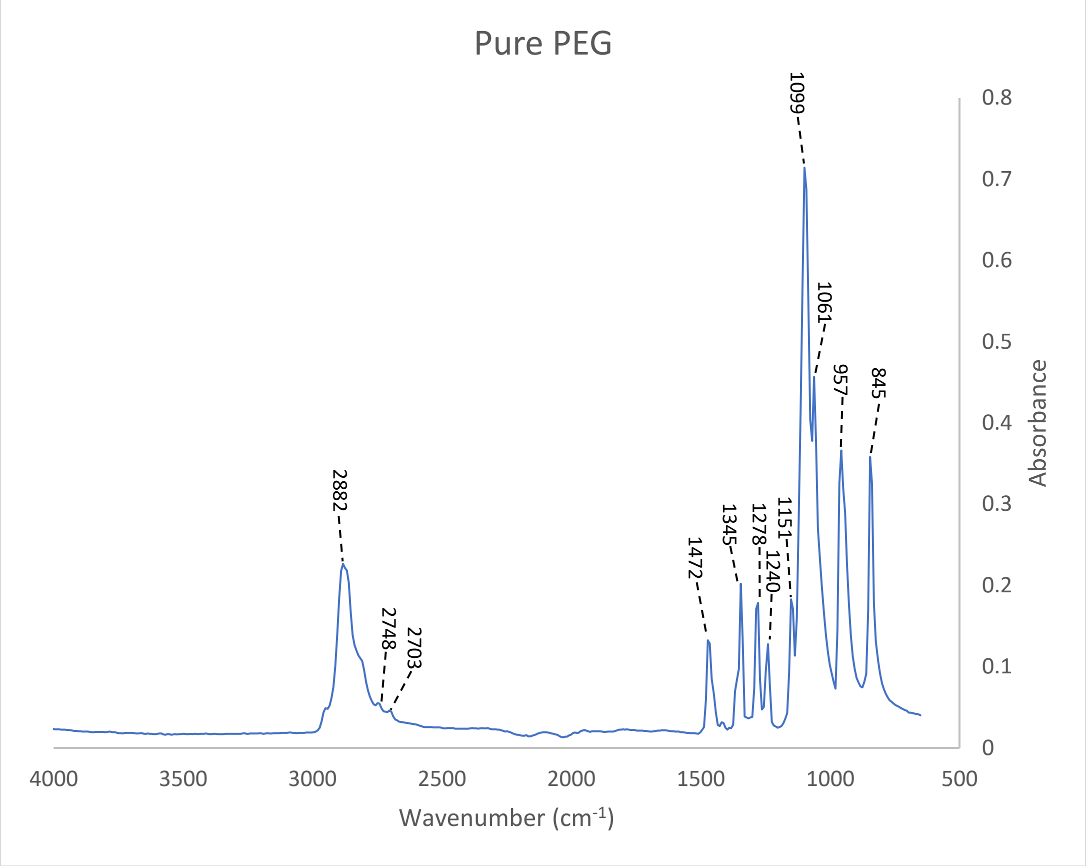

Figure 49: FTIR Spectra of Pure Poly (Ethylene Glycol)

Spectra of Pure PEG (Figure 49) contains peaks located at 2882 and 2748 cm^{-1} responsible for CH_2 symmetrical stretching and CH_2 deformations on CH_2 stretching respectively [47]. Sharp peaks at 1472 cm^{-1} are contributed to in-plane scissoring of the CH_2 groups, while 1345 and 1278 cm^{-1} are due to OH in-plane deformations [47]. The peak located at 1240 cm^{-1} is a result of C-O-C asymmetric stretching, while 957 and 845 cm^{-1} are contributed to C-C skeletal stretching [47].

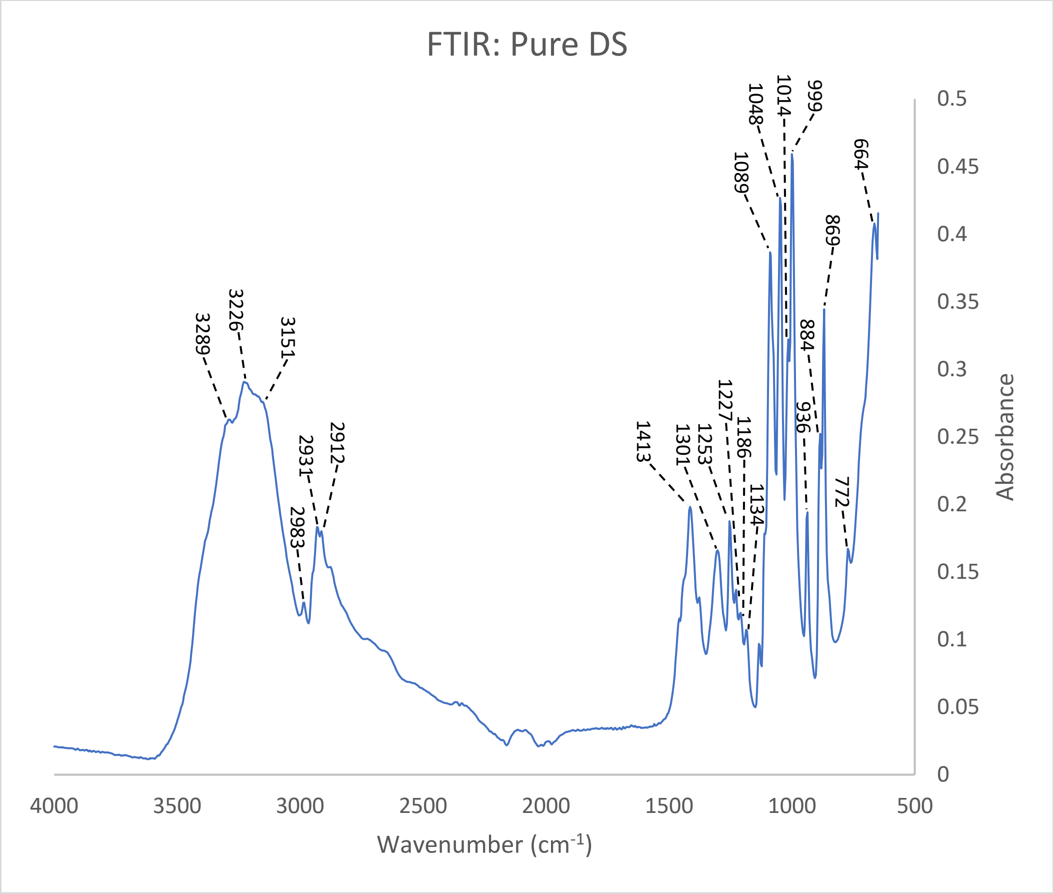

Figure 50: FTIR Spectra of Pure D-Sorbitol

DS spectra (Figure 50) show multiple peaks related to the -OH hydroxyl group stretch at 3289, 3225, and 3151 cm^{-1}. The peaks located at 2931 and 2912 cm^{-1} are a result of methylene C-H asymmetrical stretching, while 1458 cm^{-1} is a result of methylene C-H bending [48].

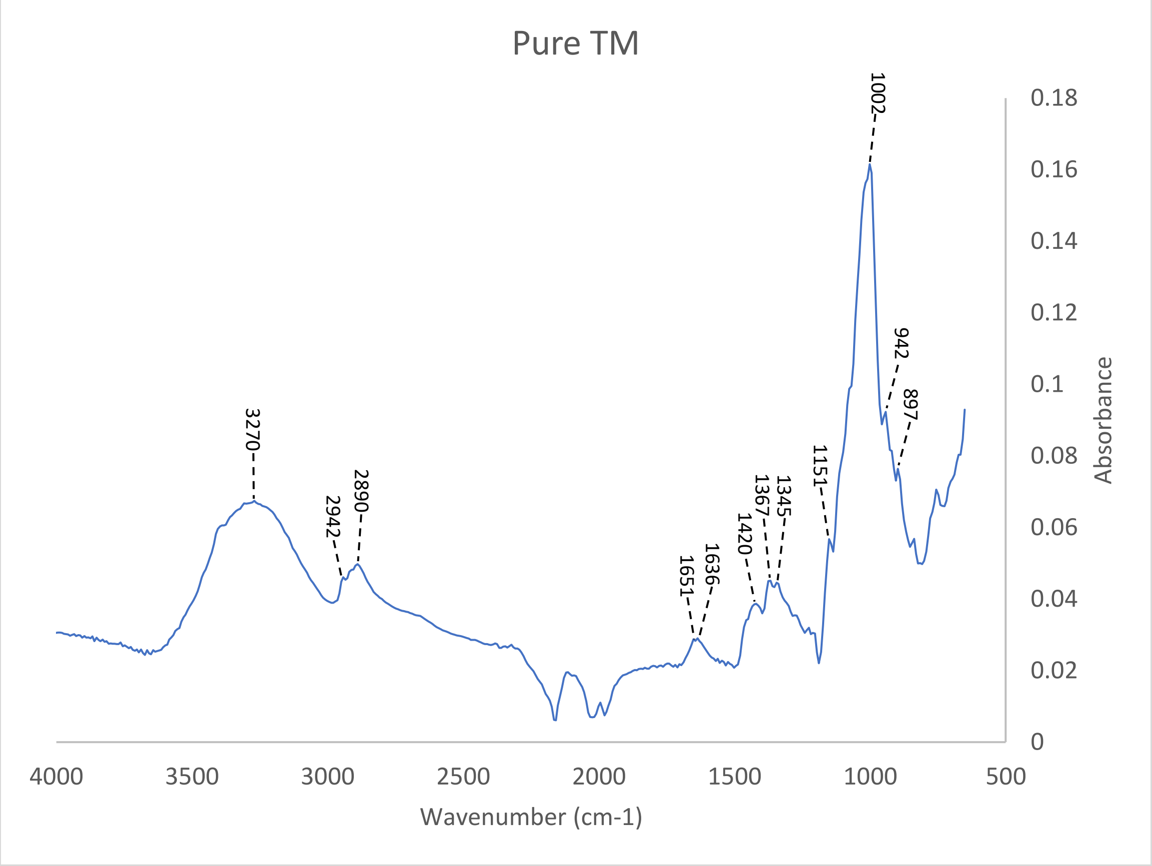

Figure 51: FTIR Spectra of Pure Tamarind Gum

TM spectra (Figure 51) contains multiple peaks that result from Hydroxyl -OH stretching at 3390, 3307, and 3270 cm^{-1} [48] [49]. Where methylene C-H stretching is responsible for peaks located between 2950-2800 cm^{-1}, and methylene C-H bending at 1420 cm^{-1} [49]. The peak located at 1002 cm^{-1} is a result of CH_2-O-CH_2 twisting vibrations [50].

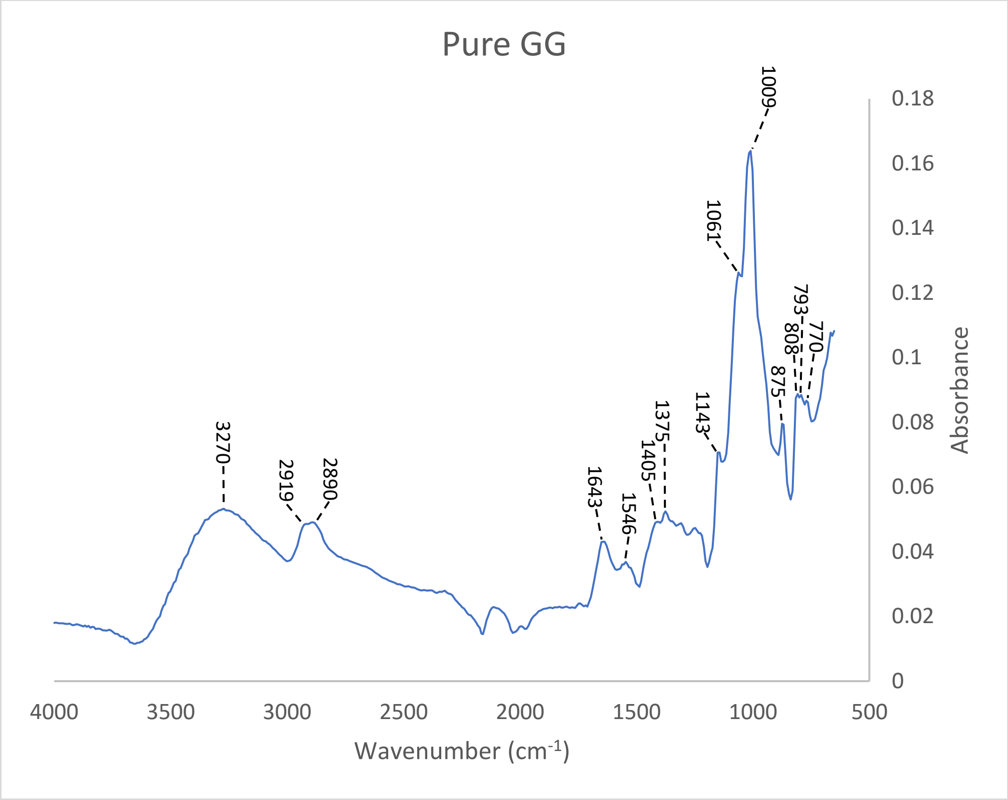

Figure 52: FTIR Spectra of Pure Guar Gum

Pure GG spectra (Figure 52) also contain a broad peak located at 3270 cm^{-1} because of hydroxyl group OH stretching [48]. Both peaks located at 2919 and 2890 cm^{-1} are a result of methylene CH asymmetric stretching, while 1643 cm^{-1} results from ring stretching [48] [51]. Peaks located at 1143 and 1061 cm^{-1} are the result of C-OH and primary alcoholic CH_2OH stretching [51]. Peaks located at 875 and 770 cm^{-1} are responsible for D-galactose and D-mannose of 1-4 and 1-6 linkages respectively [51] [52].

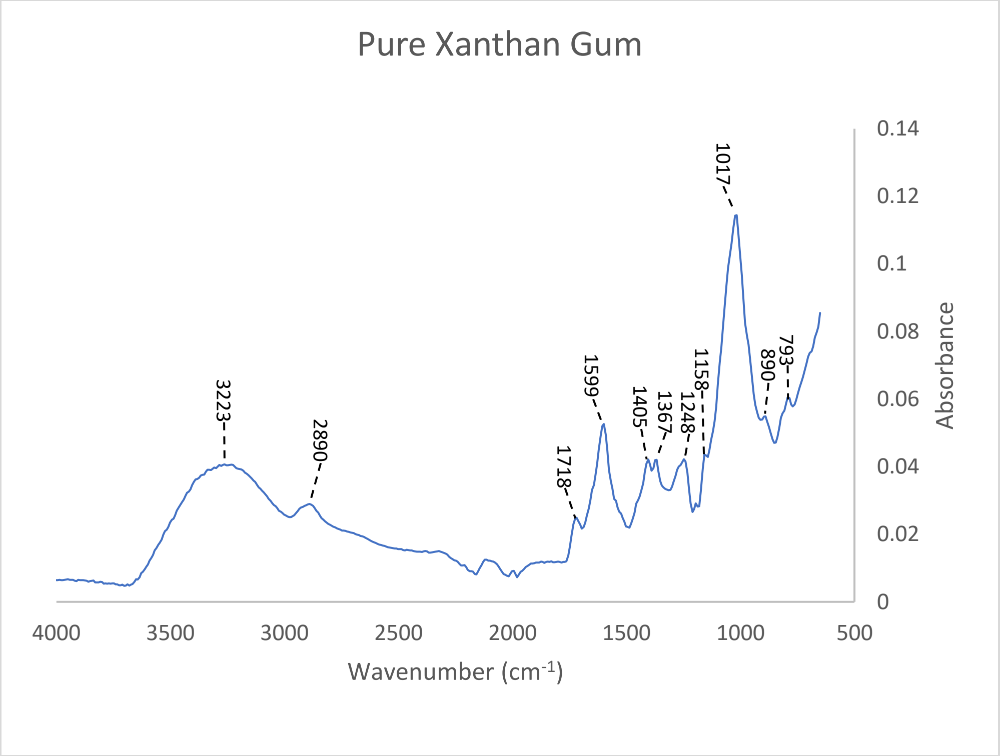

Figure 53: FTIR Spectra of Pure Xanthan Gum

Spectra of pure XN (Figure 53) contain a broad peak at 3233 cm^{-1} resulting from OH stretching vibration [48], while the peak located at 2890 cm^{-1} is a result of CH stretching [48]. The peak located at 1718 cm^{-1} is possibly a result of the free carboxylic acid or ester group [53]. Both peaks located at 1599 and 1405 cm^{-1} are due to the asymmetric stretching of C=O bonds near the carboxylate anion [53]. Peaks located at 1248 and 1017 cm^{-1} are a result of OH bend from the primary hydroxyl group in XN's backbone, and CO stretching coupled to adjacent CC bond stretching respectively [53].

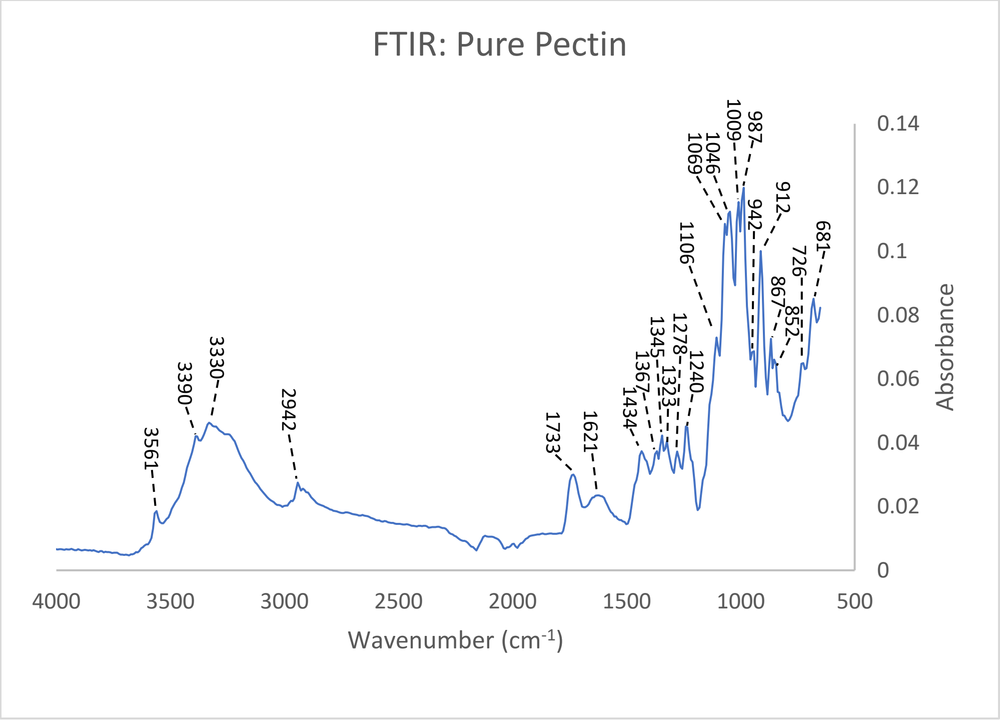

Figure 54: FTIR Spectra of Pure Pectin

Pure PC spectra (Figure 54) peaks located between 3570 to 3200 cm^{-1} are a result of Hydroxyl group OH stretching [48]. Both peaks located at 2941 and 2919 cm^{-1} is from PC's CH stretching [48], while 1434 cm^{-1} are the result of CH2 scissoring [54]. The peak located at 1106 and 1046 cm^{-1} is a result of CH-OH secondary alcohol and CH-O-CH stretching respectively [54].

Both DS75 and DA5 show an increase in the base scan before 3320 cm^{-1}, which is responsible for APAP’s O-H functional group. Signaling that DS and DA are interacting with APAP’s alcohol group shown in Figure 55. PEG is also compared with pure APAP, where peaks responsible for PEG’s CH2 symmetrical stretching and C-O-C asymmetric stretching are visible. Polysaccharide excipients including TM, GG, PC, and XN have shown minuscule change when compared to APAP shown in Figure 56.

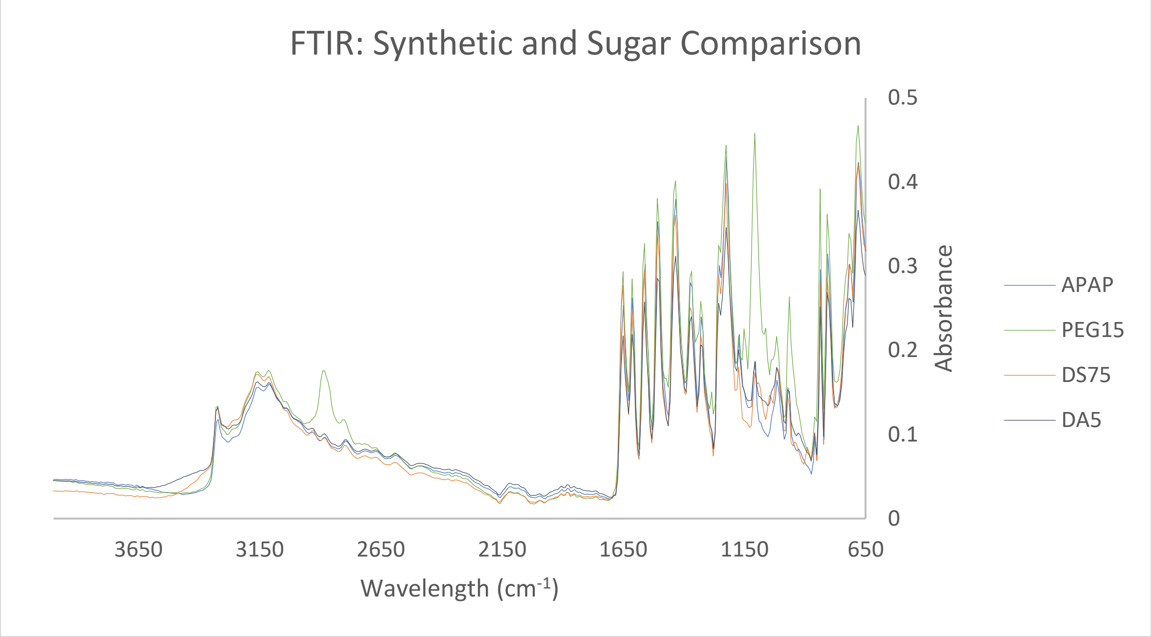

Figure 55: FTIR comparison of Pure APAP with Synthetic and Sugar Tablets

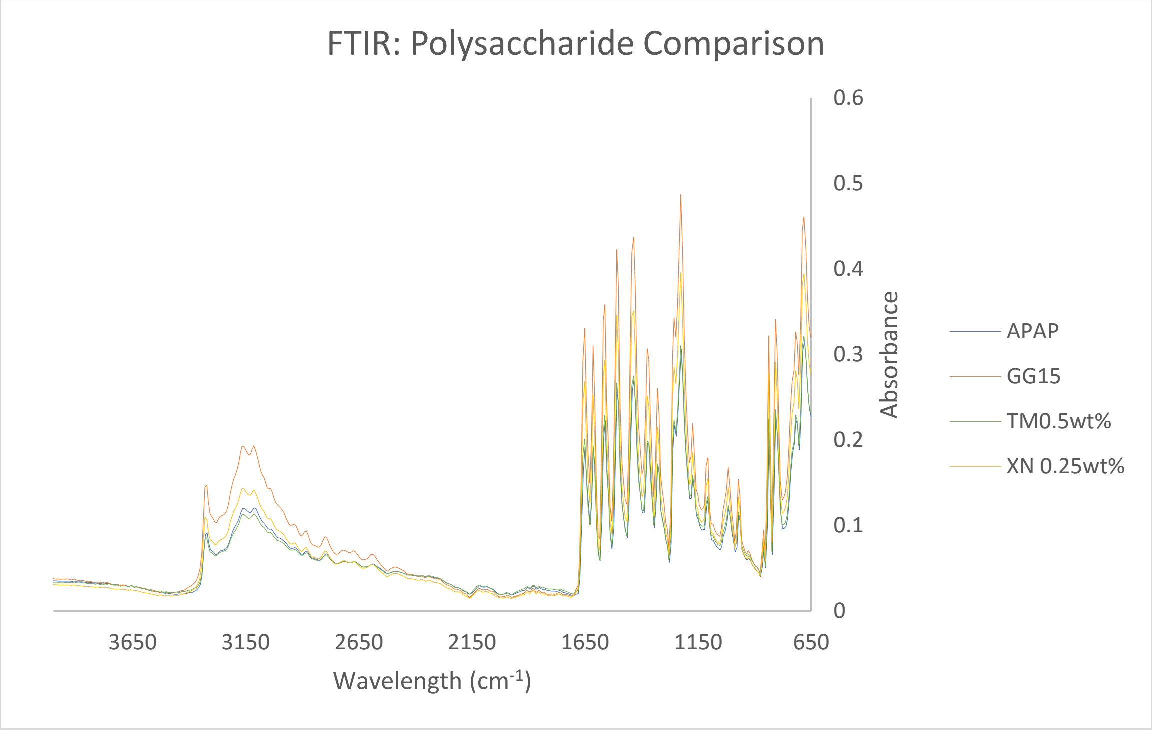

Figure 56: FTIR comparison of Pure APAP and Polysaccharide Tablets

4.4 Task 6: DSC Results

PEG reduces both the cold crystallization and melting point peak and onset temperatures shown in Figure 57 and Table 7 when compared to pure APAP. The required heat flow to reach the peaks was also reduced compared to pure APAP. A correlation is also present with the concentration of PEG in the tablet matrix, with increased concentration of PEG the lower the cold and melting peak and onset temperatures.

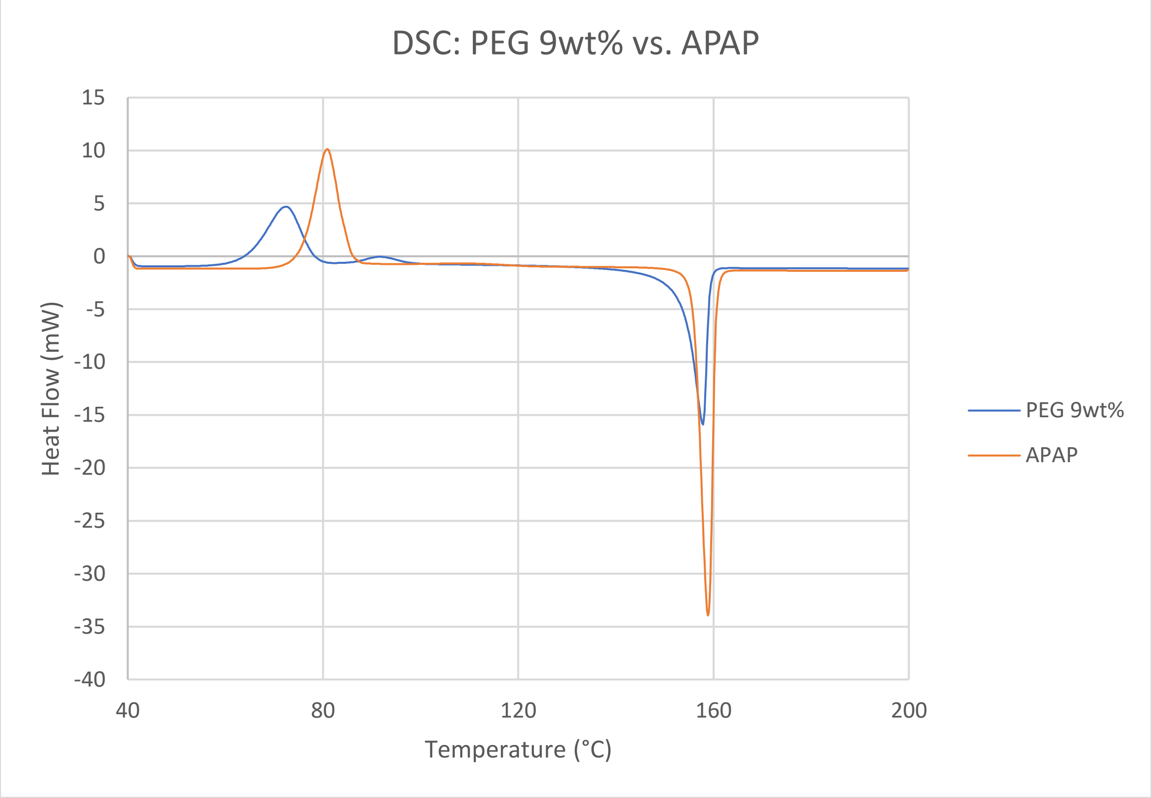

Figure 57: DSC PEG 9wt% vs APAP

It is also observed that with increasing concentration of PEG, the heat flow required to reach the cold crystallization and melting point decreases shown in Figure 58. Pure APAP used for comparison has a crystallization temperature of 81.13°C, and a melting temperature of 160.42°C. The crystallization and melting temperature are comparable with the literature finding that the crystallization peak is between 70 to 80°C and melting is at 156.2°C.

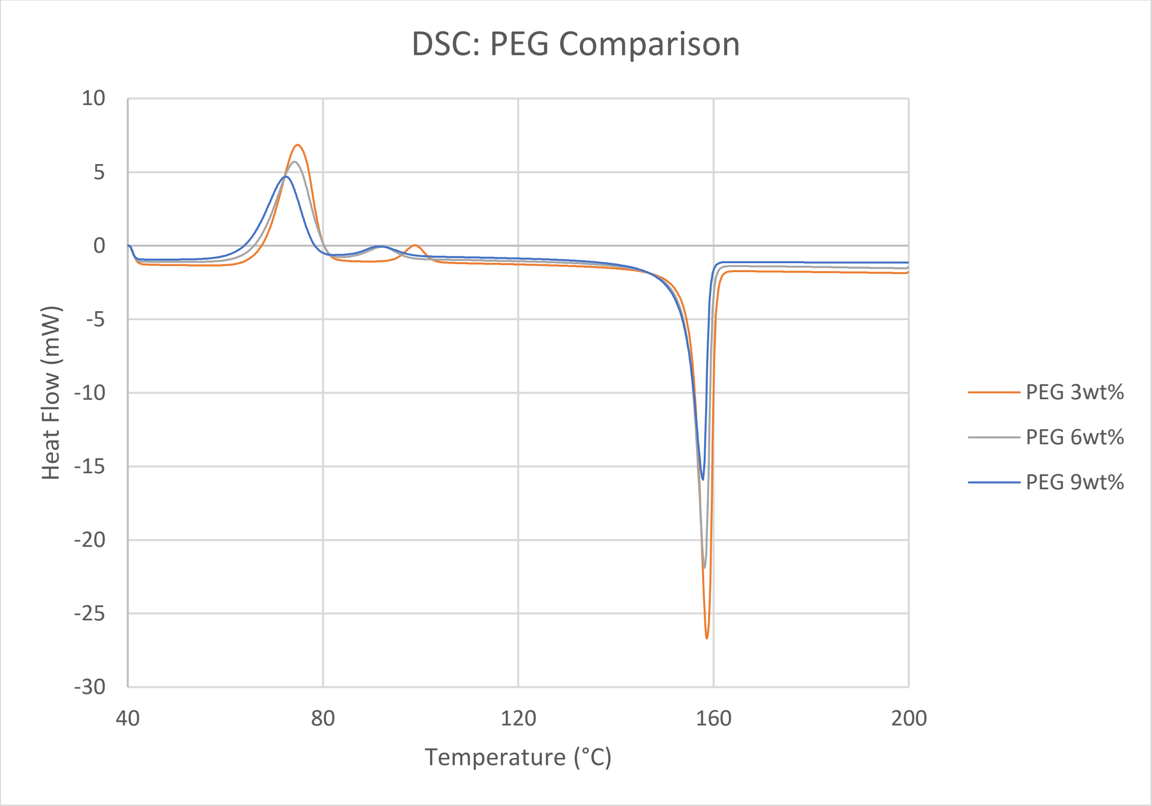

Figure 58: DSC PEG Tablet Comparison

D-sorbitol in the tablet matrix reduces the cold crystallization peak, and the melting peak temperatures. The reduction is expressed by the lower onset temperatures for both crystallization and melting peaks. Figure 59 compares the DSC scans of DS50 and APAP, where DS50 has a considerable shift to the left. This is due to DS reducing the melting point of the DS tablet.

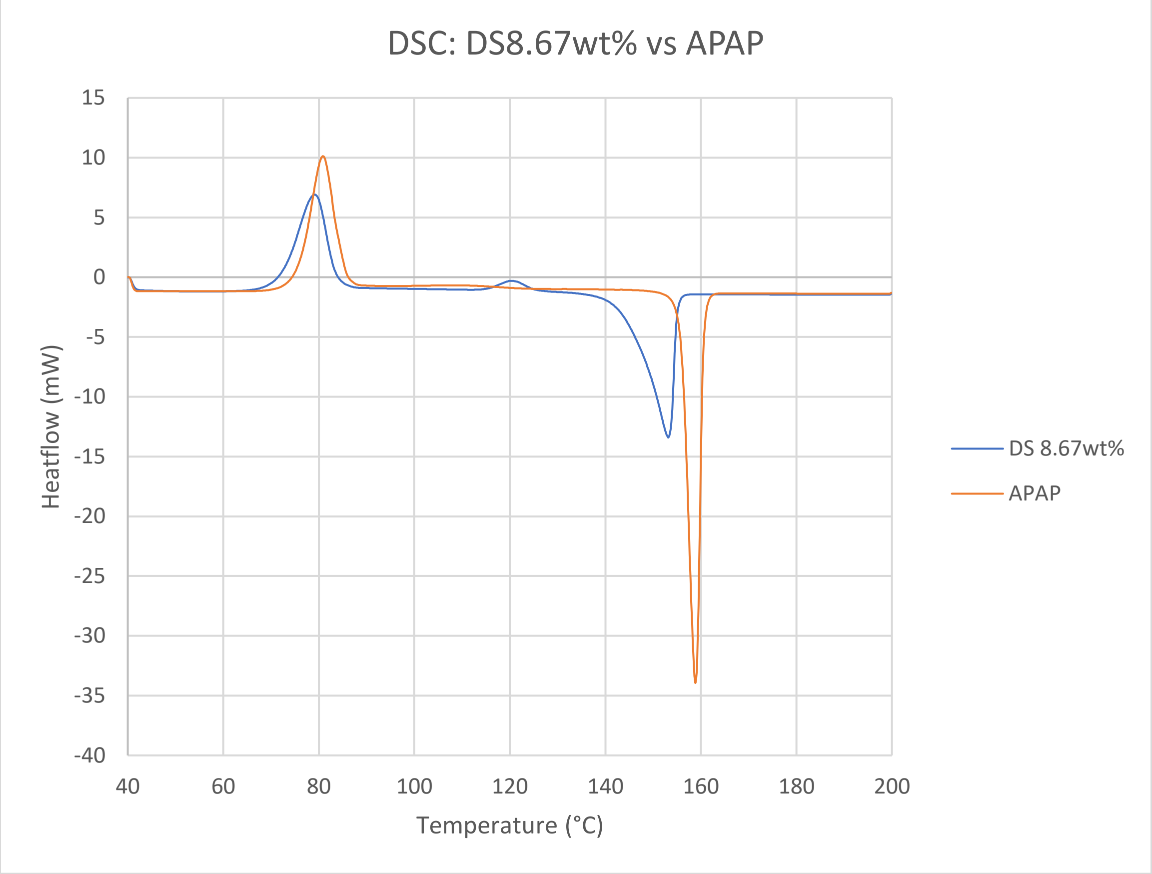

Figure 59: DSC: DS50 vs APAP

A correlation between different DS concentrations is not present in the peak temperature, onset, and endset values. All concentrations of DS show a reduction in the cold crystallization, and melting point temperature of APAP in Figure 60.

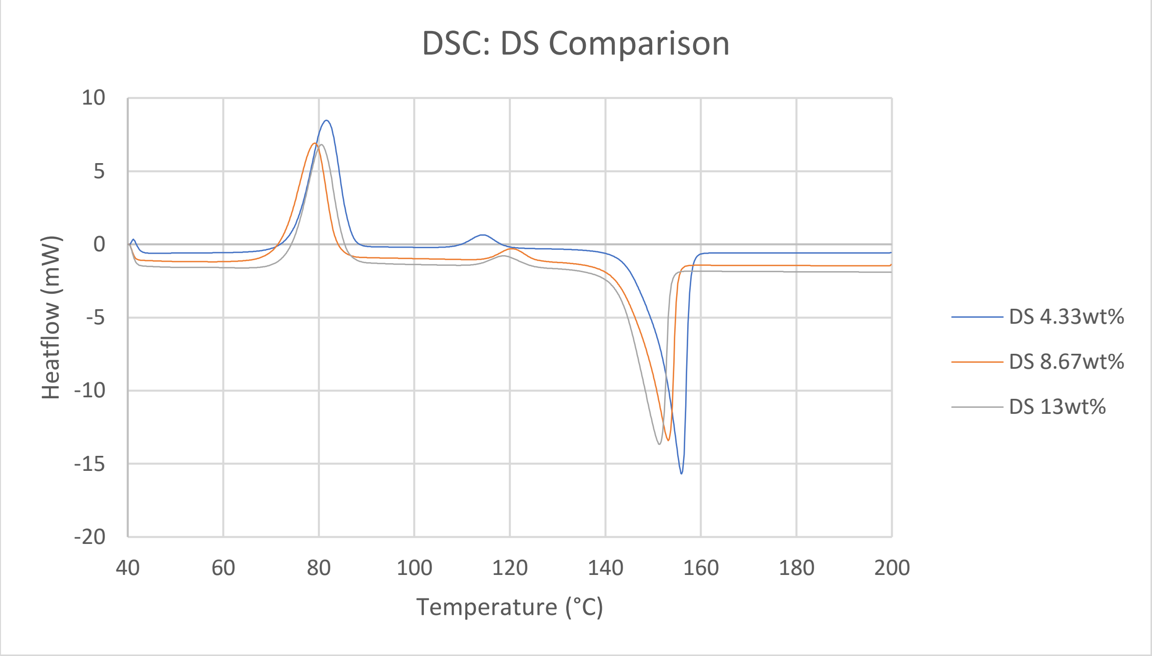

Figure 60: DSC: DS Tablet Comparison

Tamarind gum shows a slight correlation for the peak, onset, and endset temperature at the cold crystallization, and melting peaks. As the TM concentration increases the peak, onset, and endset temperatures decrease for the crystallization and melting peaks. TM tablets also have a lower melting point than pure APAP, as shown in Table 7. The DSC scans for TM0.25wt% and APAP are compared in Figure 61, where the TM tablet has a lower heat flow for the crystallization and melting peak.

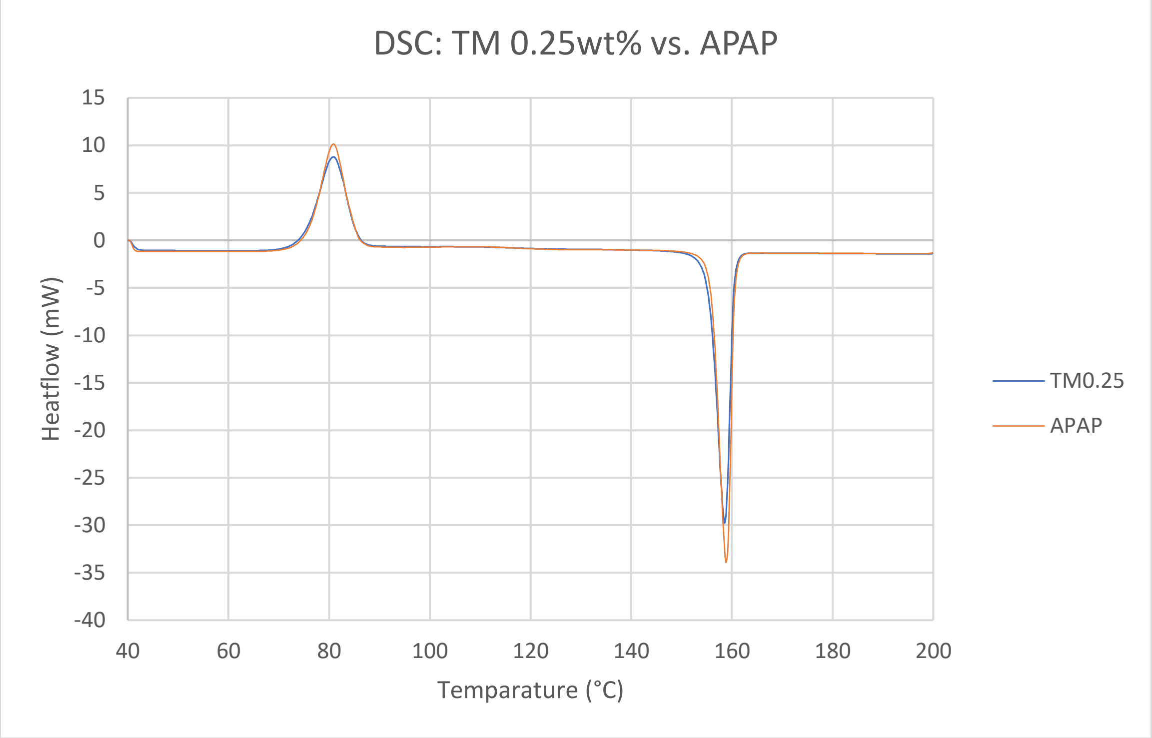

Figure 61: DSC: TM0.25wt% vs APAP

Figure 62 shows TM tablets at three concentrations including 0.1wt%, 0.25wt%, and 0.5wt%. A higher TM concentration (TM 0.5wt%) resulted in an endset value lower than pure APAP, while the opposite was true for a lower TM concentration (TM 0.1wt%). What is observed from the endset values is also true for the cold crystallization peak temperatures.

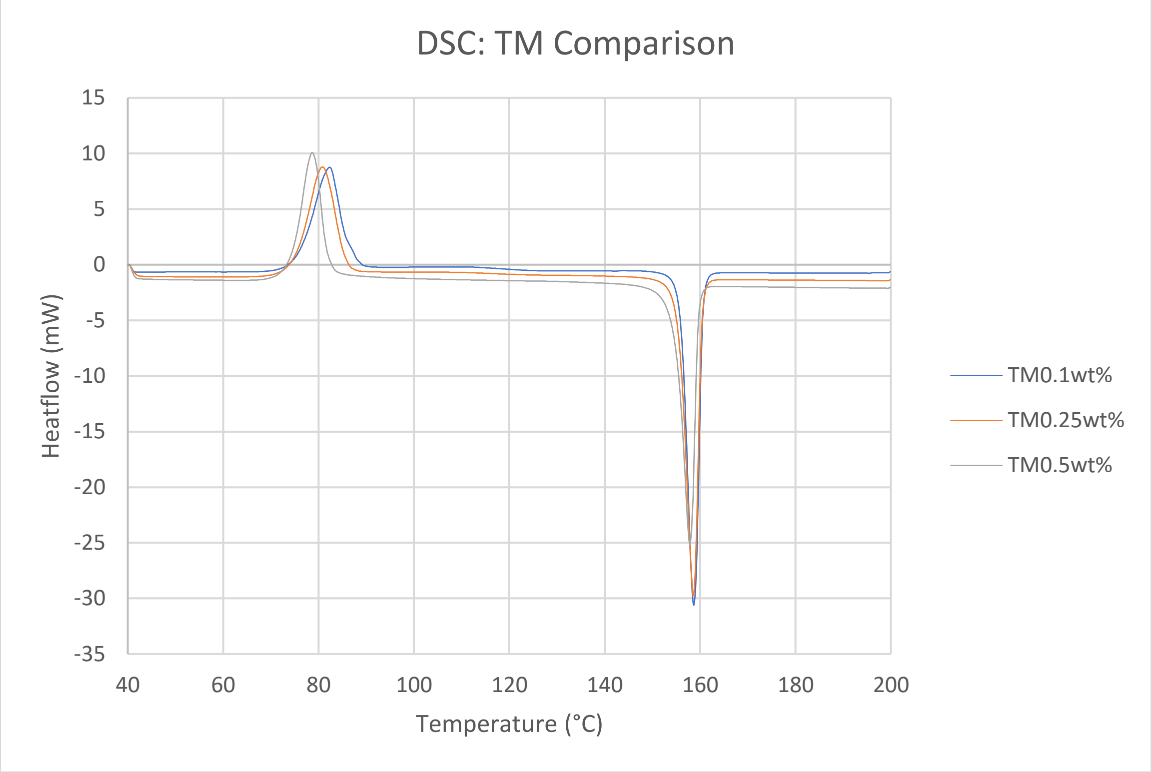

Figure 62: DSC: TM Tablet Comparison

The use of guar gum also lowers the cold crystallization and melting temperature of APAP. GG 0.36wt% has a lower onset temperature for the melting and crystallization peaks. While the peak temperature is lower for the melting peak but higher for the crystallization peak. The endset values are higher for the crystallization peak, and slightly lower for the melting peak compared to APAP. Pectin like other polysaccharides gaur gum and tamarind gum, also slightly reduces the melting point of the tablet. PC slightly reduced the peak onset and endset values for both the crystallization and melting peaks. Xanthan gum in the tablet matrix reduces the melting temperature of the tablet as shown by a lower onset and peak temperature. The crystallization peak has a higher peak temperature but a lower onset temperature. Unlike the other tablets, XN 0.25wt% has a higher endset temperature for the melting peak and an endset temperature slightly lower than GG0.36wt% for the crystallization peak. DA 13.86wt% decreased the melting and cold crystallization peak of the tablet. Figure 63 shows the comparison between pure APAP, XN, PC, GG, and DA tablets

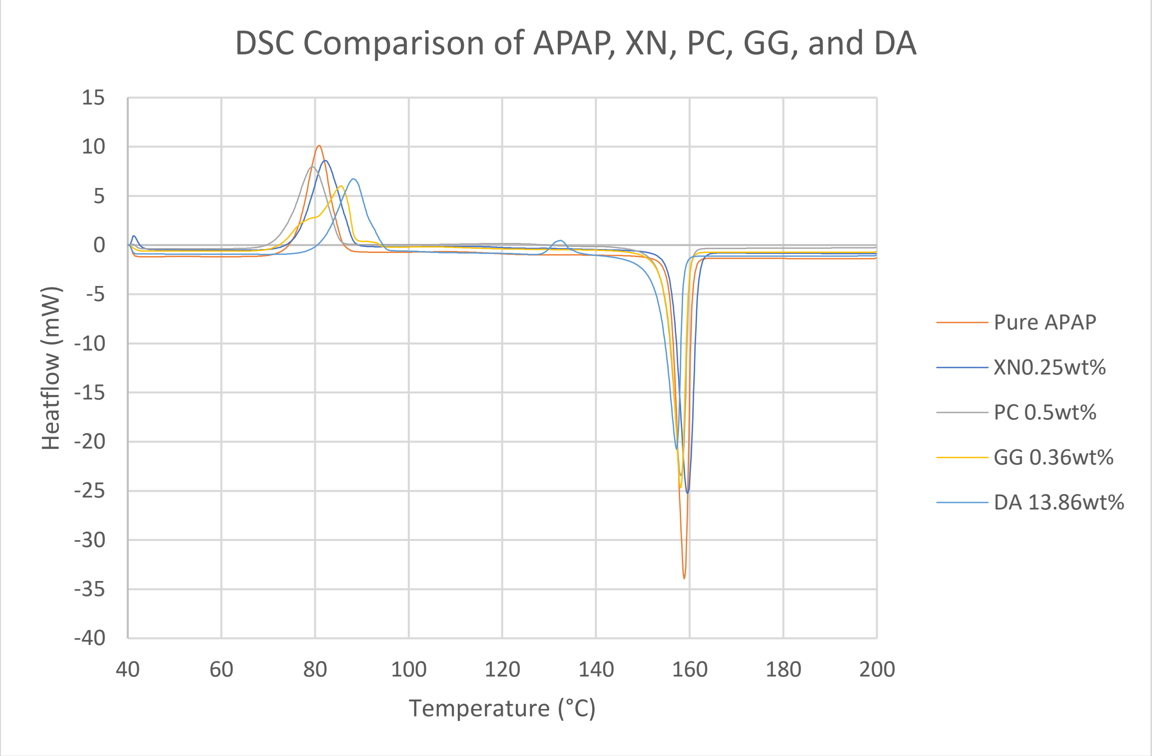

Figure 63: DSC Comparison of APAP, XN, PC, GG, and DA

Table 7: DSC Summary of Peak and Onset Temperatures

	Peak (°C)		Onset (°C)	
Sample	Cold	Melting	Cold	Melting
APAP	81.13	160.42	80.83	158.83
DS 4.33wt%	81.5	156	74.76	149.58
DS 8.67wt%	79.37	152.64	71.91	145.45
DS 13wt%	80.5	151.33	73.94	142.82
TM0.1wt%	82.33	158.67	75.76	155.88
TM0.25wt%	80.83	158.5	74.9	155.39
TM0.5wt%	78.67	157.83	74.22	154.68
PEG 3wt%	75.03	157.59	67.49	155.08
PEG 6wt%	74.33	157.29	66.19	154.36
PEG 9wt%	72.63	157.19	64.18	153.38
GG 0.36wt%	80.81	158.33	74.88	155.82
PC0.25wt%	80.17	158.67	80.17	155.53
XN0.25wt%	82.17	159.5	76.02	156.06
DA 13.86wt%	88.37	156.33	81.15	152.96

5. SUMMARY AND CONCLUSIONS

The research was conducted with a focus on multiple tasks. Task 1 was to establish an improved method to create APAP granules using wet granulation. Tasks 2 and 3 used disintegration and dissolution respectively to analyze how the granule would break apart and dissolve. Task 4 used XRD to analyze how the excipients interacted with APAP's crystal structure. Similar to Task 4, Task 5 utilized the FTIR to analyze how the excipient interacted with APAP's chemical structure. Task 6 used DSC, to analyze how the excipient affected the granule's thermodynamic properties.

After completing Task 1, 3D molds resulted in APAP tablets with a more uniform and consistent area, roundness, and aspect ratio compared to tablets created using the tray method making them more suitable for dissolution and disintegration. The tablets produced from the 3D mold were also able to handle a significantly higher compression force than tablets created from the tray method. Wet granulation with the 3D was also more successful with the use of an auto-desiccator at ambient conditions than with a vacuum and convection oven. While the 3D mold created uniform tablets, some of the APAP was stuck to the mold resulting in a reduced tablet weight once removed. Overall, the 3D mold is recommended over the tray method for the uniform tablets, and efficient use of APAP.

After completing Tasks 2 and 3, it is concluded that polysaccharides are better than sugars and synthetic PEG at sustained release. Xanthan gum was the only tablet that failed to disintegrate and had the slowest rate of dissolution. DS tablets have the most rapid disintegration time and rate of dissolution. DA on the other hand shared similar disintegration times with DS, and dissolution characteristics with TM and GG tablets.

Through the completion of Tasks 4-6, it is concluded that the natural excipients have no significant alterations to the structure of the API APAP. XRD analysis shows that the excipient will slightly influence the crystallinity, lattice strain, and crystallite size of APAP, but no significant changes were seen in the crystal structure which would signal the formation of a different compound. FTIR analysis showed that polysaccharide excipients did not affect the structure of APAP, while sugar excipients interacted with the -OH functional group. The synthetic excipient, PEG, had the greatest effect on the structure of APAP and was the only excipient that showed new functional group peaks at 2897, 2822, and 1106 cm^{-1} signaling a change in chemical structure, possibly interacting with APAP's CH_3 and C-O stretching respectively. DSC analysis proved that the addition of any excipient used during testing would reduce the maximum melting temperature of the APAP tablet. However, polysaccharides had the smallest effect on the APAP tablet thermodynamic properties followed by the synthetic PEG. D-sorbitol provided the highest reduction in melting peak and onset temperatures.

In conclusion, 3D molds are a great alternative method to create APAP tablets through wet granulation, due to their uniform shape and improved physical characteristics shown through compression tests. PEG excipient is a superior binder compared to natural binders when used in a two-ingredient matrix including one binder and API. On the other hand, FTIR has shown that each natural binder interacted with the APAP's chemical structure less than PEG. XRD and DSC results showed that natural ingredients can compete with PEG. It is recommended that the 3D molds should be improved to prevent the APAP from sticking to the walls. One suggestion is to create the molds using a more advanced 3D printer and a higher-quality polymer. Because this research has successfully investigated how natural excipients interact with APAP on an individual basis, new tests should analyze how mixtures of two or more natural ingredients will affect the tablet matrix and compare with synthetic PEG.

References

[1] Rhodes, M., Introduction to Particle Technology: Second Edition, John Wiley & Sons, 2008.

[2] Ennis, B., "Theory of Granulation: An Engineering Perspective," in *Handbook of Pharmaceutical Granulation Technology: Second Edition*, Research Triangle Park, North Carolina, U.S.A, Taylor & Francis Group, LLC., 2005, pp. 7-78.

[3] Kristensen, H. and Schaefer, T., "Granulation: A Review on Pharmaceutical Wet Granulation," *Drug Development and Industrial Pharmacy,* pp. Vol13 pp 803-372, 1987.

[4] He, L., Liu, L. and Lister, J., "Scale-Up Considerations in Granulation," in *Handbook of Pharmaceutical Granulation Technology*, Boca Raton, FL, Taylor & Francis Group, LLC, 2005, pp. 459-489.

[5] Li, Q., Rudolph, V., Weigl, B. and Earl, A., "Interparticle van der Waals force in powder flowability and compactibility," *International journal of pharmaceutics,* vol. 280, pp. 77-93, 2004.

[6] Markl, D. and Zeitler, J., "A Review of Disintegration Mechanisms and Measurement Techniques," *Pharmaceutical Research,* vol. 34, no. 5, pp. 890-917, 2017.

[7] Shirwaikar, A. and et al., "Herbal Excipients in Novel Drug Delivery Systems," *Indian Journal of Pharmaceutical Sciences,* pp. 415-422, August 2008.

[8] Amiri, M. and et al., "Plant-Based Gums and Mucilages Applications in Pharmacology and Nanomedicine: A Review," *Molecules,* March 22, 2021.

[9] Bhosale, R., Osmani, R. and Moin, A., "Natural Gums and Mucilages: A Review on Multifaceted Excipients in Pharmaceutical Science and Research," *International Journal of Pharmacognosy and Phytochemical Research,* pp. 901-912, 2014.

[10] Thombare, N., Jha, U. and Siddiqui, M., "Guar gum as a promising starting material for diverse applications: A review," *International Journal of Biological Macromolecules,* pp. 361-372, 2016.

[11] Shur, J., "Sorbitol," in *Handbook of Pharmaceutical Excipients: Sixth Edition*, Grayslake, IL, Pharmaceutical Press, 2009, pp. 679-682.

[12] Wallick, D., "Polyethylene Glycol," in *Handbook of Pharmaceutical Excipients; Sixth Edition*, Washington, DC., Pharmaceutical Press, 2009, pp. 517-522.

[13] Shah, H. and Singh, K., "Xanthan Gum," in *Handbook of Pharmaceutical Excipients: Sixth edition*, Washington D.C., Pharmaceutical Press, 2009, pp. 782-785.

[14] Cook, W., Quinn, M., and Shesky, P., "Pectin," in *Handbook of Pharmaceutical Excipients: Sixth Edition,* Washington D.C., Pharmaceutical Press, 2009, pp. 478-479.

[15] Kibbe, A., "Guar Gum," in *Handbook of Pharmaceutical Excipients: Sixth Edition,* Grayslake, IL, Pharmaceutical Press, 2009, pp. 298-300.

[16] Khaounvilay, K. and Sittikijyothin, W., "Rheological Behavior of Tamarind Seed Gum in Aqueous Solutions," *Food Hydrocolloids,* pp. 334-338, 2012.

[17] Joseph, J., Kanchalochana, S., Rajalakshmi, G., Hari, V. and Durai, R., "Tamarind seed polysaccharide: A promising natural excipient for pharmaceuticals," *International Journal of Green Pharmacy,* pp. 270-278, 2012.

[18] Hu, M., Li, M., Jiang, B. and Zhang, T., "Bioproduction of D-allulose: Properties, applications, purification, and future, perspectives," *Comprehensive Reviews in Food Science and Food Safety,* vol. 20, pp. 6012-6026, September 17, 2021.

[19] Zhang, W. and et al., "D-allulose, a versatile rare sugar: recent biotechnological advances and challenges," *Critical Reviews in Food Science and Nutrition,* 2021.

[20] American Chemical Society., "CAS Registry Number: 103-90-2," SciFinder, [Online]. Available: https://scifinder-n-cas-org.pvamu.idm.oclc.org/searchDetail/substance/62f3141a55641a06b2f14ed5/substanceDetails. [Accessed 8 August 2022].

[21] Patterson, T. and et al., "Deprescribing paracetamol in pain conditions: A scoping review," *Research in Social and Administrative Pharmacy*, vol. 18, pp. 3272-3283, 2022.

[22] Li, J. and Doherty, M., "Steady State Morphologies of Paracetamol Crystal from Different Solvents," *Crystal Growth and Design*, vol. 17, pp. 659-670, 2016.

[23] Bertolini, A. and et al., "Paracetamol: New Vistas of an Old Drug," *CNS Drug Reviews*, vol. 12, pp. 250-275, 2006.

[24] Botting, R. and Ayoub, S., "COX-3 and the mechanism of action of paracetamol/acetaminophen," *Prostaglandins Leukotrienes and Essential Fatty Acids*, vol. 72, pp. 85-87, 2005.

[25] Resnik, R., Misch's Avoiding Complications in Oral Implantology, 2018.

[26] Thi, Y., Rademann, K. and Emmerling, F., "Direct Evidence of Polyamorphism in paracetamol," *CrystEngComm*, vol. 17, no. 47, pp. 8967-9244, 2015.

[27] Nezzal, A. and et al., "Polymorphism of Sorbitol," *Journal of Crystal Growth*, pp. 3863-3870, 2009.

[28] PubChem, National Library of Medicine, [Online]. Available: https://pubchem.ncbi.nlm.nih.gov/compound/Sorbitol. [Accessed 14 October 2022].

[29] Krishnaiah, Y. and et al., "Development of colon targeted drug delivery systems for mebendazole," *Journal of Controlled Release,* pp. 87-95, 2001.

[30] Willats, W. and et al., "Pectin: Cell Biology and Prospects for Functional Analysis," *Plant Molecular Biology,* pp. 9-27, 2001.

[31] Katzbauer, B., "Properties and applications of xanthan gum," *Polymer Degradation and Stability,* pp. 81-84, 1998.

[32] Kimmura, T. and et al., "D-allulose enhances postprandial fat oxidation in healthy humans," *Applied Nutritional Investigation,* Vols. 43-44, pp. 16-20, 2017.

[33] Smith, B., Remington Education: Physical Pharmacy, Pharmaceutical Press, 2016.

[34] Askeland, D. and Wright, W., The Science and Engineering of Materials: Seventh Edition, Boston, MA: Cengage Learning, 2016.

[35] Chaturvedi, K., "Contribuition of Crystal Lattice Energy on the Dissolution Behavior of Eutectic Solid Dispersions," *ACS Omega,* pp. 9690-9701, 2020.

[36] Ramteke, K., Dighe, P., Kharat, A. and Patil, S., "Mathematical Models of Drug Dissolution: A Review," *Scholars Academic Journal of Pharmacy,* pp. pp 388-396, 2014.

[37] Wu, I. and et al., "Interpreting non-liner drug diffusion data: Utilizing Korsmeyer-Peppas model to study drug release from liposomes," *European Journal of Pharmaceutical Sciences,* p. vol 138, July 29, 2019.

[38] Quodbach, J. and Kleinebudde, P., "A critical review on tablet disintegration," *Pharmaceutical Development and Technology,* vol. 21, no. 6, pp. 763-774, 2016.

[39] Moore, E., Fourier Transform Infrared Spectroscopy (FTIR): Methods, Analysis and Research Insights, Hauppauge, NY: Nova Science Publishers, Inc, 2017.

[40] Mallah, M. and et al., "A rapid Fourier-transform infrared (FTIR) spectroscopic method for direct quantification of paracetamol content in solid pharmaceutical formulations," *Spectrochimica Acta Part A: Molecular and Biomolecular Spectroscopy,* pp. 64-70, 2015.

[41] Gaffney, J., Marley, N., and Jones, D., "Fourier Transform Infrared (FTIR) Spectroscopy," *Characterization of Materials,* pp. 1104-1135, 2012.

[42] Chiu, M. and Prenner, E., "Differential Scanning Calorimetry: An invaluable tool for a detailed thermodynamic characterization of macromolecules and their interactions," *Journal of Pharmacy and Bioallied Sciences,* pp. 39-59, 2011.

[43] Wagner, M., Thermal Analysis in Practice, Cincinnati: Hanser Publications, 2018.

[44] USP, *Disintegration,* The United States Pharmacopeia, May 1, 2020.

[45] Rincon, Y. and Reeves, S., "Design of 3D Printed Molds for Tablet Formation," *American Society for Engineering Education,* 2022.

[46] Florence, A. and et al., "Solving molecular crystal structures from laboratory x-ray powder diffraction data with DASH: the state of the art and challenges," *Journal of Applied Crystallography,* vol. 38, 2005.

[47] Saravanan, L. and Subramanian, S., "Surface chemical studies on the competitive adsorption of poly(ethylene glycol) and ammonium poly(methacrylate) onto alumina," *Journal of Colloid and Interface Science,* vol. 284, pp. 363-377, 2005.

[48] Nandiyanto, A., Oktiani, R. and Ragadhita, R., "How to Read and Interpret FTIR Spectrscope of Organic Material," *Indonesian Journal of Science and Technology,* vol. 4, no. 1, pp. 97-118, 2019.

[49] Sangnim, T. and et al., "Design and characterization of clindamycin-loaded nanofiber patches composed of polyvinyl alcohol and tamarind seed gum and fabricated by electrohydrodynamic atomization," *Asian Journal of Pharmaceutical Sciences,* vol. 13, pp. 450-458, 2018.

[50] Dey, R., Tiwary, G., Patnaik, T. and Jha, U., "Controlled release of 5-aminosalicylic acid from a new pH-responsive polymer derived from tamarind seed polysaccharide, acrylic acid, and polyamindoamine," *Polymer Bulletin,* vol. 66, pp. 583-598, 2011.

[51] Mudgil, D., Barak, S. and Khatkar, B., "X-ray diffraction, IR Spectroscopy and Thermal Characterization of Partially Hydrolyzed Guar Gum," *International of Biological Macromolecules,* vol. 50, pp. 1035-1039, 2012.

[52] Motta, M. and et al., "Study of the Mechanical Degradation Mechanism of Guar Gum in Turbulent Flow by FTIR," *International Lournal of Biological Macromolecules,* vol. 121, pp. 23-28, 2019.

[53] Pawlicka, A. and et al., "Dielectric Behavior and FTIR Studies of Xanthan Gum-Based Solid Polymer Electrolytes," *Electrochimica Acta,* vol. 305, pp. 232-239, 2019.

[54] Sutar, P., Mishra, R., Pal, K. and Banthia, A., "Development of pH Sensitive Polyacrylamide Grafted Pectin Hydrogel for Controlled Drug Delivery System.," *Journal of Materials Science: Materials in Medicine,* vol. 19, pp. 2247-2253, 2008.

[55] T. T, Handbook of Colloid and Interface Science, Volume 1: Basic Principles of Interface Science and Colloid Stability, Walter de Gruyter GmbH, 2018.

[56] P. M. G. G. J. Niebergall, "Dissolution Rate Studies II: Dissolution Particles Under Conditions of Rapid Agitation," *Journal of Pharmaceutical Sciences,* pp. Vol. 52, pp 236-241, March 1963.

[57] H. e. a. Charles-Williams, "Granule Nucleation and Growth: Competing drop spreading and infiltration processes," *Powder Technology,* pp. vol 206, pp 63-71, 2011.

[58] L. L. C. Nair, "Biodegradable Polymers as Biomaterials," *Progress in Polymer Science,* pp. vol 32, pp 762-798, June 11, 2007.

[59] A. C. Society, "CAS Registry Number: 103-9-2," SciFinder, [Online]. Available: https://scifinder-n-cas-org.pvamu.idm.oclc.org/searchDetail/substance/62f3143a55641a06b2f1ed5/substanceDetails. [Accessed 8 August 2022].

[60] T. e. a. Patterson, "Deprescribing Paracetamol in Pain Conditions: A Scoping Review," *Research in Social and Administrative Pharmacy,* vol. 18, pp. 3272-3283, 2022.

[61] J. D. M. Li, "Steady State Morphologies of Paracetamol Crystal from Different Solvents," *Crystal Growth and Design,* vol. 17, pp. 659-670, 2016.

[62] A. e. a. Bertolini, "Paracetamol: New Vistas of an Old Drug," *CNS Drug Reviews,* vol. 12, pp. 250-275, 2006.

[63] Kibbe, A., "Povidone," in *Handbook of Pharmaceutical Excipients; Sixth Edition,* Washington, DC, Pharmaceutical Press, 2009, pp. 581-585.

[64] Nsengiyumva, E. and Alexandridis, P., "Xanthan gum in aqueous solutions: Fundamentals and applications," *International Journal of Biological Macromolecules,* vol. 216, pp. 583-604, 2022.

APPENDIX

Appendix A: Image Analysis Samples

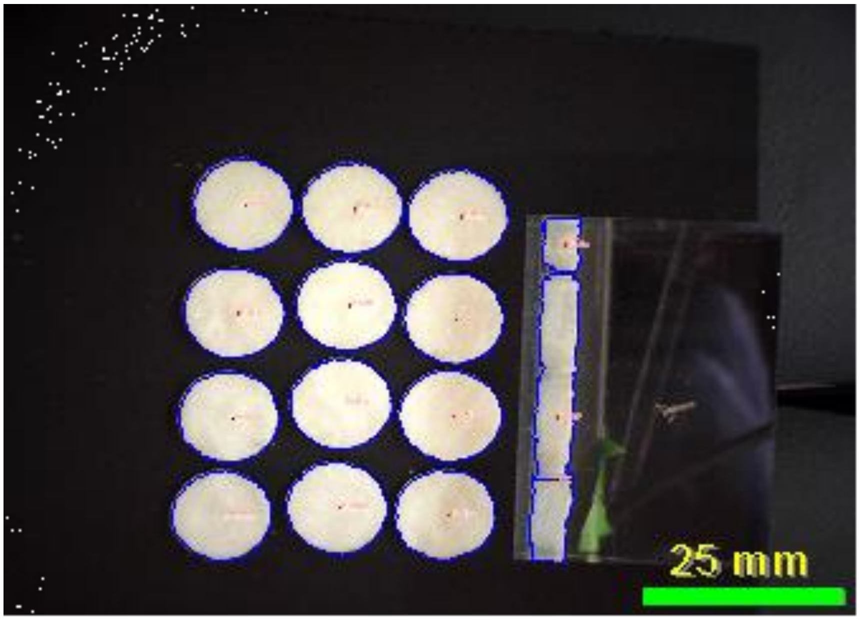

Figure A.1: Image of PEG 3.0wt% Produced from 3D Mold

Table A.1: PEG 3.0wt% 3D Mold Sizing Data

Feature Name	Area(mm^2)	Aspect Ratio	Perimeter (mm)	Roundness	Diameter, Mean(mm)	Height (mm)
P1R1	123.8	1.0	40.4	1.1	12.5	
P1R2	123.4	1.0	40.5	1.1	12.5	
P1R3	123.2	1.0	40.2	1.1	12.4	
P1R5	124.0	1.0	40.6	1.1	12.5	
P1R6	123.0	1.0	40.1	1.1	12.4	
P1R8	122.7	1.0	40.0	1.1	12.4	
P1R9	124.6	1.0	40.4	1.1	12.5	
P1R10	126.1	1.0	40.7	1.1	12.6	
P1R11	123.5	1.0	40.4	1.1	12.5	
P1R12	124.5	1.0	40.6	1.1	12.5	
P1R13	119.9	1.0	39.8	1.1	12.3	
P1R14	123.2	1.0	40.1	1.1	12.4	
Average	123.5	1.0	40.3	1.1	12.5	5.1

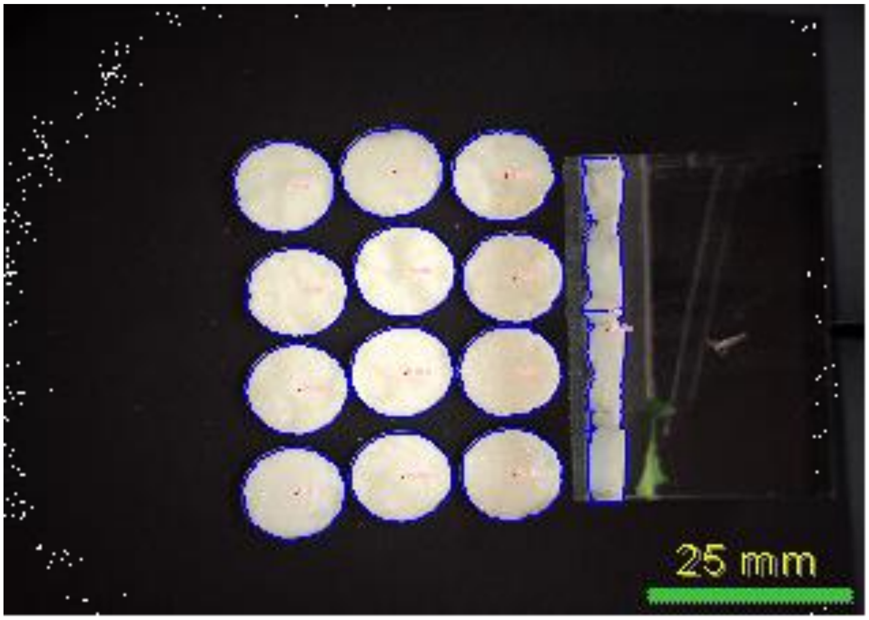

Figure A.2: Image of PEG 6.0wt% Produced from 3D Mold

Table A.2: PEG 6.0wt% 3D Mold Sizing Data

Feature Name	Area(mm^2)	Aspect Ratio	Perimeter (mm)	Roundness	Diameter, Mean(mm)	Height (mm)
P1R1	125.1	1.0	40.6	1.1	12.5	
P1R2	126.0	1.0	40.8	1.1	12.6	
P1R3	125.8	1.0	40.7	1.1	12.6	
P1R5	126.9	1.0	40.9	1.1	12.6	
P1R6	125.0	1.0	40.8	1.1	12.5	
P1R7	123.3	1.0	40.3	1.1	12.4	
P1R8	127.1	1.0	40.7	1.0	12.6	
P1R9	125.9	1.0	41.4	1.1	12.6	
P1R10	125.3	1.0	40.5	1.1	12.6	
P1R11	127.1	1.0	40.6	1.0	12.6	
P1R12	123.7	1.0	39.9	1.0	12.5	
P1R13	127.9	1.0	40.6	1.0	12.7	
Average	125.7	1.0	40.7	1.1	12.6	5.0

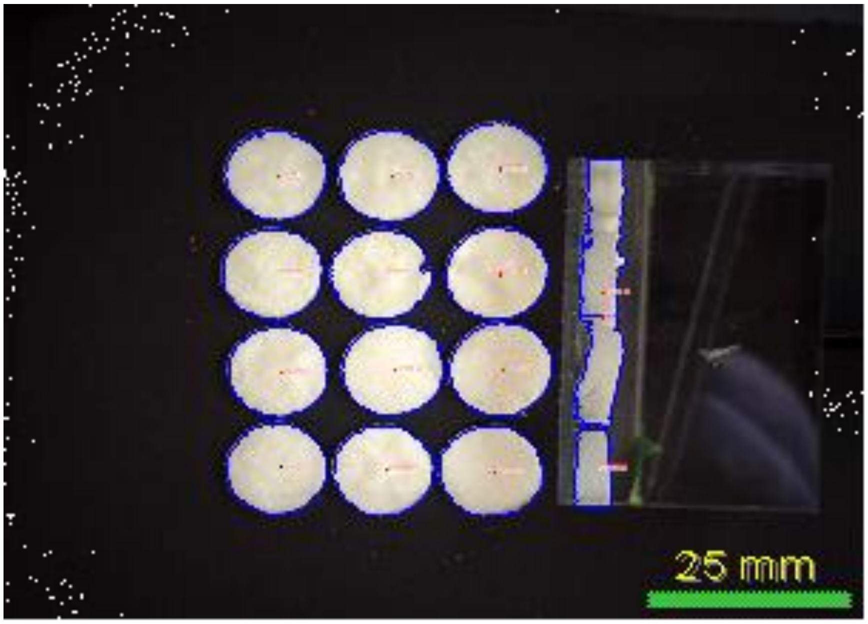

Figure A.3: Image of PEG 9.0wt% Produced from 3D Mold

Table A.3: PEG 9.0wt% 3D Mold Sizing Data

Feature Name	Area(mm^2)	Aspect Ratio	Perimeter (mm)	Roundness	Diameter, Mean(mm)	Height (mm)
P1R1	123.3	1.0	41.4	1.1	12.5	
P1R2	125.0	1.0	40.8	1.1	12.5	
P1R3	120.5	1.0	40.2	1.1	12.3	
P1R5	126.5	1.0	40.8	1.1	12.6	
P1R6	122.9	1.0	40.4	1.1	12.4	
P1R7	120.3	1.0	41.6	1.2	12.3	
P1R8	128.6	1.0	41.0	1.1	12.7	
P1R9	126.4	1.0	41.3	1.1	12.6	
P1R10	120.8	1.0	39.8	1.1	12.3	
P1R11	122.4	1.0	40.3	1.1	12.4	
P1R12	121.7	1.0	41.5	1.1	12.4	
P1R13	126.6	1.0	41.4	1.1	12.6	
Average	123.8	1.0	40.9	1.1	12.5	4.6

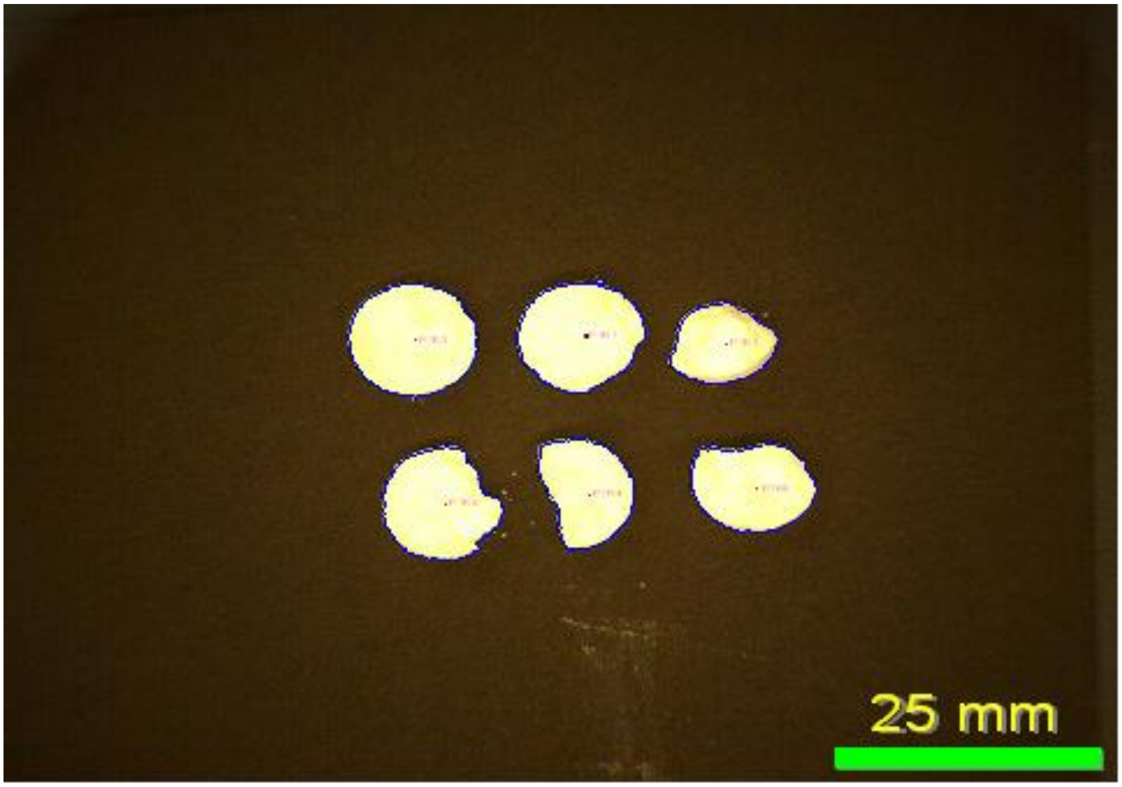

Figure A.4: Image of DS 0.05wt% Produced From 3D Mold

Table A.4: DS 0.05wt% 3D Mold Sizing Data

Feature Name	Area(mm^2)	Aspect Ratio	Perimeter (mm)	Roundness	Diameter, Mean(mm)
P1R1	107.6	1.1	40.3	1.2	11.6
P1R2	114.8	1.0	38.6	1.0	12.0
P1R3	65.1	1.2	30.4	1.2	9.0
P1R4	78.9	1.5	34.7	1.2	9.8
P1R5	88.1	1.3	35.6	1.2	10.5
P1R6	100.1	1.2	39.6	1.3	11.2
average	92.4	1.2	36.5	1.2	10.7

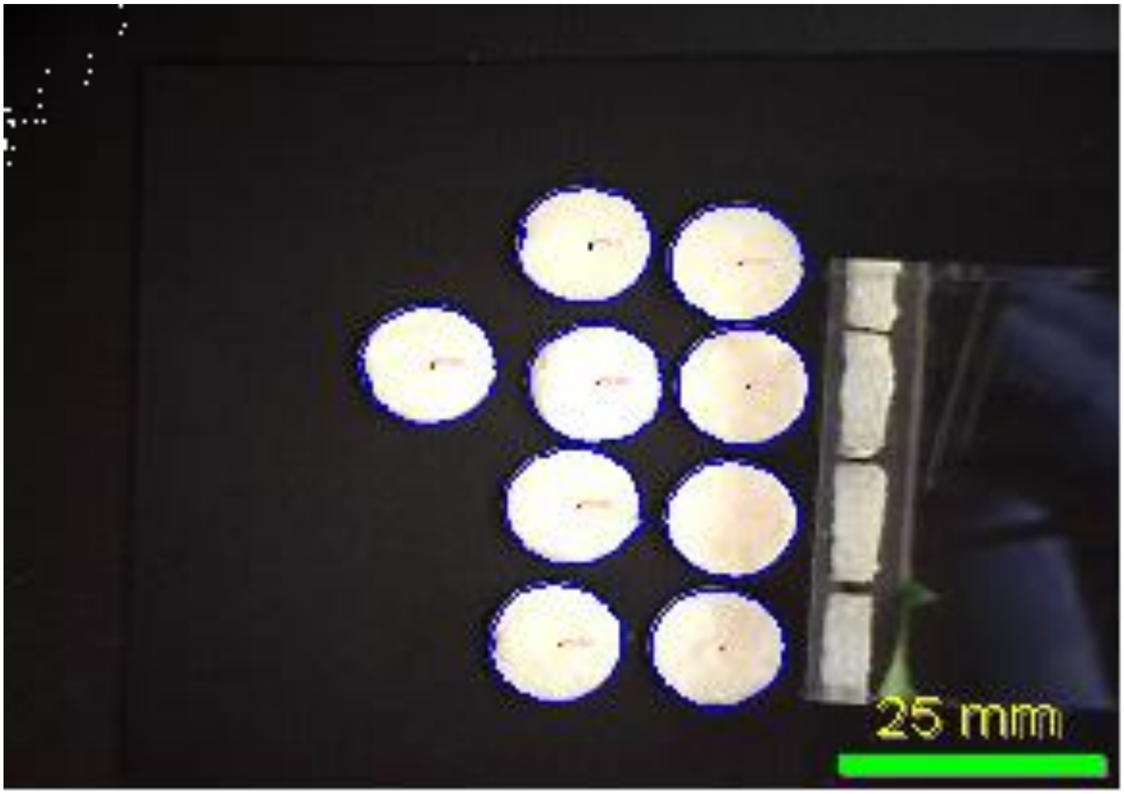

Figure A.5: Image of DS 4.3wt% Produced from 3D Mold

Table A.5: DS 4.3wt% 3D Mold Sizing Data

Feature Name	Area (mm^2)	Aspect Ratio	Perimeter (mm)	Roundness	Diameter, Mean (mm)	Height (mm)
P1R1	126.7	1.0	41.2	1.1	12.6	
P1R2	128.5	1.0	40.8	1.0	12.7	
P1R3	129.4	1.0	41.0	1.0	12.8	
P1R4	131.8	1.0	42.0	1.1	12.9	
P1R5	126.6	1.0	40.3	1.0	12.6	
P1R6	129.2	1.0	41.9	1.1	12.7	
P1R7	124.3	1.0	40.0	1.0	12.5	
P1R8	127.4	1.0	40.5	1.0	12.7	
P1R9	128.8	1.0	41.0	1.1	12.7	
Average	128.1	1.0	41.0	1.1	12.7	5.1

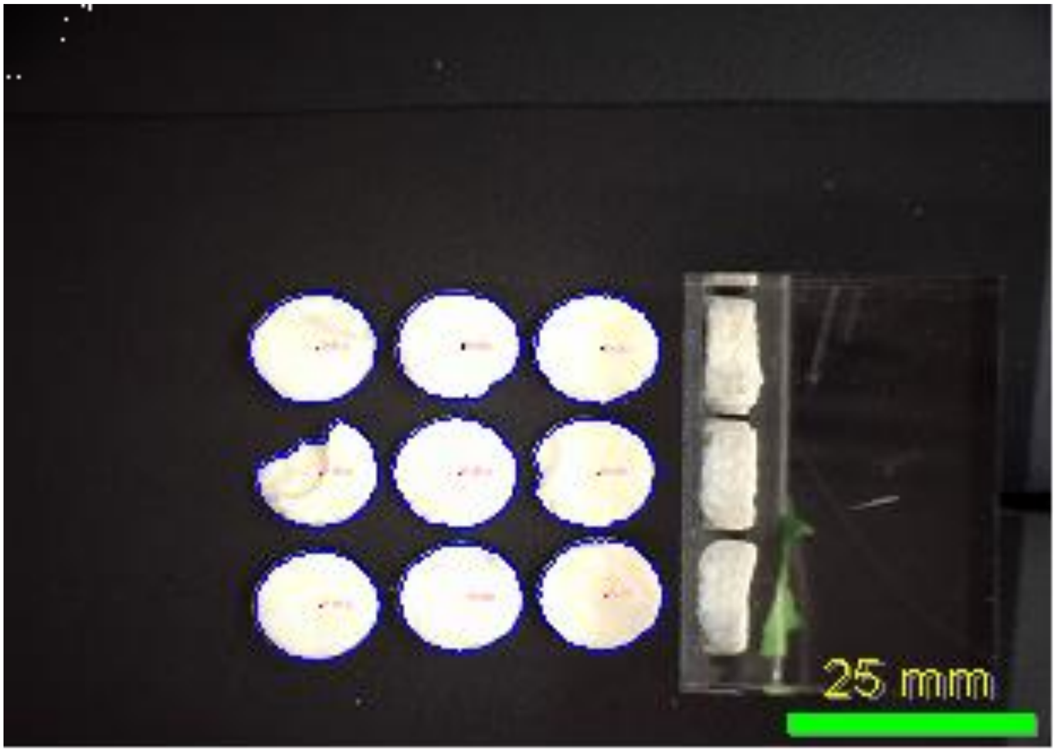

Figure A.6 Image of DS 8.7wt% Produced from 3D Mold

Table A.6: DS 8.7wt% 3D Mold Sizing Data

Feature Name	Area (mm^2)	Aspect Ratio	Perimeter (mm)	Roundness	Diameter, Mean (mm)	Height (mm)
P1R1	121.7	1.0	40.0	1.1	12.4	
P1R2	126.0	1.0	40.5	1.0	12.6	
P1R3	124.1	1.0	40.2	1.1	12.5	
P1R4	124.5	1.0	40.2	1.0	12.5	
P1R5	122.7	1.0	40.8	1.1	12.4	
P1R6	103.5	1.3	40.6	1.3	11.3	
P1R7	125.5	1.0	40.2	1.0	12.6	
P1R8	122.4	1.0	39.8	1.0	12.4	
P1R9	123.2	1.0	39.6	1.0	12.4	
Average	121.5	1.1	40.2	1.1	12.3	5.1

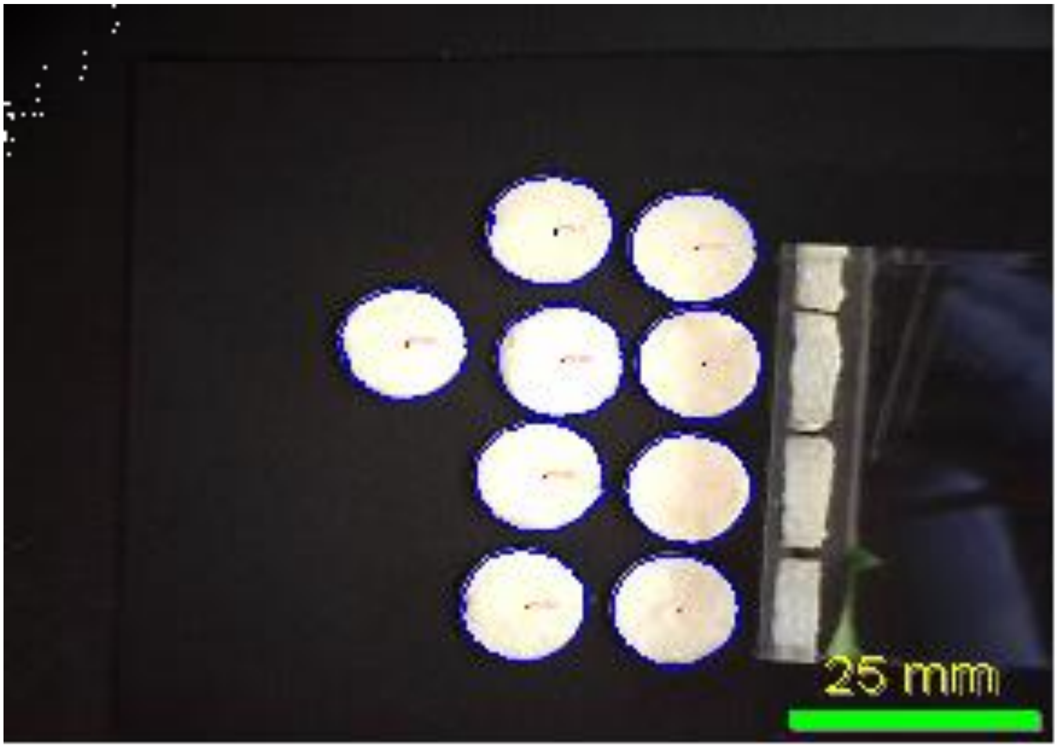

Figure A.7: Image of DS 13.0wt% 3D Mold

Table A.7: DS 13.0wt% 3D Mold Sizing Data

Feature Name	Area (mm^2)	Aspect Ratio	Perimeter (mm)	Roundness	Diameter, Mean (mm)	Height (mm)
P1R1	126.7	1.0	41.2	1.1	12.6	
P1R2	128.5	1.0	40.8	1.0	12.7	
P1R3	129.4	1.0	41.0	1.0	12.8	
P1R4	131.8	1.0	42.0	1.1	12.9	
P1R5	126.6	1.0	40.3	1.0	12.6	
P1R6	129.2	1.0	41.9	1.1	12.7	
P1R7	124.3	1.0	40.0	1.0	12.5	
P1R8	127.4	1.0	40.5	1.0	12.7	
P1R9	128.8	1.0	41.0	1.1	12.7	
Average	128.1	1.0	41.0	1.1	12.7	5.1

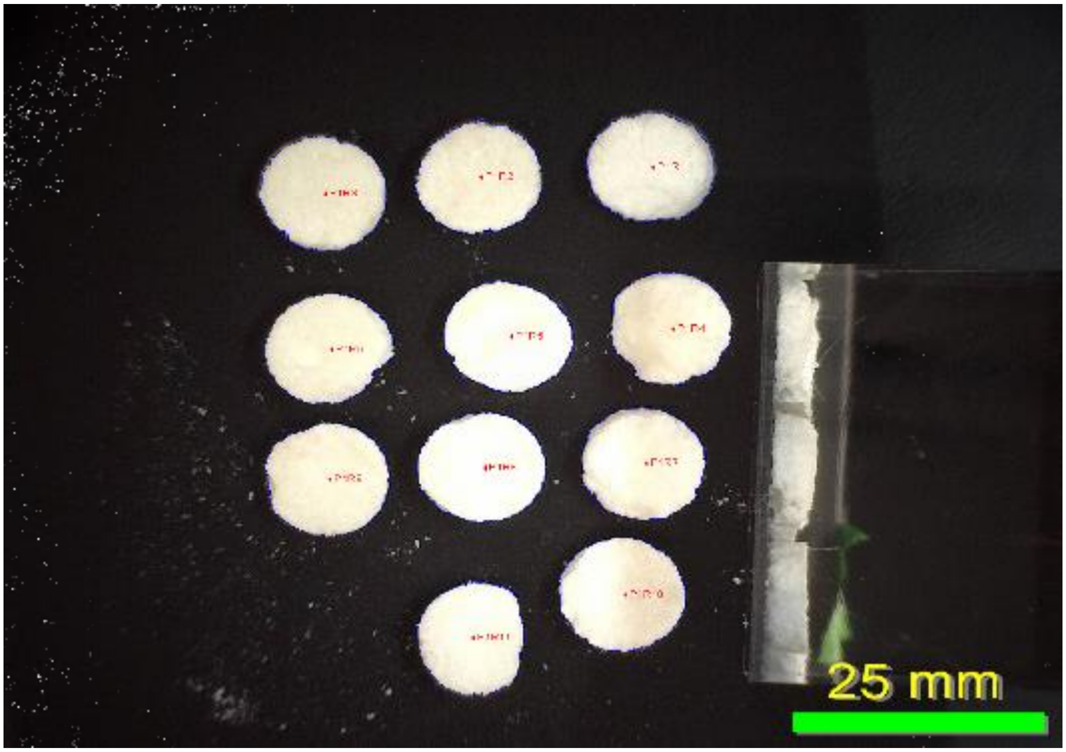

Figure A.8 Image of TM 0.1wt% Produced from a 3D Mold

Table A.8: TM 0.1wt% 3D Mold Sizing Data

Feature Name	Area (mm^2)	Aspect Ratio	Perimeter (mm)	Roundness	Diameter, Mean (mm)	Height (mm)
P1R1	123.8	1.0	40.5	1.1	12.5	
P1R2	122.9	1.0	41.0	1.1	12.4	
P1R3	126.7	1.1	40.8	1.1	12.6	
P1R4	119.7	1.1	40.5	1.1	12.3	
P1R5	123.6	1.1	41.6	1.1	12.5	
P1R6	120.5	1.1	40.4	1.1	12.3	
P1R7	123.3	1.0	40.7	1.1	12.4	
P1R8	123.6	1.0	40.8	1.1	12.5	
P1R9	124.2	1.0	40.8	1.1	12.5	
P1R10	126.7	1.0	41.2	1.1	12.6	
P1R11	109.2	1.2	40.5	1.2	11.7	
Average	122.2	1.1	40.8	1.1	12.4	4.4

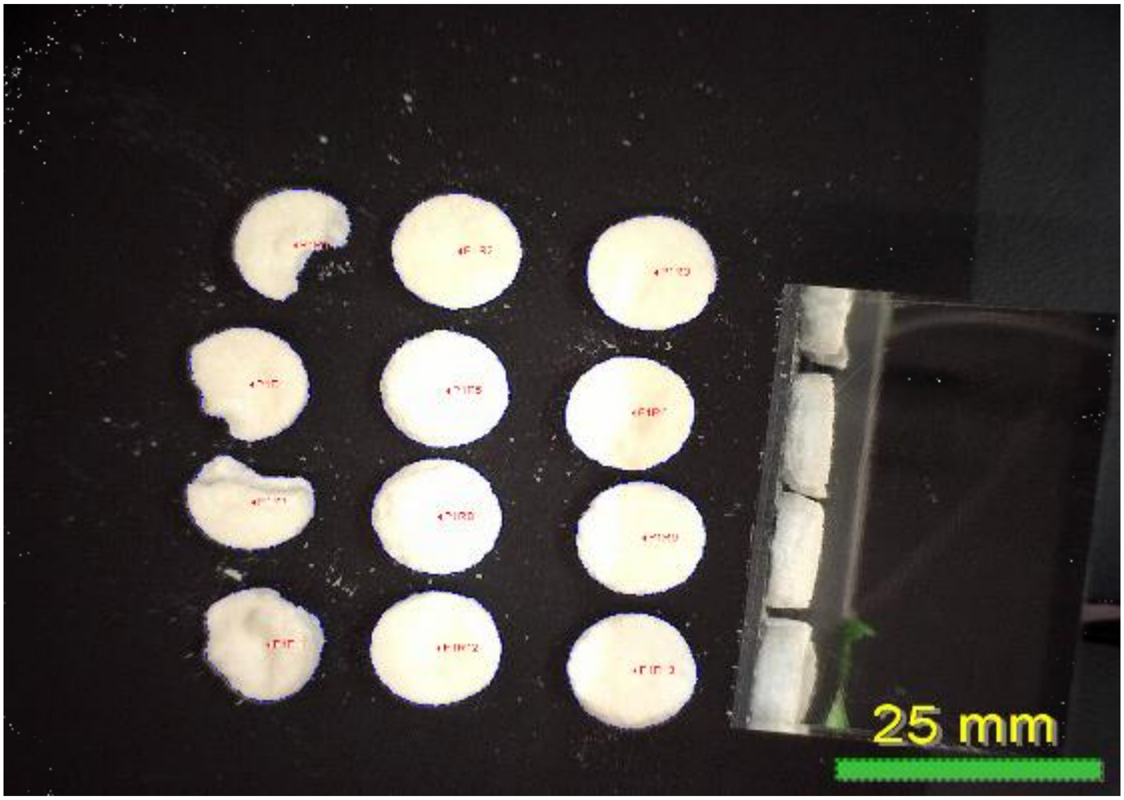

Figure A.9: Image of TM 0.25wt% Produced from a 3D Mold

Table A.9: TM 0.25wt% 3D Mold Sizing Data

Feature Name	Area(mm^2)	Aspect Ratio	Perimeter (mm)	Roundness	Diameter, Mean(mm)	Height (mm)
P1R1	86.7	1.4	38.2	1.4	10.2	
P1R2	119.2	1.0	39.9	1.1	12.2	
P1R3	120.1	1.0	40.1	1.1	12.3	
P1R4	102.8	1.2	38.1	1.1	11.3	
P1R5	119.7	1.0	40.2	1.1	12.3	
P1R6	116.8	1.0	39.0	1.0	12.1	
P1R7	88.4	1.4	36.2	1.2	10.4	
P1R8	119.0	1.0	40.1	1.1	12.2	
P1R9	117.7	1.0	39.2	1.1	12.2	
P1R11	103.6	1.1	38.1	1.1	11.4	
P1R12	120.6	1.0	39.6	1.0	12.3	
P1R13	118.4	1.0	39.0	1.0	12.2	
Average	111.1	1.1	39.0	1.1	11.8	4.7

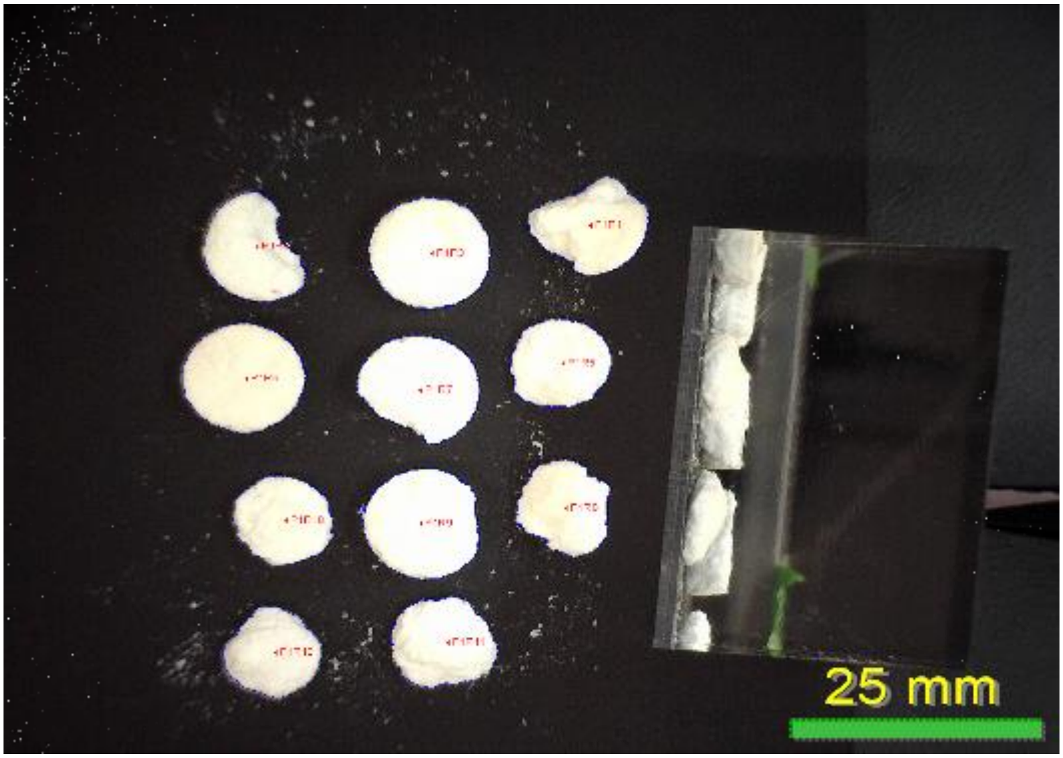

Figure A.10: Image of TM 0.50wt% Produced from a 3D Mold

Table A.10: TM 0.50wt% 3D Mold Sizing Data

Feature Name	Area (mm^2)	Aspect Ratio	Perimeter (mm)	Roundness	Diameter, Mean (mm)	Height (mm)
P1R1	88.2	1.2	36.8	1.2	10.4	
P1R2	87.6	1.4	36.7	1.2	10.3	
P1R3	119.5	1.0	40.3	1.1	12.3	
P1R5	80.0	1.1	33.3	1.1	10.0	
P1R6	116.5	1.0	38.9	1.0	12.1	
P1R7	107.6	1.2	39.5	1.2	11.6	
P1R8	75.6	1.2	34.6	1.3	9.7	
P1R9	114.8	1.1	41.8	1.2	12.0	
P1R10	77.1	1.1	32.9	1.1	9.8	
P1R11	84.1	1.1	34.7	1.2	10.3	
P1R12	72.7	1.0	31.7	1.1	9.5	
Average	93.1	1.1	36.5	1.2	10.7	5.0

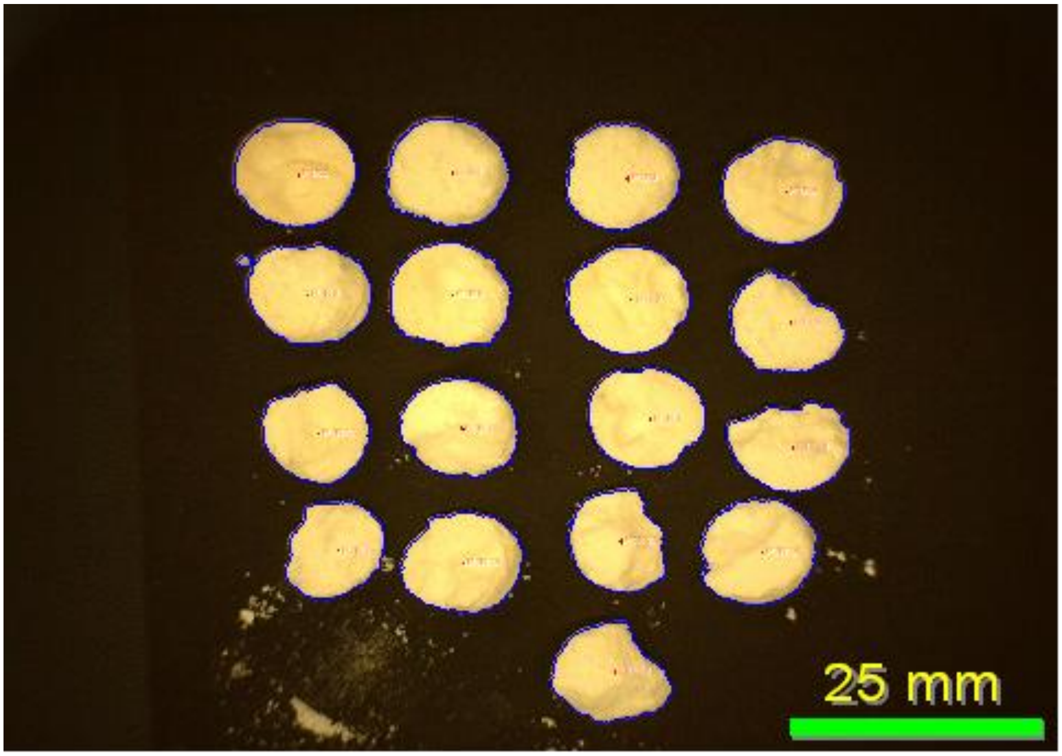

Figure A.11: Image of PC 0.05wt% Produced from a 3D Mold

Table A.11: PC 0.05wt% 3D Sizing Data

Feature Name	Area(mm^2)	Aspect Ratio	Perimeter, Bounding Polygon(mm)	Roundness	Diameter, Mean(mm)
P1R1	115.1	1.0	41.2	1.2	12.0
P1R2	114.4	1.0	38.7	1.1	12.0
P1R3	106.4	1.1	38.8	1.1	11.6
P1R4	110.2	1.0	38.4	1.1	11.8
P1R5	112.5	1.1	42.8	1.3	11.9
P1R6	110.9	1.2	43.3	1.4	11.8
P1R7	113.7	1.0	40.0	1.1	12.0
P1R8	91.5	1.2	38.4	1.3	10.7
P1R9	103.8	1.0	39.1	1.2	11.4
P1R10	101.0	1.1	38.3	1.2	11.3
P1R11	90.7	1.0	35.6	1.1	10.7
P1R12	92.9	1.3	37.4	1.2	10.7
P1R13	85.9	1.3	36.7	1.3	10.3
P1R14	108.1	1.1	40.3	1.2	11.6
P1R15	82.9	1.2	34.5	1.2	10.1
P1R16	105.7	1.1	38.7	1.1	11.5
P1R17	94.3	1.2	37.9	1.2	10.8
Average	102.3	1.1	38.8	1.2	11.3

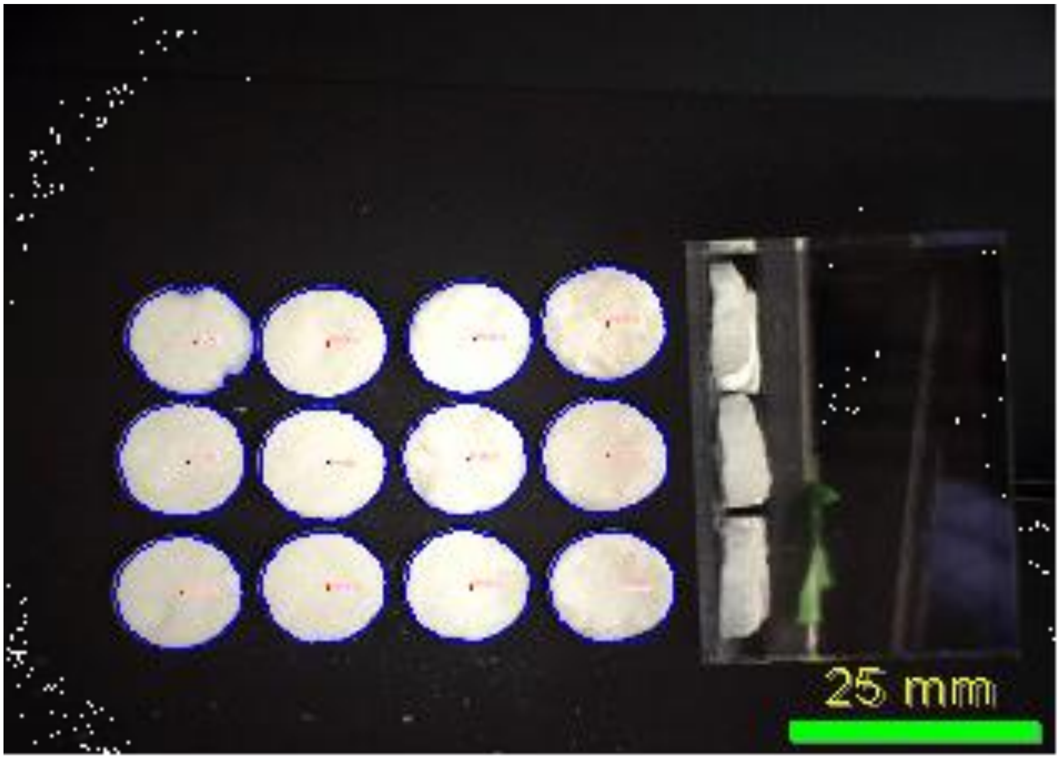

Figure A.12: Image of PC 0.25wt% Produced from a 3D Mold

Table A.12: PC 0.25wt% 3D Mold Sizing Data

Feature Name	Area (mm^2)	Aspect Ratio	Perimeter (mm)	Roundness	Diameter, Mean (mm)	Height (mm)
P1R1	126.1	1.0	40.8	1.1	12.6	
P1R2	125.2	1.0	40.5	1.1	12.6	
P1R3	119.9	1.0	41.1	1.1	12.3	
P1R4	125.5	1.0	40.3	1.0	12.6	
P1R5	128.4	1.0	41.6	1.1	12.7	
P1R6	128.9	1.0	40.8	1.0	12.7	
P1R7	125.8	1.0	40.9	1.1	12.6	
P1R8	127.0	1.0	40.8	1.1	12.6	
P1R9	124.1	1.0	40.0	1.0	12.5	
P1R10	125.7	1.0	40.5	1.1	12.6	
P1R11	124.3	1.0	41.0	1.1	12.5	
P1R12	125.9	1.0	40.4	1.0	12.6	
Average	125.6	1.0	40.7	1.1	12.6	5.0

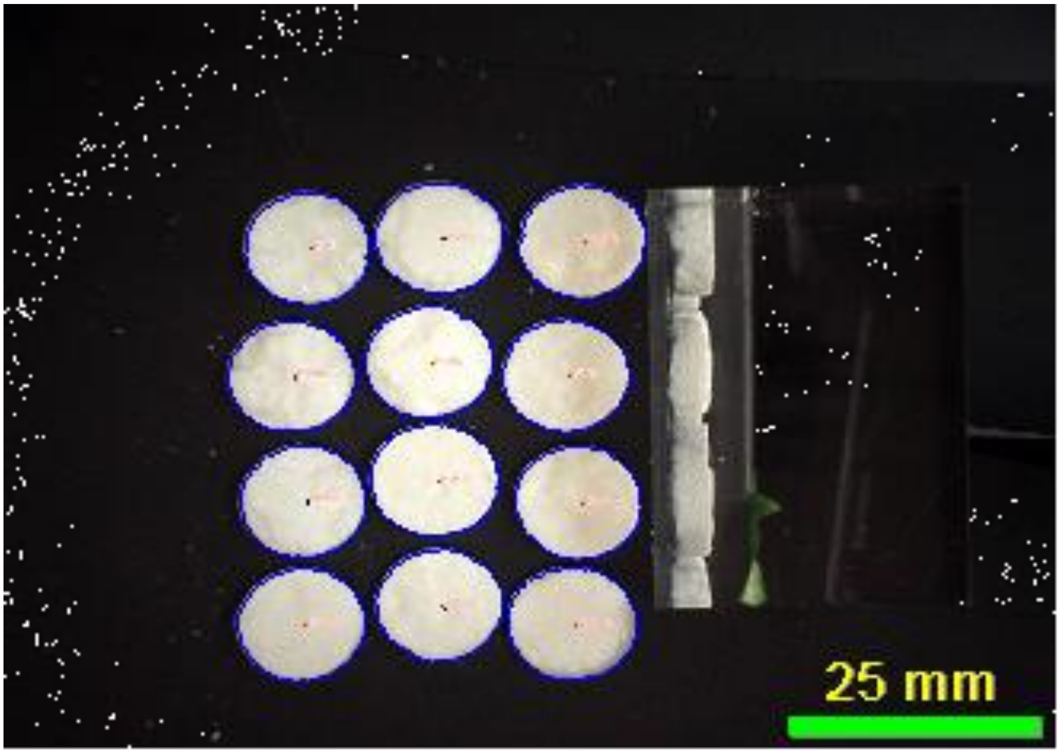

Figure A.13: Image of PC 0.50wt% Produced from a 3D Mold

Table A.13: PC 0.50wt% 3D Sizing Data

Feature Name	Area(mm^2)	Aspect Ratio	Perimeter (mm)	Roundness	Diameter, Mean(mm)	Height (mm)
P1R1	125.9	1.0	40.1	1.0	12.6	
P1R2	125.6	1.0	40.2	1.0	12.6	
P1R3	124.1	1.0	40.2	1.0	12.5	
P1R4	126.6	1.0	40.7	1.1	12.6	
P1R5	126.0	1.0	40.5	1.0	12.6	
P1R6	124.8	1.0	40.2	1.0	12.5	
P1R7	127.9	1.0	40.4	1.0	12.7	
P1R8	124.5	1.0	40.6	1.1	12.5	
P1R9	126.1	1.0	40.2	1.0	12.6	
P1R10	124.4	1.0	40.4	1.1	12.5	
P1R11	126.8	1.0	40.8	1.1	12.6	
P1R12	128.4	1.0	40.9	1.1	12.7	
Average	125.9	1.0	40.4	1.0	12.6	4.3

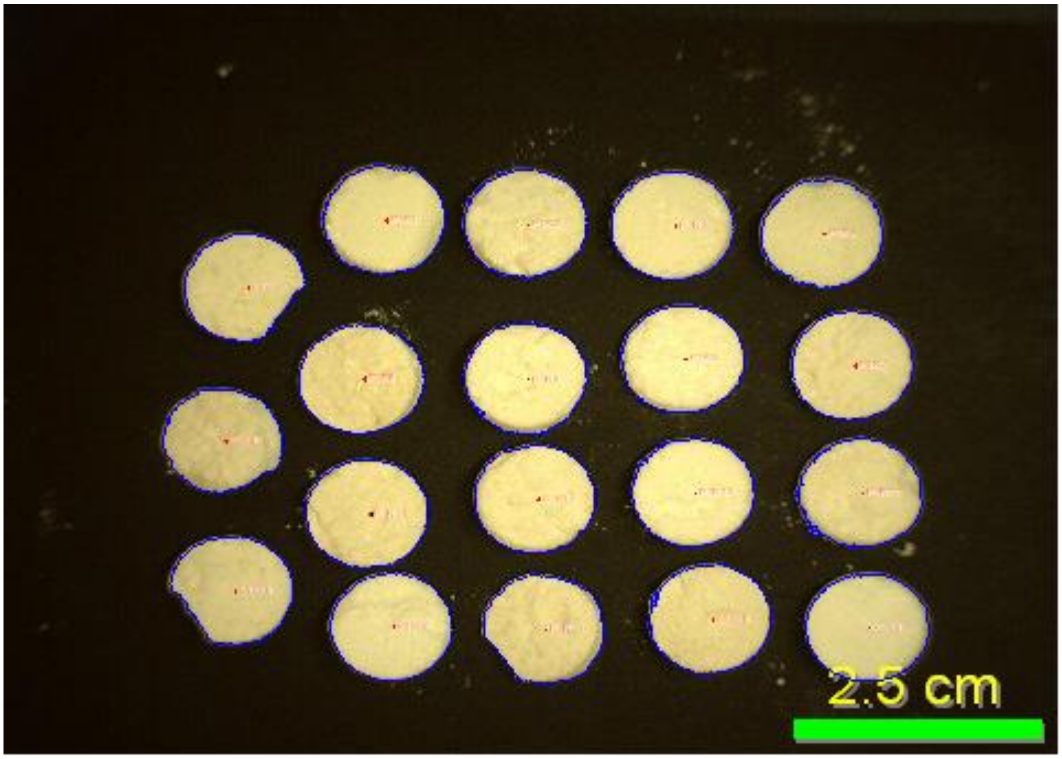

Figure A.14: Image of XN 0.05wt% Produced from 3D Molds

Table A.14: XN 0.05wt% 3D Sizing Data

Feature Name	Area (cm^2)	Aspect Ratio	Perimeter (cm)	Roundness	Height (cm)
P1R1	1.2	1.0	4.0	1.1	
P1R2	1.2	1.0	4.2	1.2	
P1R3	1.2	1.0	4.0	1.1	
P1R4	1.2	1.0	4.0	1.1	
P1R5	1.1	1.1	3.9	1.1	
P1R6	1.2	1.0	3.9	1.0	
P1R7	1.2	1.0	3.9	1.0	
P1R8	1.2	1.0	4.1	1.1	
P1R9	1.2	1.0	4.1	1.1	
P1R10	1.1	1.0	3.9	1.1	
P1R11	1.2	1.0	4.2	1.2	
P1R12	1.2	1.0	4.0	1.1	
P1R13	1.2	1.0	4.0	1.1	
P1R14	1.2	1.0	4.0	1.1	
P1R15	1.1	1.1	3.9	1.1	
P1R16	1.2	1.0	4.0	1.1	
P1R17	1.2	1.0	3.9	1.1	
P1R18	1.2	1.0	4.0	1.1	
P1R19	1.2	1.1	3.9	1.1	
Average	1.2	1.0	4.0	1.1	0.4

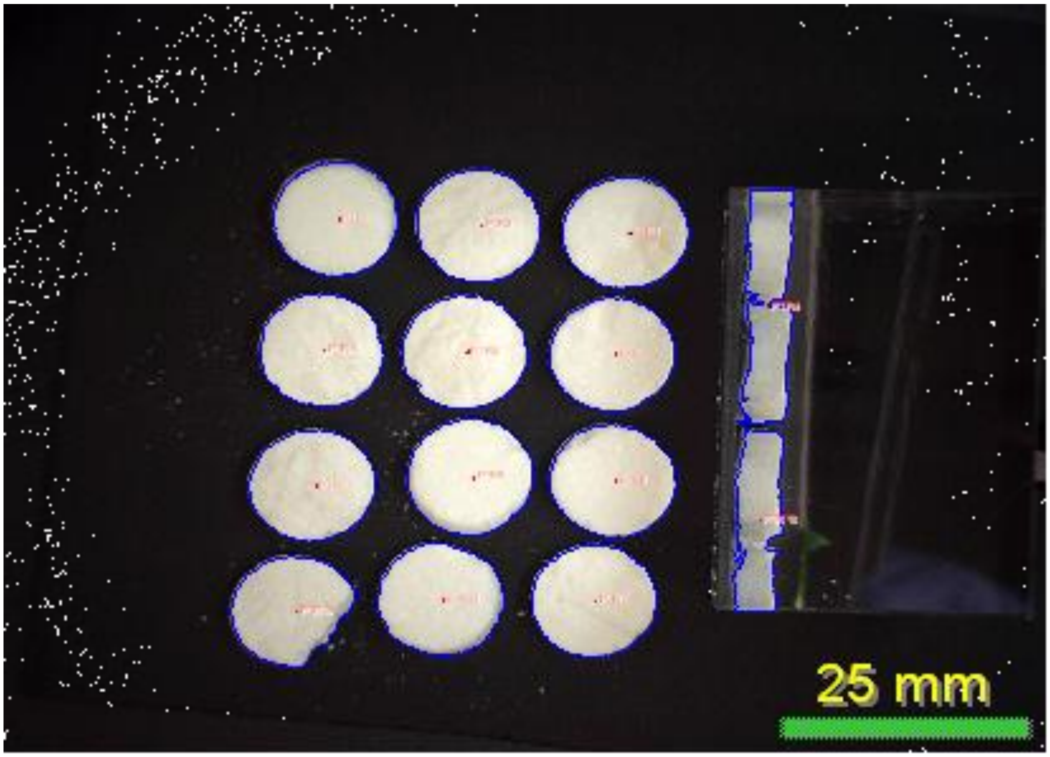

Figure A.15: Image of XN 0.25wt% Produced from a 3D Mold

Table A.15: XN 0.25wt% 3D Sizing Data

Feature Name	Area(mm^2)	Aspect Ratio	Perimeter (mm)	Roundness	Diameter, Mean(mm)	Height (mm)
P1R1	126.7	1.0	40.6	1.1	12.6	
P1R2	124.9	1.0	40.5	1.1	12.5	
P1R3	124.9	1.0	40.1	1.0	12.5	
P1R5	125.6	1.0	40.9	1.1	12.6	
P1R6	126.1	1.0	40.7	1.1	12.6	
P1R7	126.0	1.0	40.2	1.0	12.6	
P1R8	129.4	1.0	41.1	1.1	12.8	
P1R9	125.4	1.0	40.3	1.0	12.6	
P1R11	124.3	1.0	40.0	1.0	12.5	
P1R12	125.2	1.0	41.1	1.1	12.5	
P1R13	124.9	1.0	40.4	1.1	12.5	
P1R14	113.0	1.2	40.1	1.1	11.9	
Average	124.7	1.0	40.5	1.1	12.5	4.8

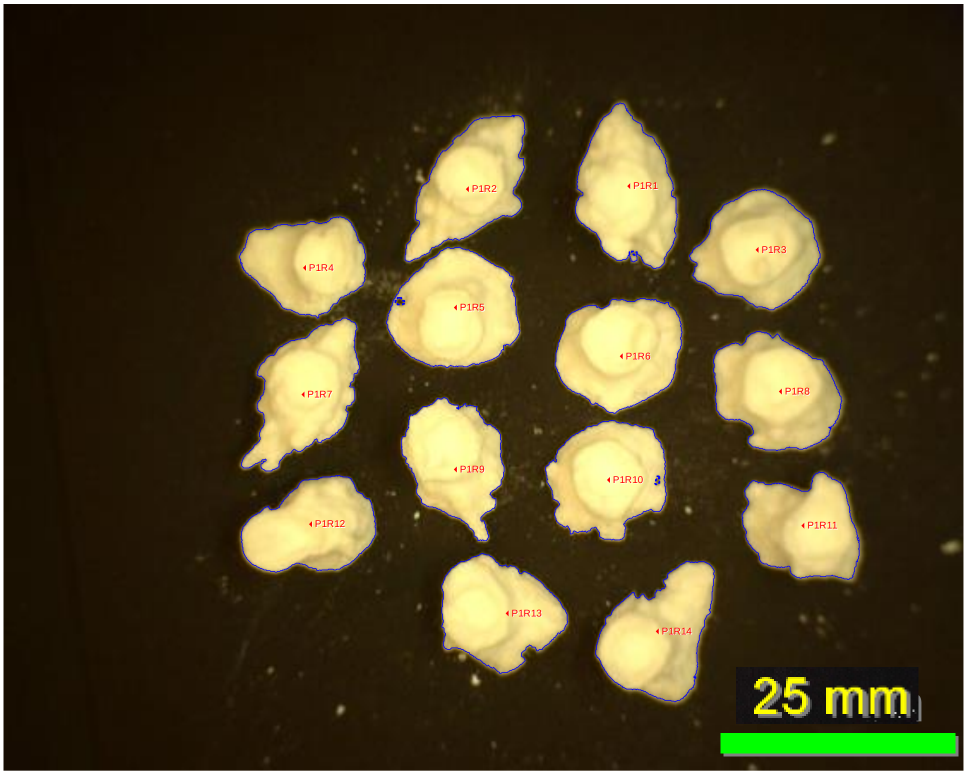

Figure A.16: Image of DS 8.7wt% Produced from Trays

Table A.16: DS 8.7wt% Tray Sizing Data

Feature Name	Area (mm^2)	Axis, Major (mm)	Axis, Minor (mm)	Aspect Ratio	Perimeter (mm)	Roundness
P1R1	131.3	16.6	10.2	1.6	4.9	1.5
P1R2	117.7	17.2	8.9	1.9	4.9	1.6
P1R3	122.7	13.0	12.1	1.1	4.3	1.2
P1R4	102.3	13.2	10.0	1.3	4.0	1.2
P1R5	135.2	13.9	12.4	1.1	4.4	1.1
P1R6	126.6	13.9	11.6	1.2	4.3	1.2
P1R7	121.9	17.0	9.4	1.8	5.3	1.9
P1R8	126.7	14.6	11.1	1.3	4.5	1.3
P1R9	109.0	14.1	10.0	1.4	4.6	1.6
P1R10	122.2	13.4	11.7	1.1	4.6	1.4
P1R11	107.7	13.4	10.5	1.3	4.3	1.4
P1R12	107.8	14.8	9.4	1.6	4.1	1.2
P1R13	116.7	13.4	11.2	1.2	4.4	1.3
P1R14	122.9	15.5	10.6	1.5	4.7	1.4
Average	119.3	14.6	10.6	1.4	4.5	1.4

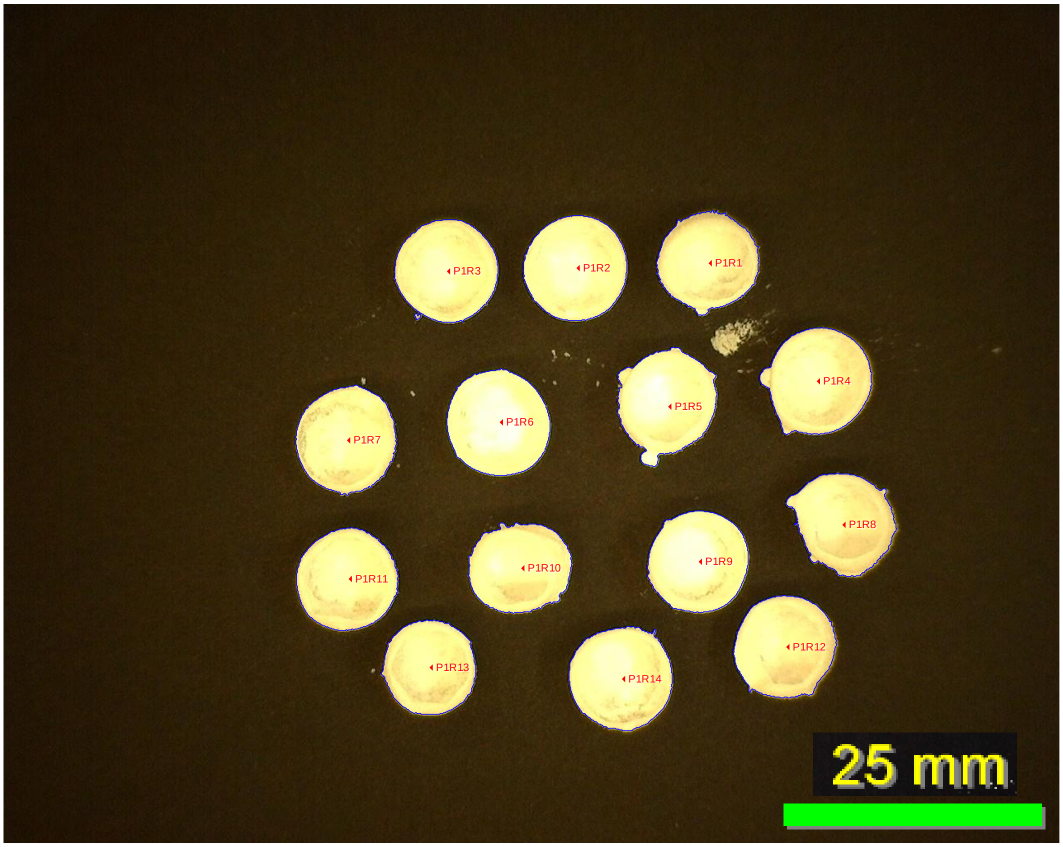

Figure A.17: Image of XN 0.5wt% Produced from Trays

Table A.17: XN 0.5wt% Sizing Data

Feature Name	Area (mm^2)	Axis, Major (mm)	Axis, Minor (mm)	Aspect Ratio	Perimeter (mm)	Roundness
P1R1	73.8	9.9	9.5	1.0	32.6	1.2
P1R2	81.5	10.4	10.0	1.0	32.1	1.0
P1R3	78.7	10.0	10.0	1.0	33.9	1.2
P1R4	84.6	10.7	10.1	1.1	34.3	1.1
P1R5	79.1	10.7	9.5	1.1	36.1	1.3
P1R6	82.3	10.6	9.9	1.1	32.5	1.0
P1R7	79.9	10.5	9.7	1.1	32.6	1.1
P1R8	75.9	10.5	9.2	1.1	34.4	1.3
P1R9	77.1	10.1	9.7	1.0	31.5	1.0
P1R10	70.7	10.2	8.8	1.2	32.1	1.2
P1R11	77.3	10.1	9.8	1.0	31.6	1.0
P1R12	78.3	10.3	9.7	1.1	32.6	1.1
P1R13	66.4	9.3	9.0	1.0	29.4	1.1
P1R14	80.4	10.2	10.1	1.0	33.3	1.1
Average	77.6	10.2	9.6	1.1	32.8	1.1

Figure 18: TM 0.05wt% Produced from Trays

Table 18: TM 0.05wt% Sizing Data

Feature Name	Area (mm^2)	Axis, Major (mm)	Axis, Minor (mm)	Aspect Ratio	Perimeter (mm)	Roundness
P1R1	102.3	12.7	10.3	1.2	41.6	1.4
P1R2	126.2	13.7	12.0	1.1	54.9	1.9
P1R3	81.1	10.6	9.8	1.1	35.6	1.3
P1R4	103.2	14.0	9.5	1.5	42.8	1.4
P1R5	91.0	11.1	10.5	1.1	37.5	1.3
P1R6	115.2	13.5	11.0	1.2	44.9	1.4
P1R7	88.1	11.6	9.8	1.2	38.9	1.4
P1R8	79.0	11.5	9.2	1.3	40.2	1.7
P1R9	100.2	13.7	9.5	1.4	45.1	1.6
P1R10	138.8	17.5	10.2	1.7	51.6	1.5
P1R11	105.2	13.7	9.8	1.4	41.8	1.3
P1R12	111.4	14.5	9.9	1.5	44.9	1.5
P1R13	131.3	15.8	11.3	1.4	54.1	1.8
Average	105.6	13.4	10.2	1.3	44.2	1.5

Appendix B: Image Analysis Averages

Table B.1: 3D Mold Method Sizing Data

	3D Mold				
	Tablet	Area(mm^2)	Perimeter (mm)	Roundness	Aspect Ratio
Synthetic	PEG 3wt%	123.7 ± 1.7	40.4 ± 0.5	1.1	1.0
	PEG 6wt%	125.5 ± 1.2	40.6 ± 0.4	1.1	1.0
	PEG 9wt%	124.4 ± 2.4	41.0 ± 0.8	1.1	1.0
Sugar	DS0.05wt%	92.4 ± 18.6	36.5 ± 3.7	1.2	1.2
	DS 4.33wt%	125.9 ± 2.8	40.7 ± 0.7	1.1	1.0
	DS 8.67wt%	115.2 ± 5.0	38.6 ± 0.9	1.0	1.0
	DS 13wt%	122.7 ± 3.6	40.2 ± 0.7	1.1	1.0
Polysaccharide	PC 0.05wt%	102.3 ± 10.3	38.8 ± 2.2	1.2	1.1
	PC 0.1wt%	97.6 ± 19.5	38.3 ± 2.8	1.2	1.2
	PC 0.25wt%	125.6 ± 2.2	40.7 ± 0.4	1.1	1.0
	PC 0.5wt%	125.9 ± 1.3	40.4 ± 0.3	1.0	1.0
	TM 0.1wt%	122.2 ± 4.6	40.8 ± 0.4	1.1	1.1
	TM 0.25wt%	111.1 ± 12.1	39.0 ± 1.1	1.1	1.1
	TM 0.5wt%	93.1 ± 17.1	36.5 ± 3.2	1.2	1.1
	XN 0.05wt%	107.6 ± 12.5	38.8 ± 1.6	1.1	1.1
	XN 0.25wt%	125.0 ± 2.9	40.5 ± 0.4	1.1	1.0
	GG 0.12wt%	112.0 ± 10.7	40.6 ± 2.9	1.2	1.1
	GG 0.25wt%	119.9 ± 6.7	40.9 ± 1.2	1.1	1.1
	GG 0.36wt%	110.5 ± 19.7	40.0 ± 3.4	1.2	1.1

Table B.2: Tray Method Sizing Data

Tablet	Area(mm^2)	Perimeter (mm)	Roundness	Aspect Ratio
DS 8.67wt%	117.9 ± 10.2	43.3 ± 3.6	1.3	1.3
XN0.5wt%	95.5 ± 14.9	37.7 ± 4.7	1.2	1.2
TM0.05wt%	105.6 ± 17.9	4.4 ± 5.9	1.5	1.3

Appendix C: Disintegration Results

Table C.1: PEG5 Disintegration Results

Excipient: PEG5		
Sample #	wt (g)	Time (s)
1	0.322	14
2	0.331	178
3	0.318	189
4	0.325	19
5	0.323	25
6	0.324	67
Average	0.324	82

Table C.2 PEG10 Disintegration Results

Excipient: PEG10		
Sample #	wt (g)	Time (s)
1	0.321	91
2	0.34	11
3	0.338	10
4	0.321	7
5	0.336	6
6	0.338	6
Average	0.332	21.8

Table C.3 PEG15 Disintegration Results

Excipient: PEG15		
Sample #	wt (g)	Time (s)
1	0.349	24
2	0.347	22
3	0.353	20
4	0.351	32
5	0.342	29
6	0.353	43
Average	0.349	28.3

Table C.4: DS25 Disintegration Results

Excipient: DS25		
Sample #	wt (g)	Time (s)
1	0.317	15
2	0.315	4
3	0.326	4
4	0.324	4
5	0.328	4
6	0.325	4
Average	0.323	5.8

Table C.5 DS50 Disintegration Results

Excipient: DS50		
Sample #	wt (g)	Time (s)
1	0.305	2
2	0.343	2
3	0.32	2
4	0.304	2
5	0.319	2
6	0.312	2
Average	0.3172	2

Table C.6: DS75 Disintegration Results

Excipient: DS75		
Sample #	wt (g)	Time (s)
1	0.31	5
2	0.35	5
3	0.331	5
4	0.332	5
5	0.32	15
6	0.349	15
Average	0.332	8.3

Table C.7: TM 0.1wt% Disintegration Results

Excipient: TM 0.1wt%		
Sample #	wt (g)	Time (s)
1	0.203	29
2	0.262	54
3	0.237	60
4	0.262	60
5	0.262	30
6	0.256	40
Average	0.247	45.5

Table C.8: TM 0.25wt% Disintegration Results

Excipient: TM 0.25%		
Sample #	wt (g)	Time (s)
1	0.249	66
2	0.271	90
3	0.264	15
4	0.263	29
5	0.247	61
6	0.26	54
Average	0.259	52.5

Table C.9: TM0.5wt% Disintegration Results

Excipient: TM 0.5%		
Sample #	wt (g)	Time (s)
1	0.254	102
2	0.292	175
3	0.259	113
4	0.274	170
5	0.245	67
6	0.27	98
Average	0.266	120.8

Table C.10: PC 0.5wt% Disintegration Results

Excipient: PC 0.5wt%		
Sample #	wt (g)	Time (s)
1	0.211	71
2	0.231	95
3	0.226	75
4	0.258	105
5	0.21	46
6	0.225	57
Average	0.227	74.8

Table C.11: XN 0.25wt% Disintegration Results

	Excipient: XN0.25wt%		
	Sample #	wt (g)	Time (s)
Experiment 1	1	0.299	177
	2	0.309	214
	3	0.302	216
	4	0.253	94
	5	0.304	DND
	6	0.305	75
Experiment 2	1	0.312	280
	2	0.32	DND
	3	0.297	225
	4	0.281	DND
	5	0.295	111
	6	0.295	63
Experiment 3	1	0.237	149
	2	0.254	DND
	3	0.264	255
	4	0.231	233
	5	0.224	42
	6	0.239	44
	Average	0.279	187.7

Table C.12: GG15 Disintegration Results

Excipient: GG15		
Sample #	wt (g)	Time (s)
1	0.224	82
2	0.243	88
3	0.229	76
4	0.252	174
5	0.233	105
6	0.221	115
Average	0.234	106.7

Table C.13: DA5 Disintegration Results

Excipient: DA5		
Sample #	wt (g)	Time (s)
1	0.322	4
2	0.322	4
3	0.377	4
4	0.296	4
5	0.291	6
6	0.351	6
Average	0.327	4.7

Appendix D: Dissolution Mathematical Models and Standard Linear Curve

Table D.1: Standard Linear Curve Data Points

APAP Concentration (µg/ml)	Absorbance
400	0.235 ± 0.008
800	0.479 ± 0.008
1200	0.706 ± 0.011
1600	1.009 ± 0.009
2000	1.258 ± 0.010

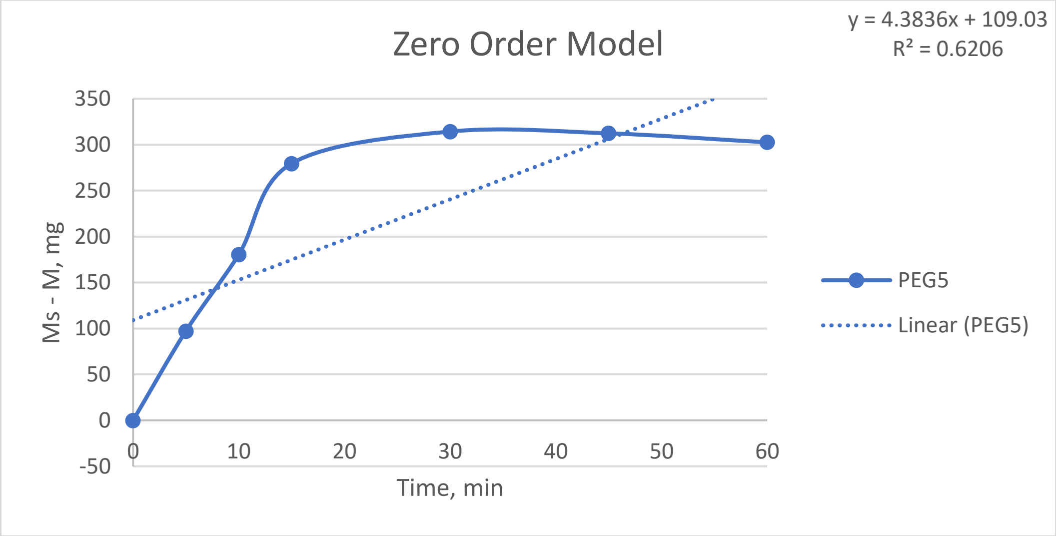

Figure D.1: Zero Order Model PEG5

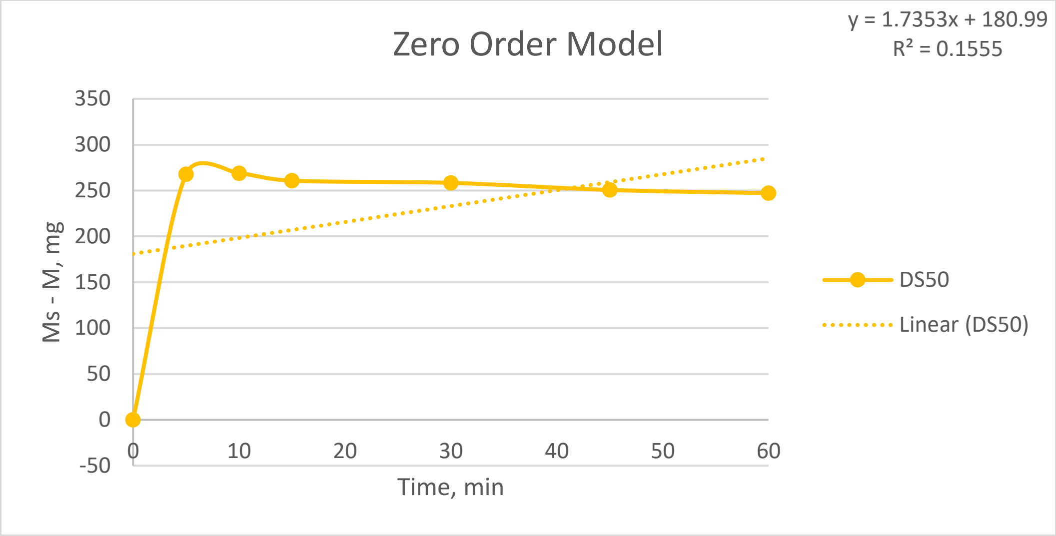

Figure D.2: Zero Order Model DS50

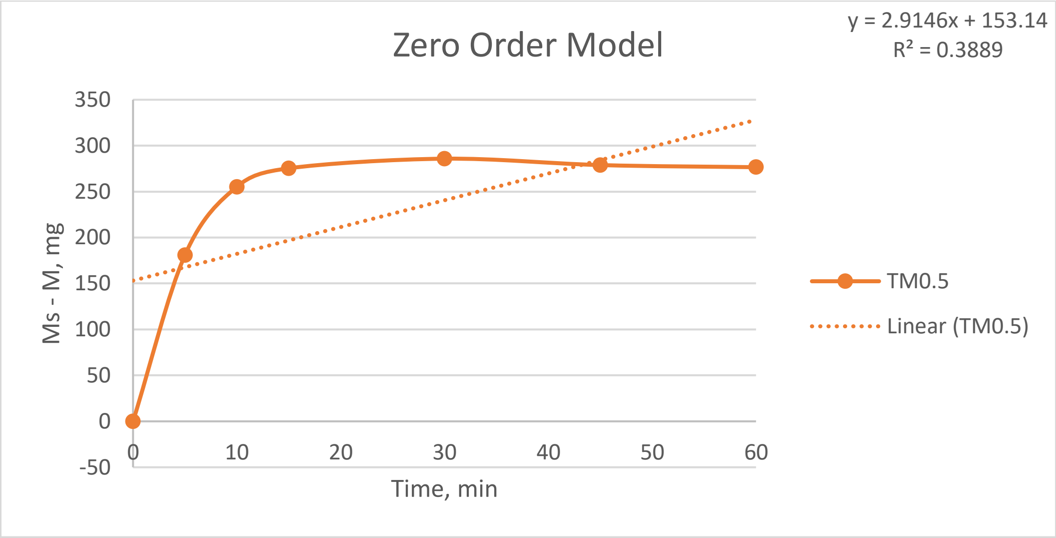

Figure D.3: Zero Order Model TM0.5wt%

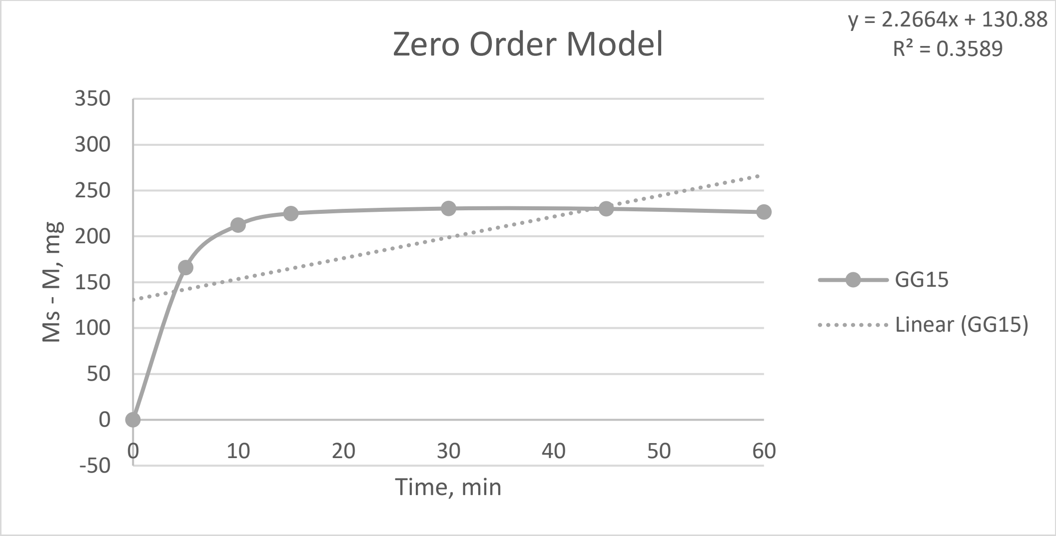

Figure D.4: Zero Order Model GG15

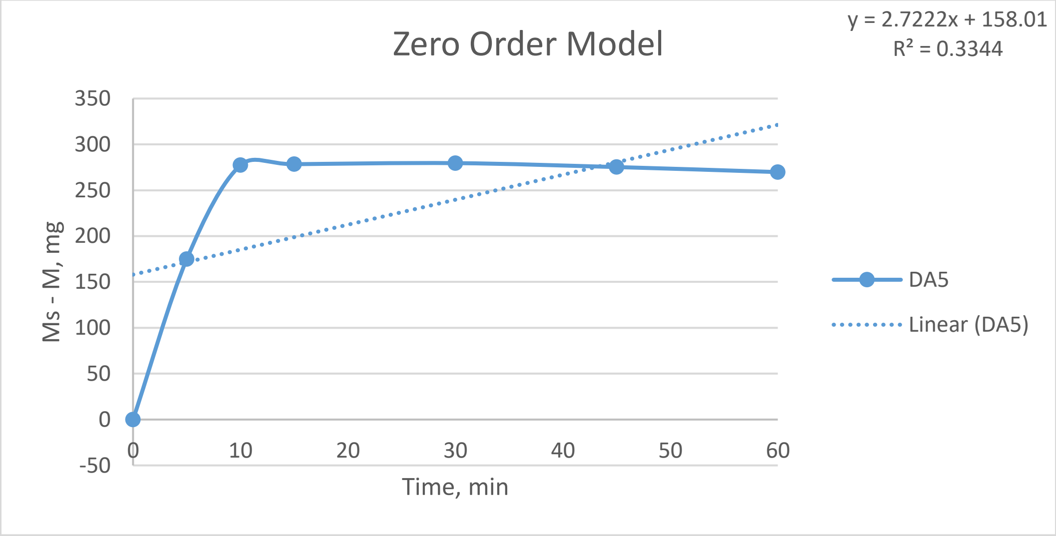

Figure D.5: Zero Order Model DA5

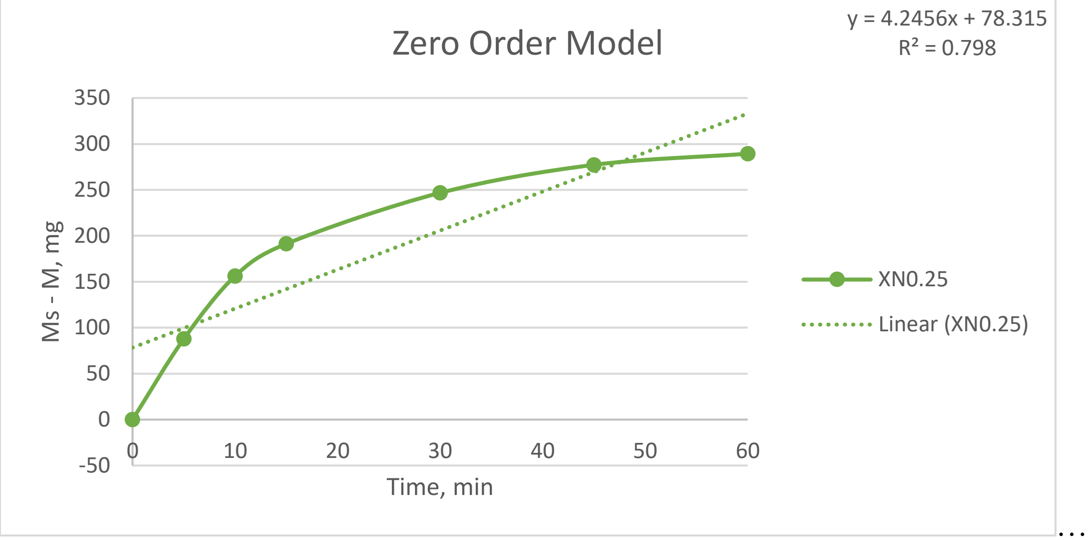

Figure D.6: Zero Order Model XN0.25wt%

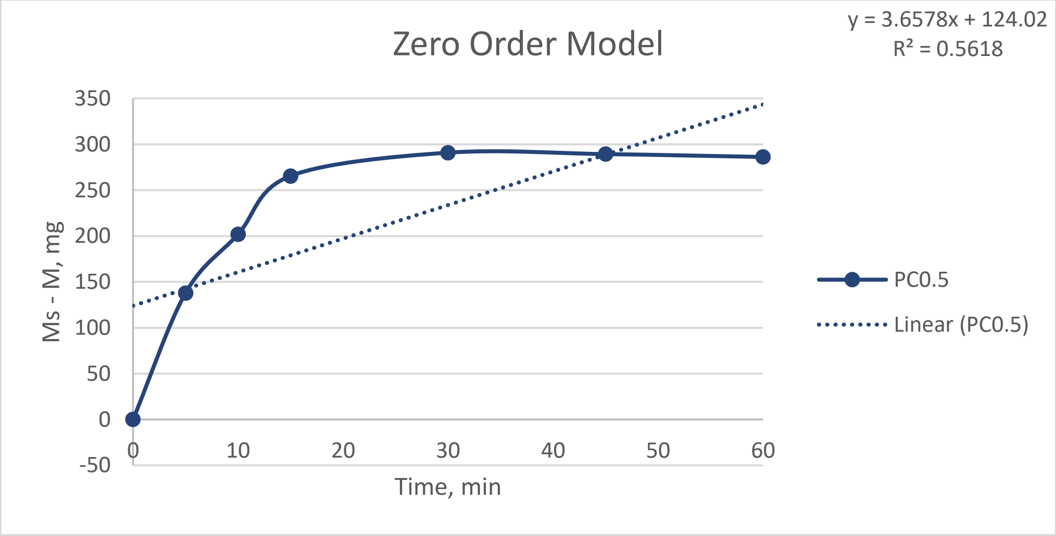

Figure D.7: Zero Order Model PC0.5wt%

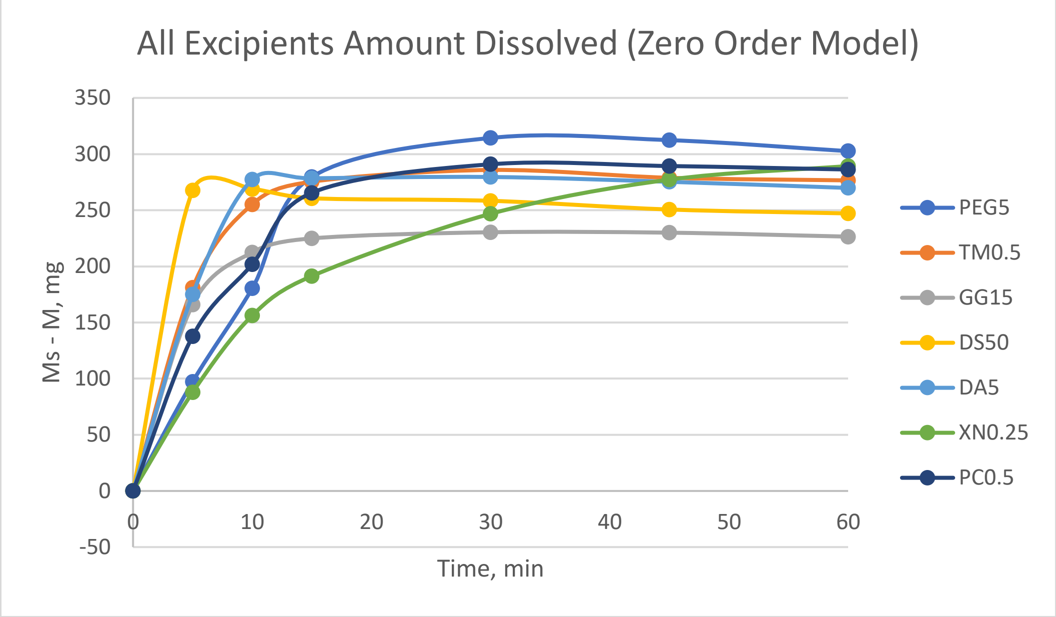

Figure D.8: Zero Order Summary

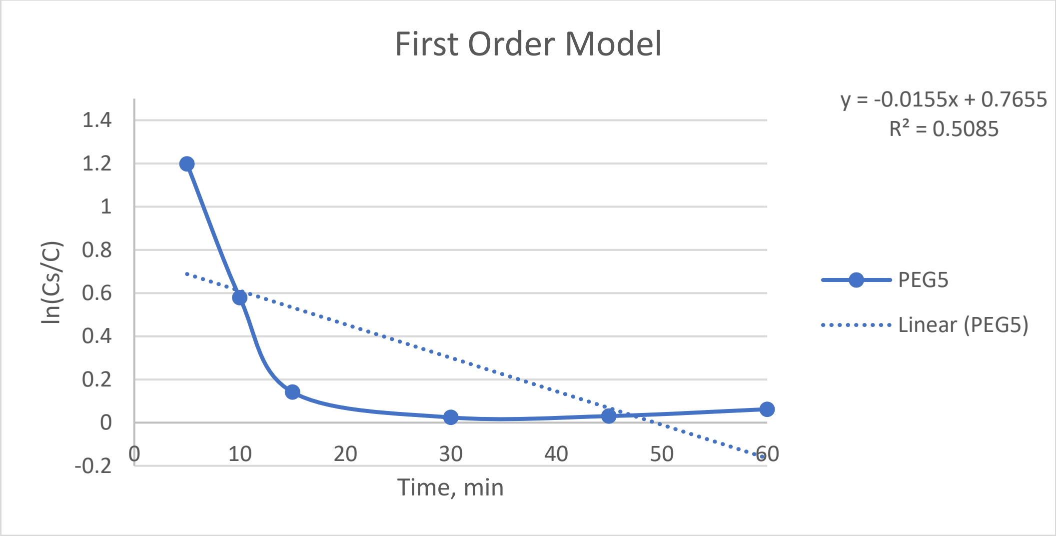

Figure D.9: First Order Model PEG5

Figure D.10: First Order Model DA5

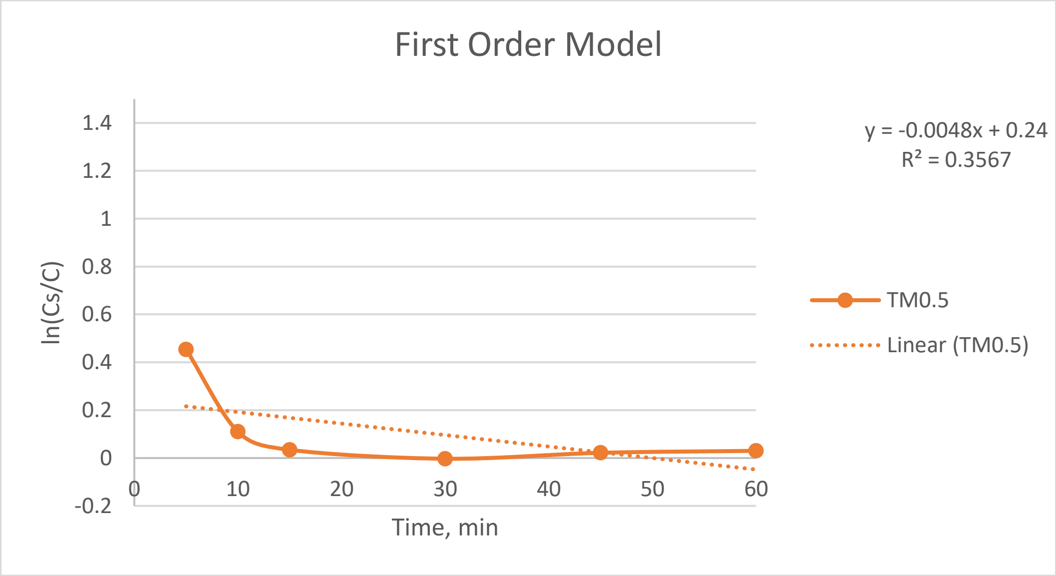

Figure D.11: First Order Model TM0.5wt%

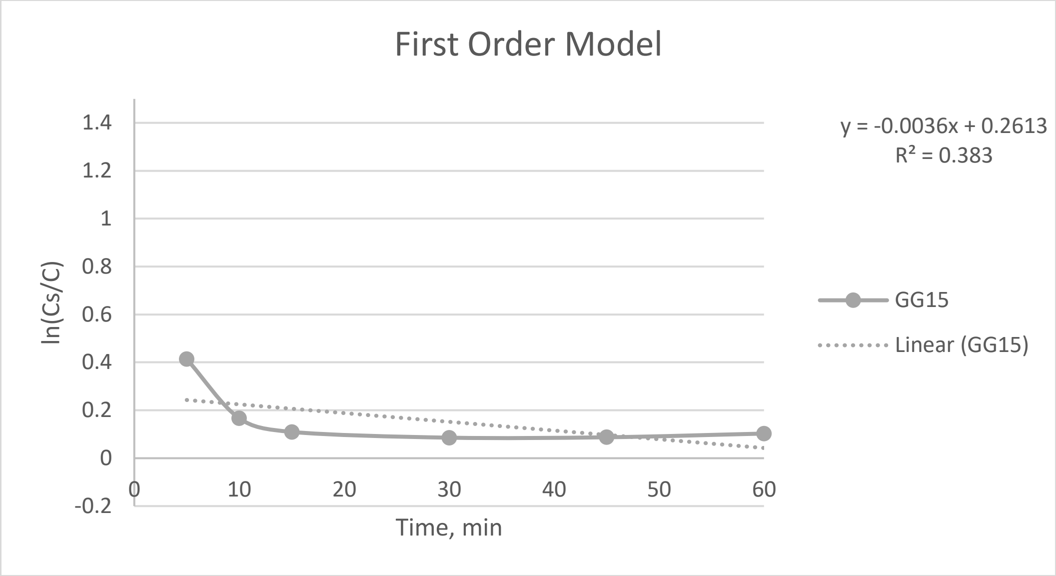

Figure D.12: First Order Model GG15

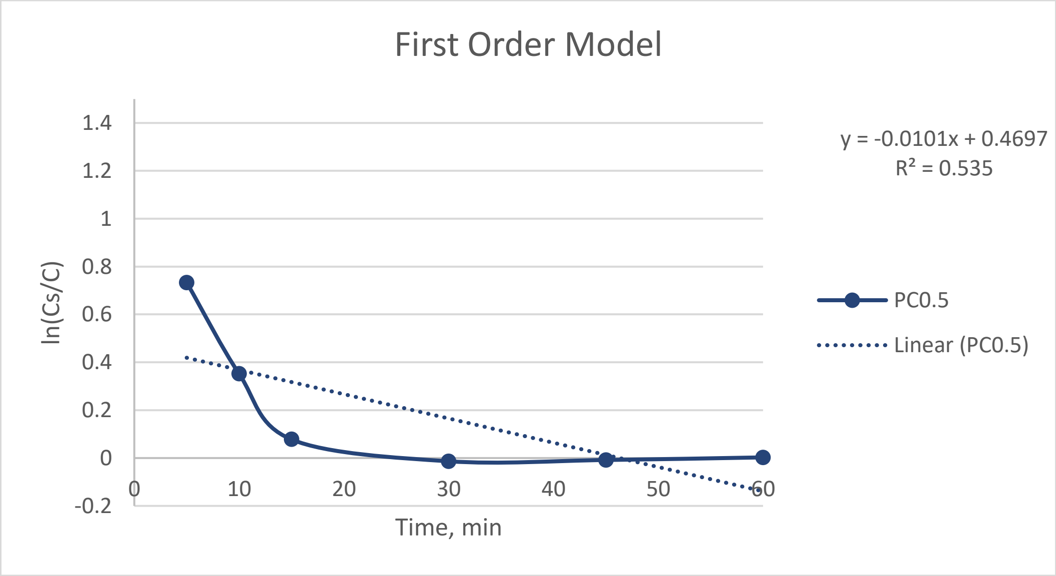

Figure D.13: First Order Model PC0.5wt%

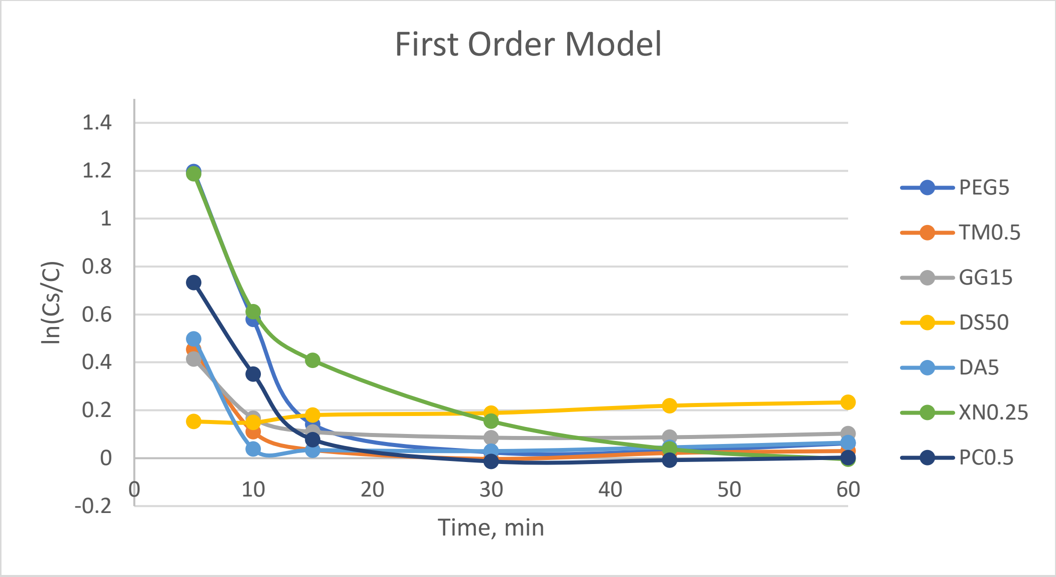

Figure D.14: First-Order Model Summary

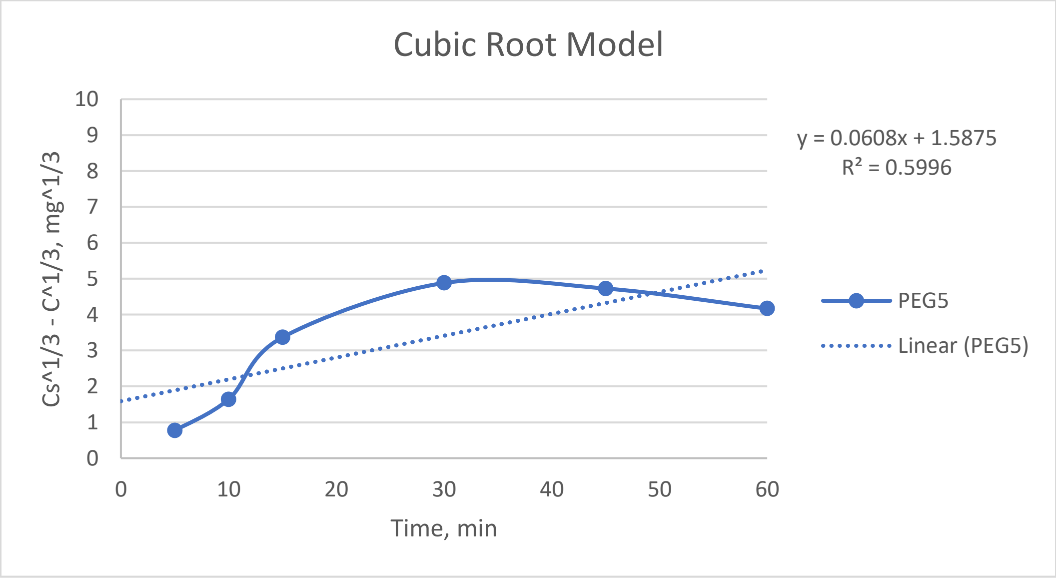

Figure D.15: Cubic Root Model PEG5

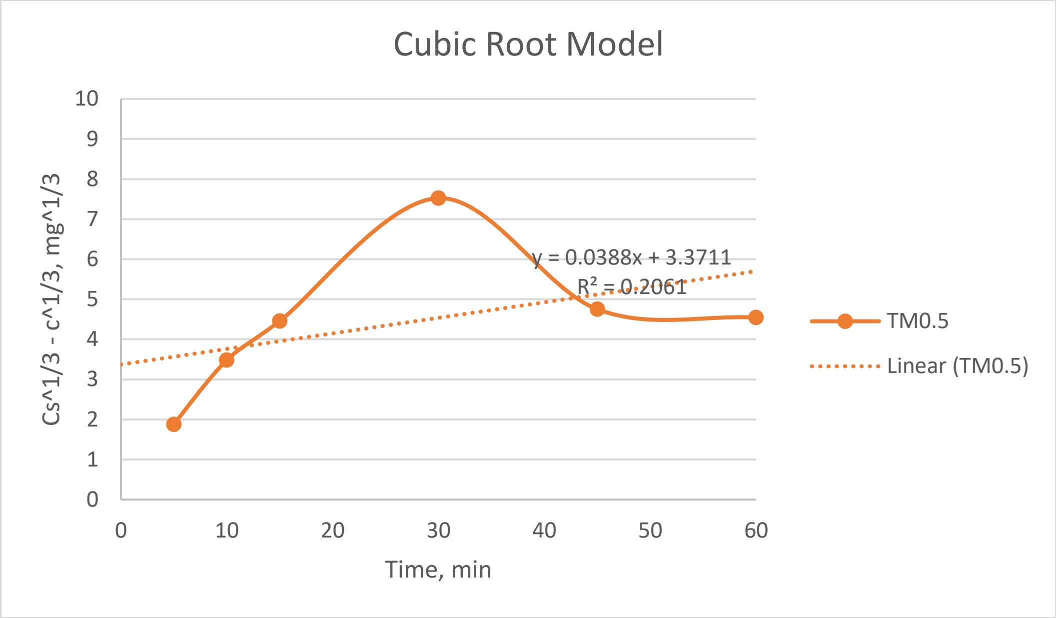

Figure D.16: Cubic Root Model TM0.5wt%

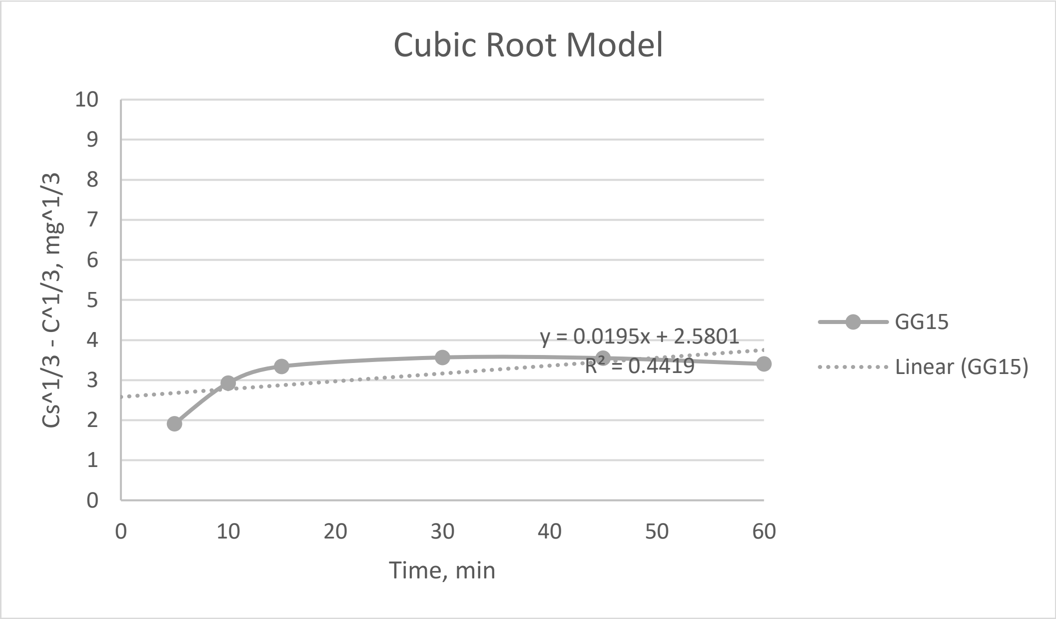

Figure D.17: Cubic Root Model GG15

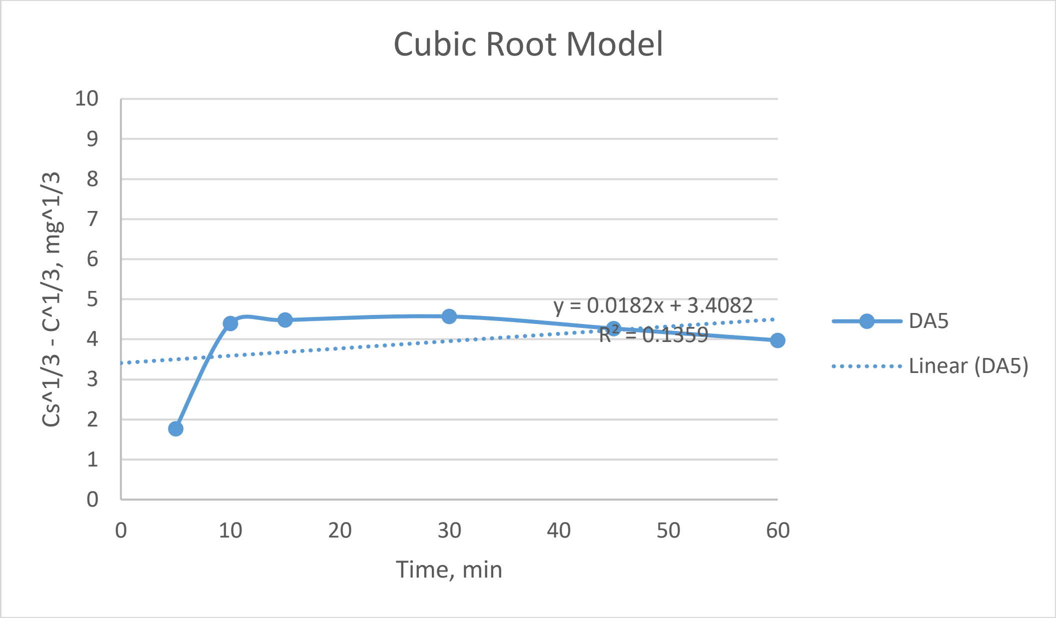

Figure D.18: Cubic Root Model DA5

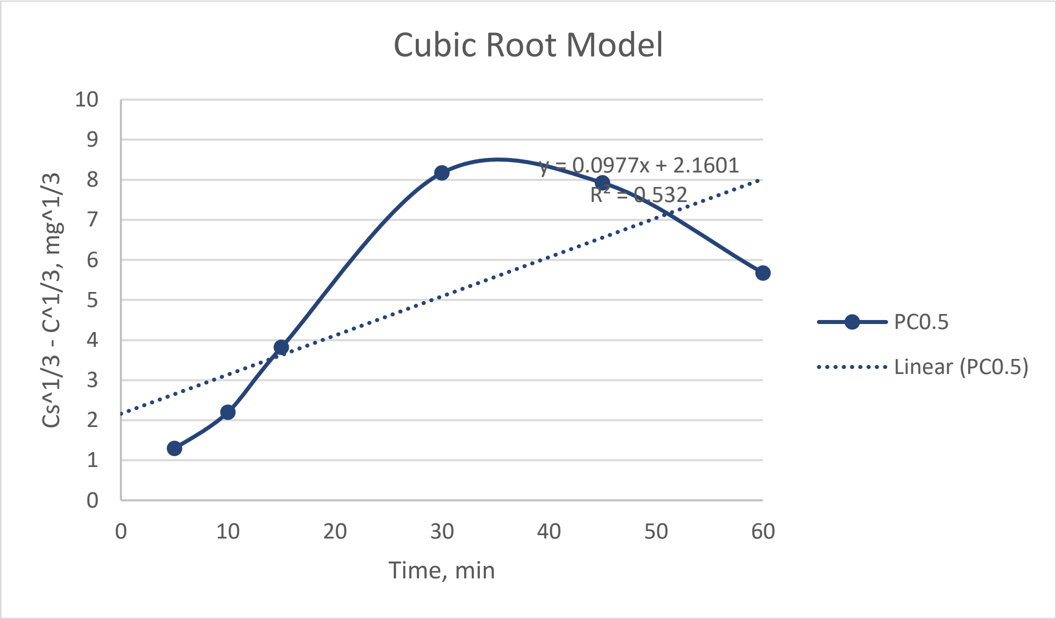

Figure D.19: Cubic Root Model PC0.5wt%

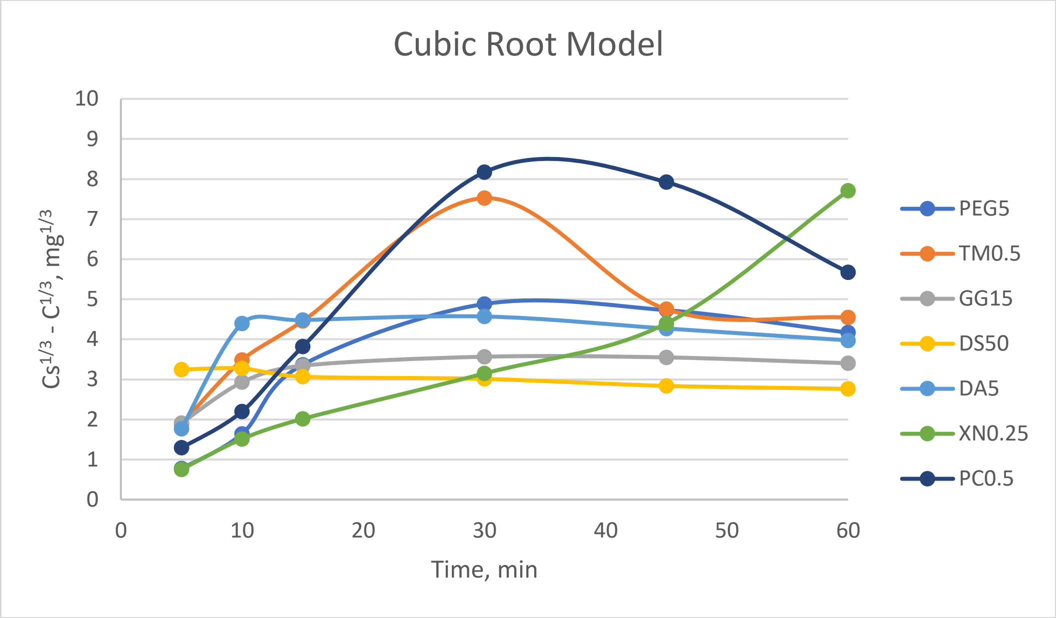

Figure D.20: Cubic Root Model Summary

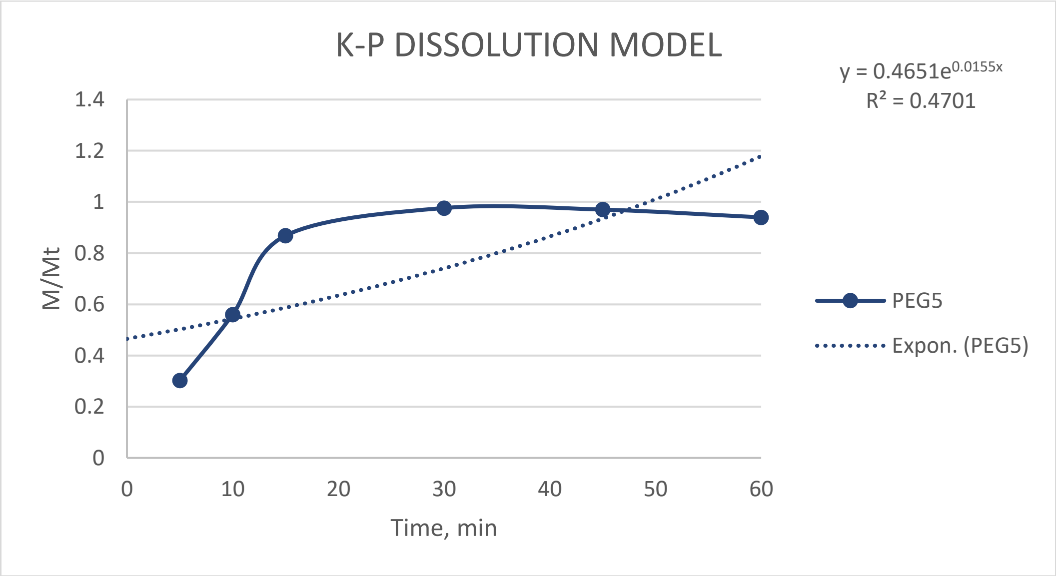

Figure D.21: Korsmeyer-Peppas Model PEG5

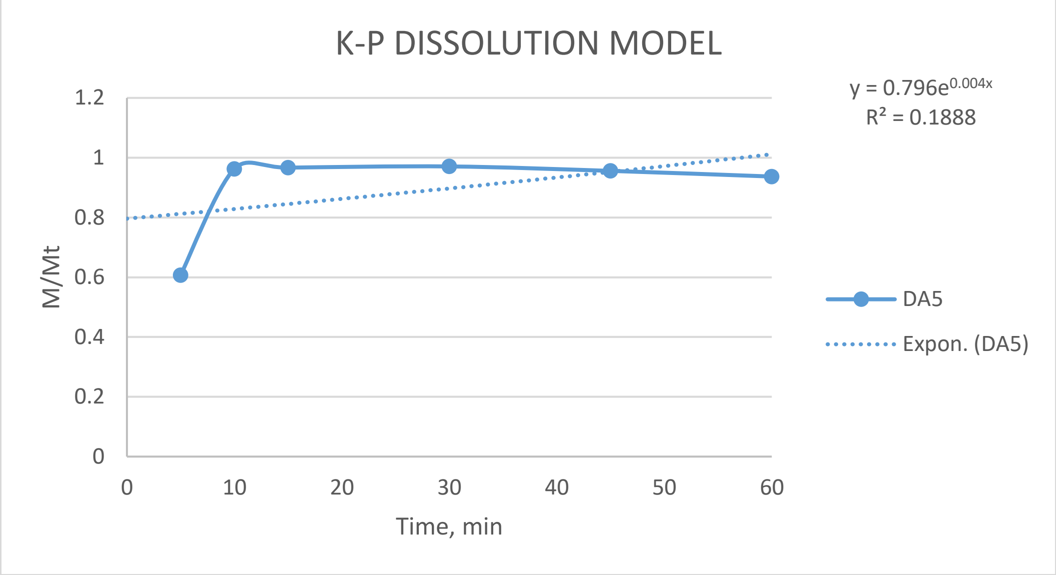

Figure D.22: Korsmeyer-Peppas Model DA5

Figure D.23: Korsmeyer-Peppas Model TM0.5wt%

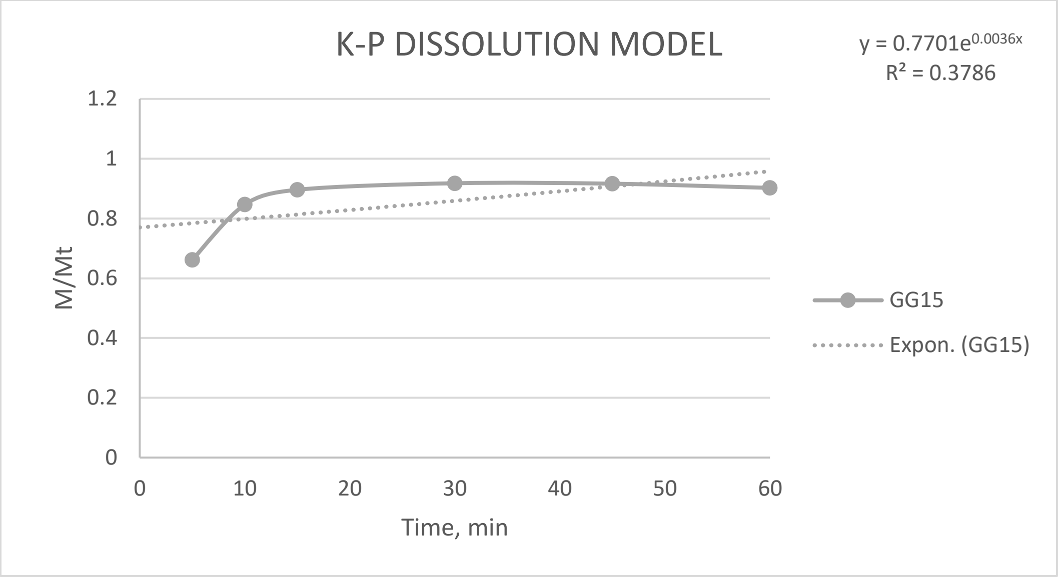

Figure D.24: Korsmeyer-Peppas Model GG15

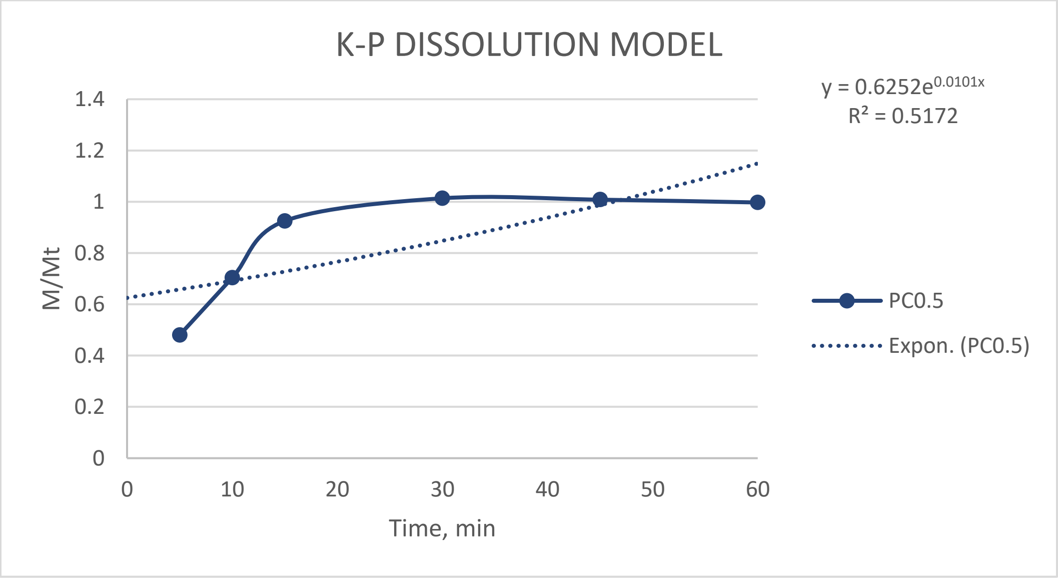

Figure D.25: Korsmeyer-Peppas Model PC0.5wt%

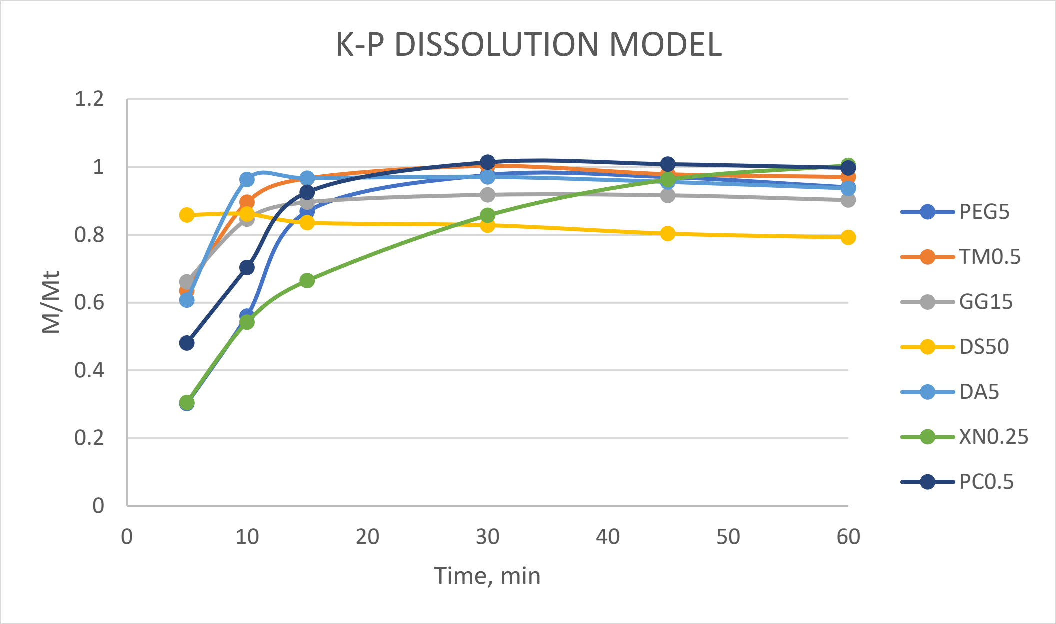

Figure D.26: Korsmeyer-Peppas Model Summary

Appendix E: XRD Scans

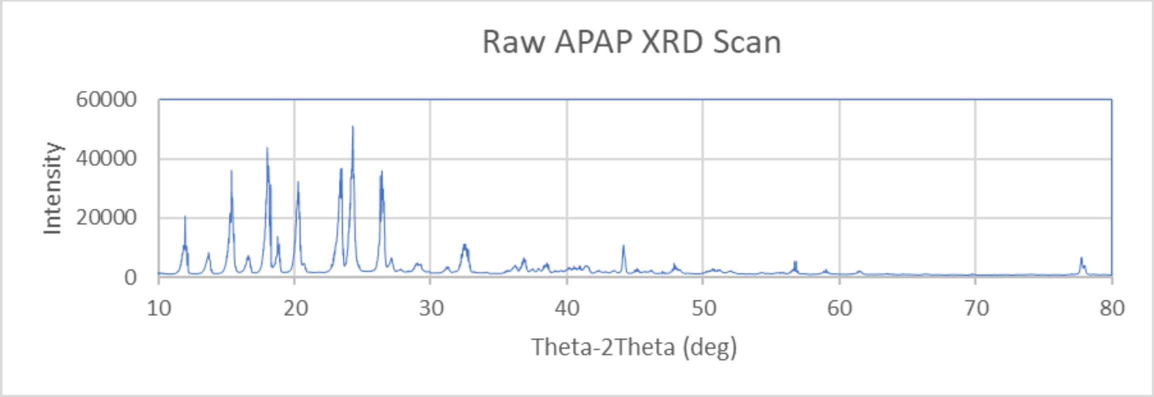

Figure E.1: Raw APAP XRD Scan 10° ≤ 2θ ≤ 80°

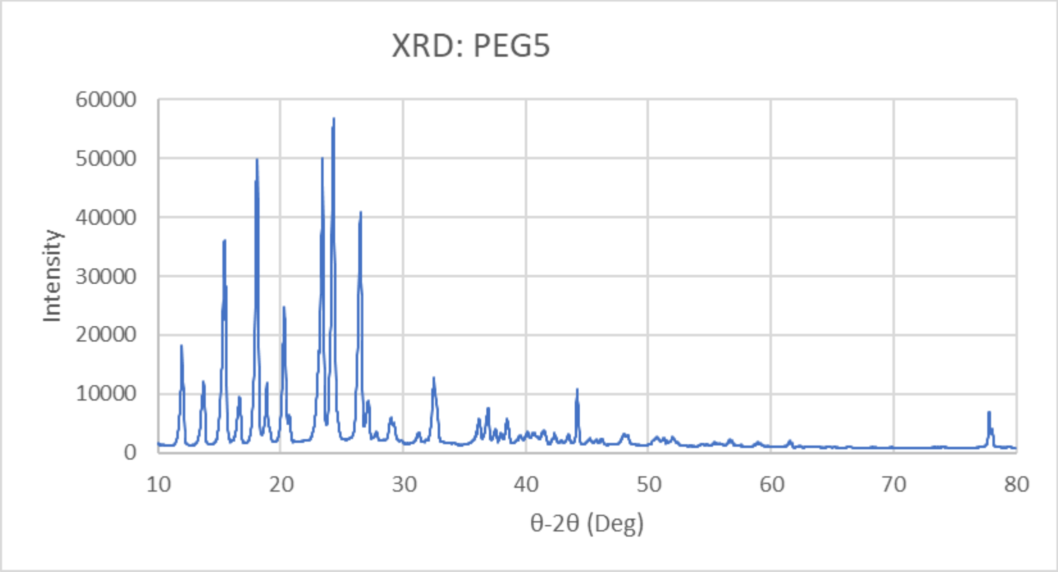

Figure E.2: PEG5 XRD Scan 10° ≤ 2θ ≤ 80°

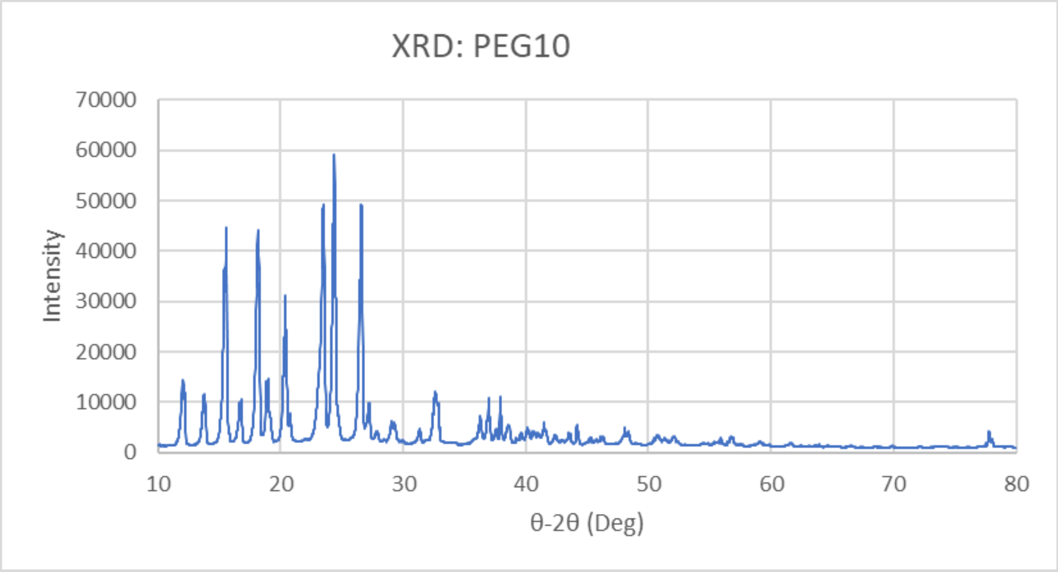

Figure E.3: PEG10 XRD Scan 10° ≤ 2θ ≤ 80°

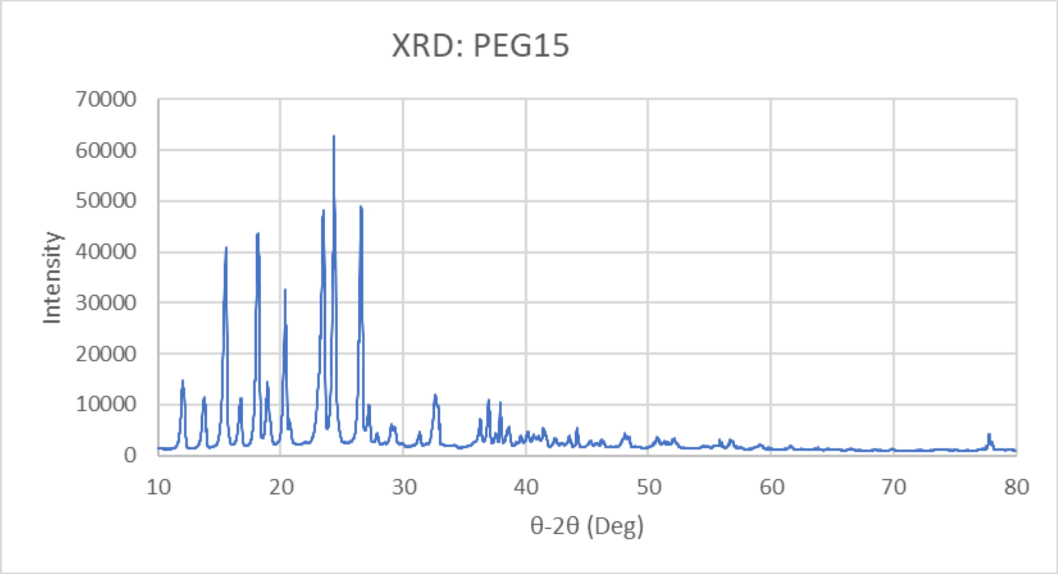

Figure E.4: PEG15 XRD Scan 10° ≤ 2θ ≤ 80°

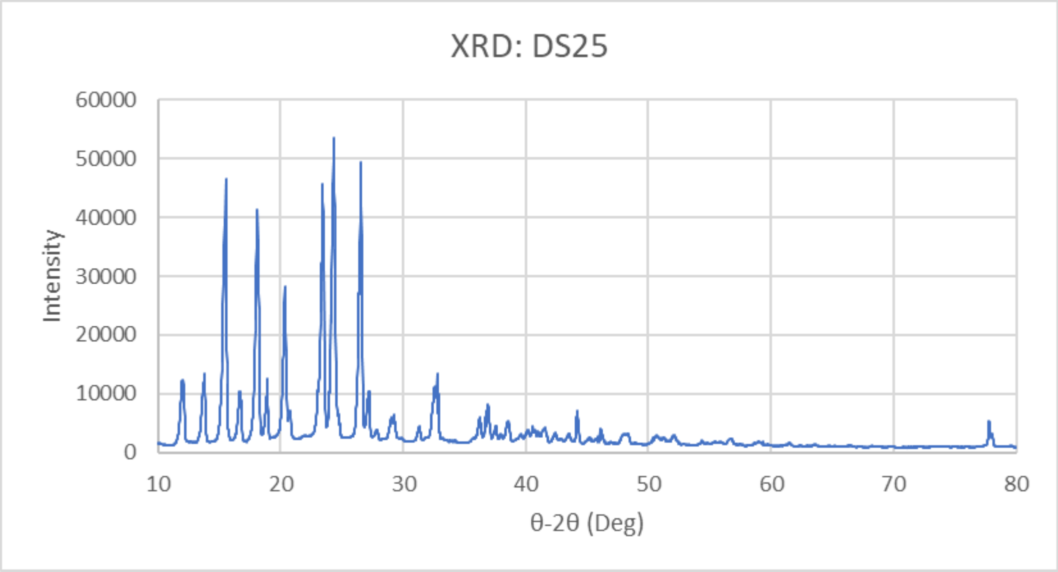

Figure E.5: DS25 XRD Scan 10° ≤ 2θ ≤ 80°

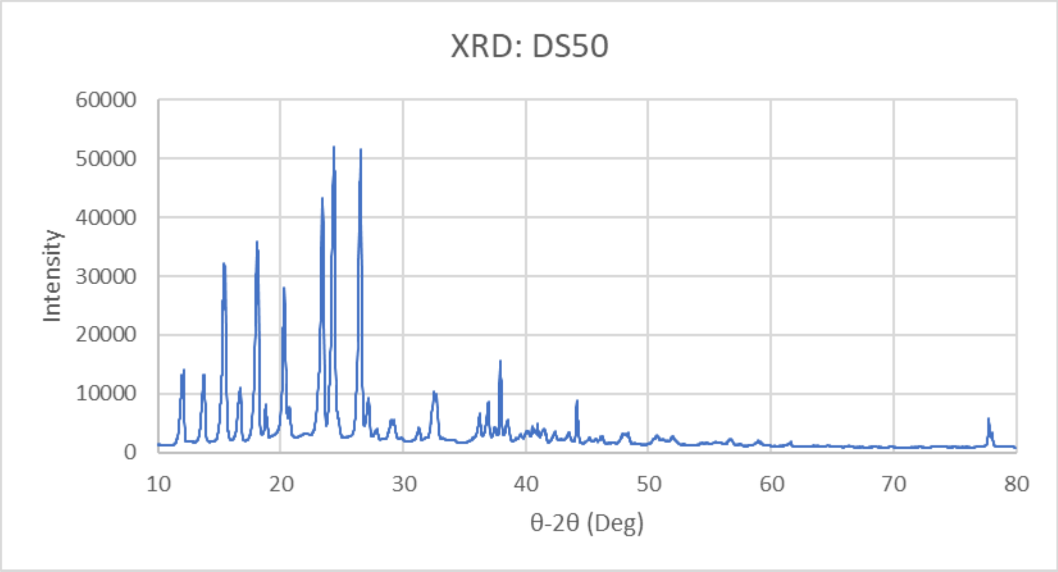

Figure E.6: DS50 XRD Scan 10° ≤ 2θ ≤ 80°

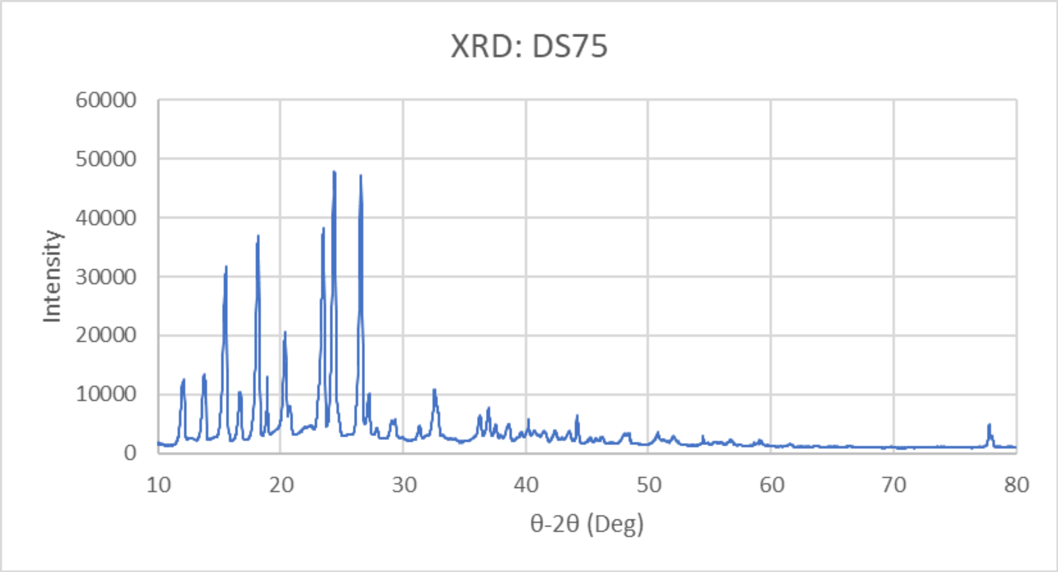

Figure E.7: DS75 XRD Scan 10° ≤ 2θ ≤ 80°

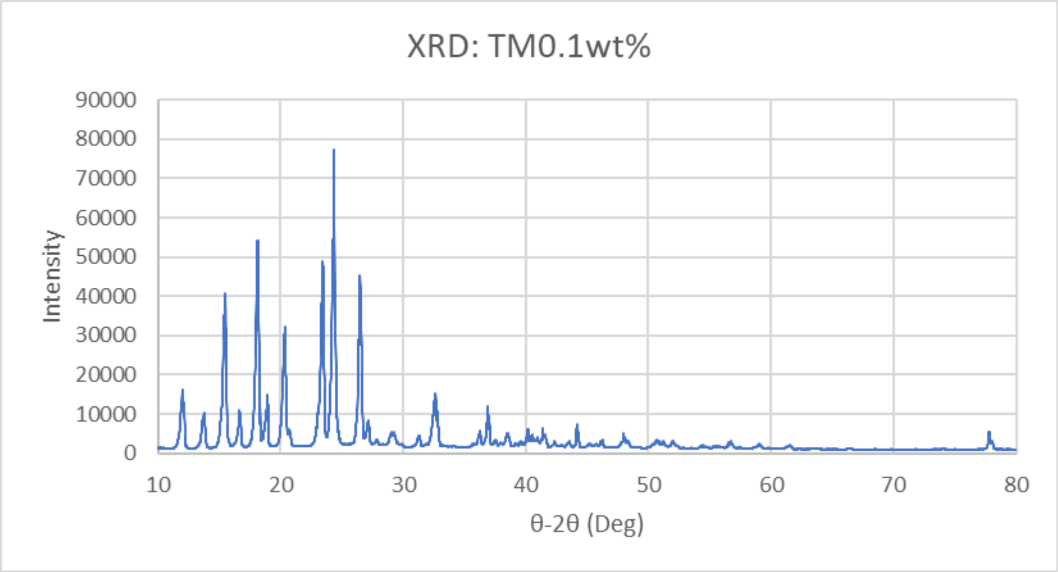

Figure E.8: TM0.1wt% XRD Scan 10° ≤ 2θ ≤ 80°

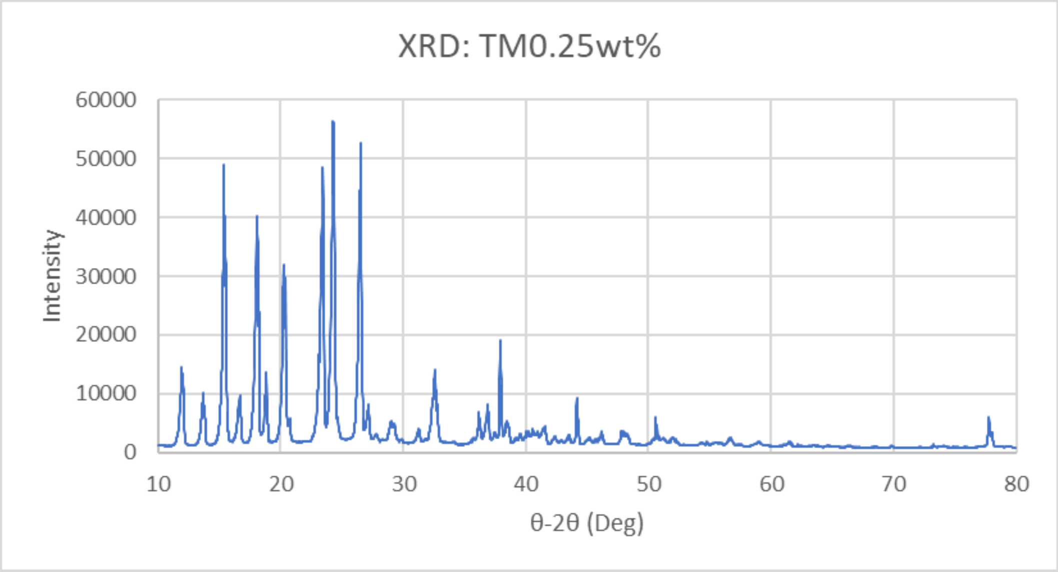

Figure E.9: TM0.25wt% XRD Scan 10° ≤ 2θ ≤ 80°

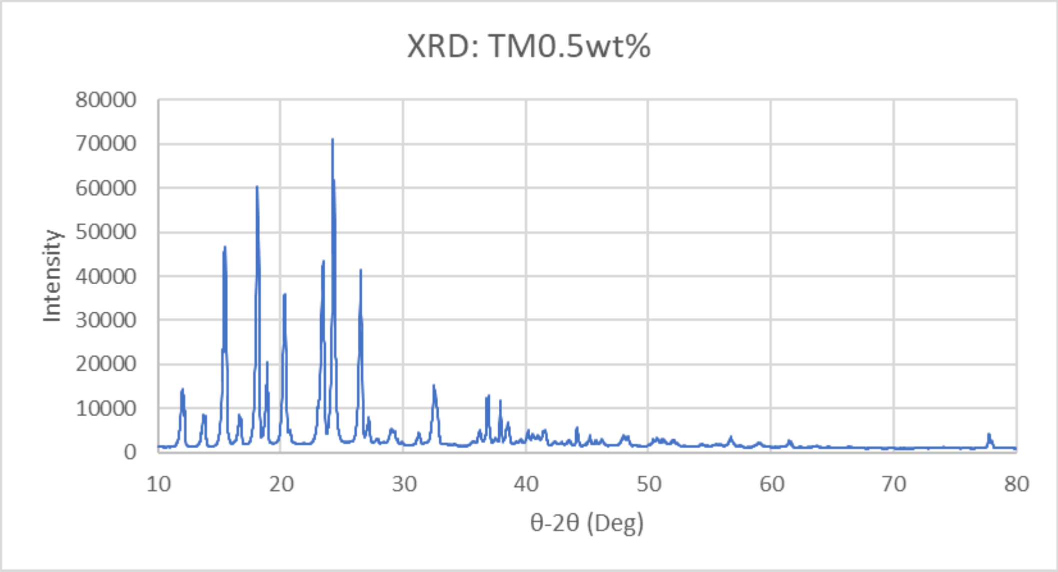

Figure E.10: TM0.5wt% XRD Scan 10° ≤ 2θ ≤ 80°

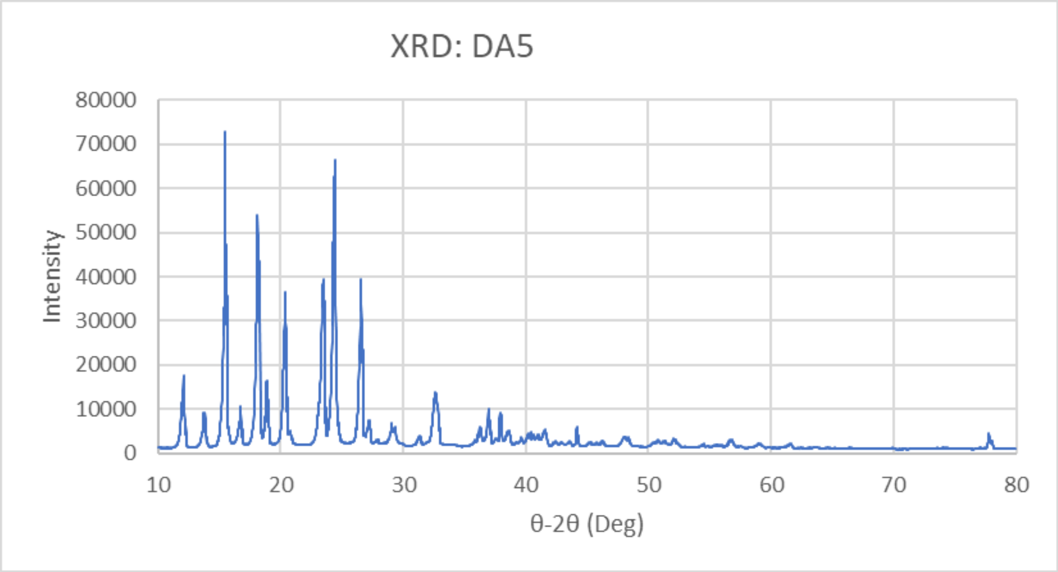

Figure E.11: DA5 XRD Scan 10° ≤ 2θ ≤ 80°

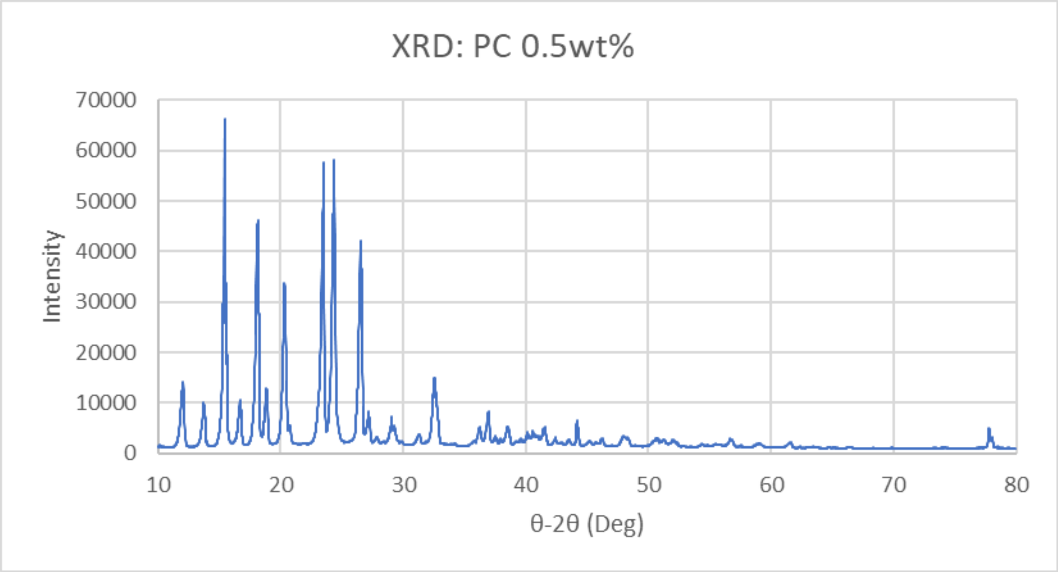

Figure E.12: PC0.5wt% XRD Scan 10° ≤ 2θ ≤ 80°

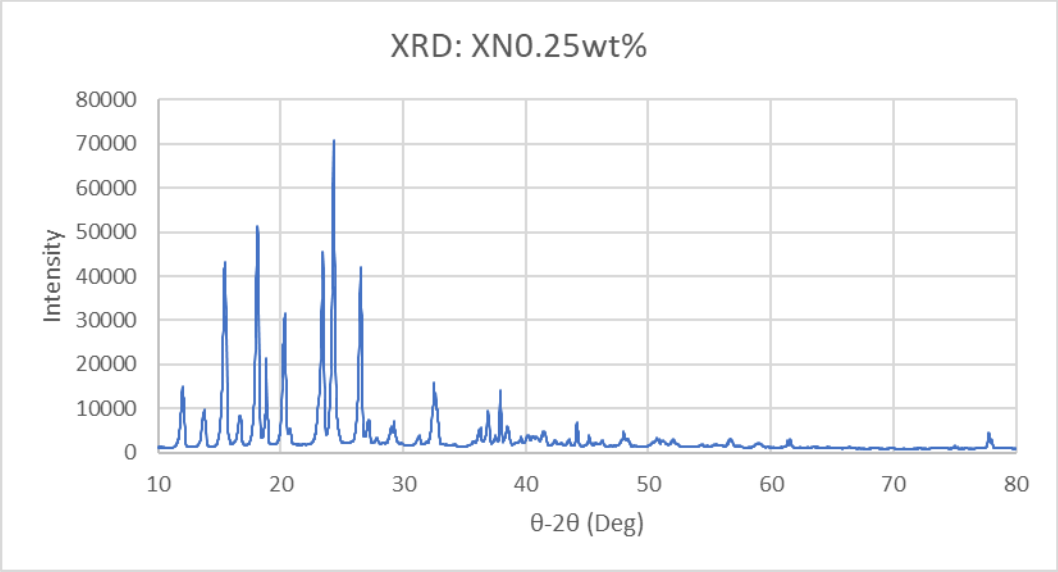

Figure E.13: XN0.25wt% XRD Scan 10° ≤ 2θ ≤ 80°

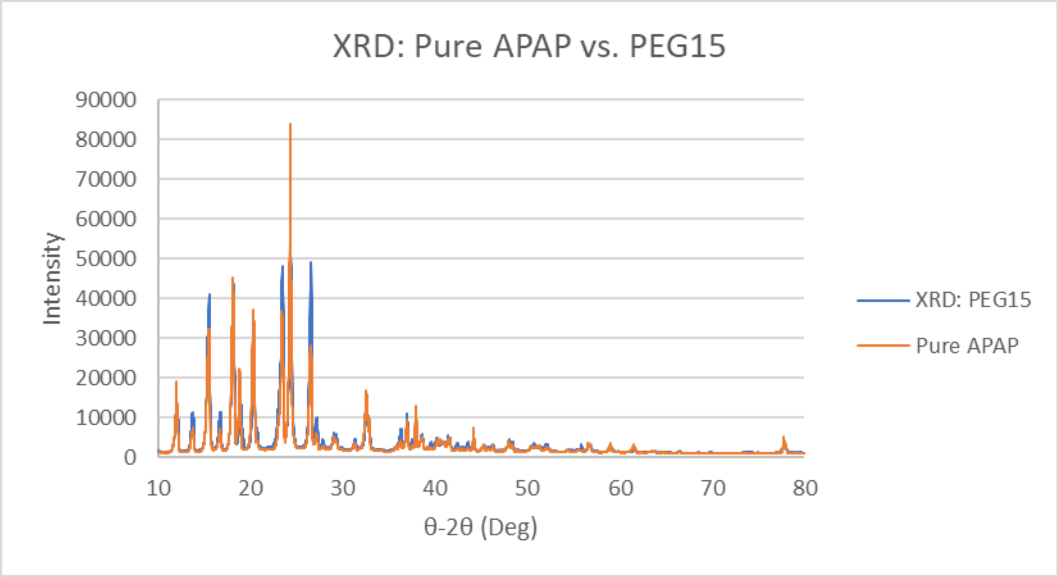

Figure E.14: XRD Raw Scan: PEG15 vs APAP between 10° ≤ 2θ ≤ 80°

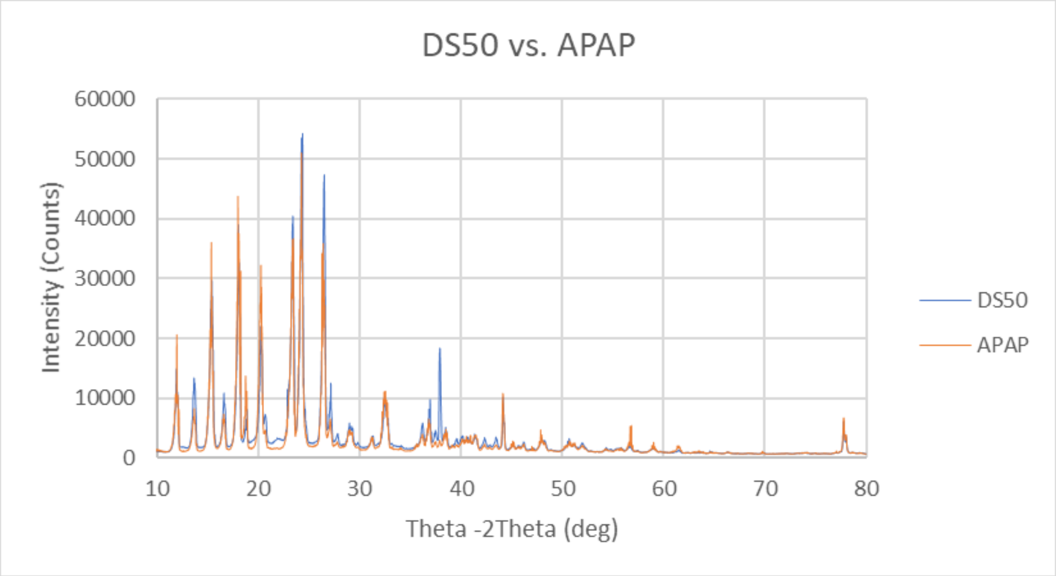

Figure E.15: DS50 vs APAP XRD 10° ≤ 2θ ≤ 80°

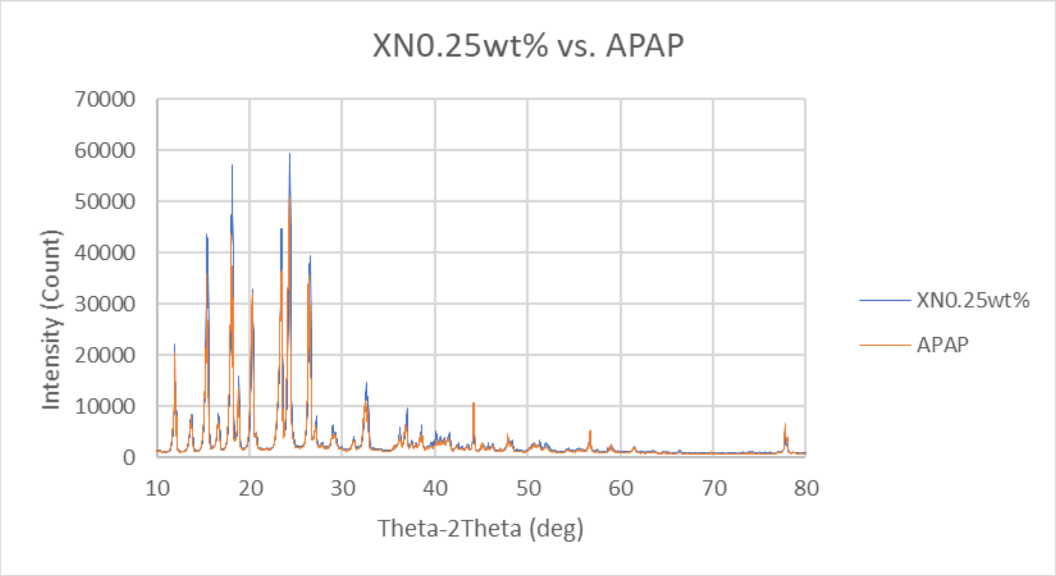

Figure E.16: XRD Raw Scan: XN0.25wt% vs APAP between 10° ≤ 2θ ≤ 80°

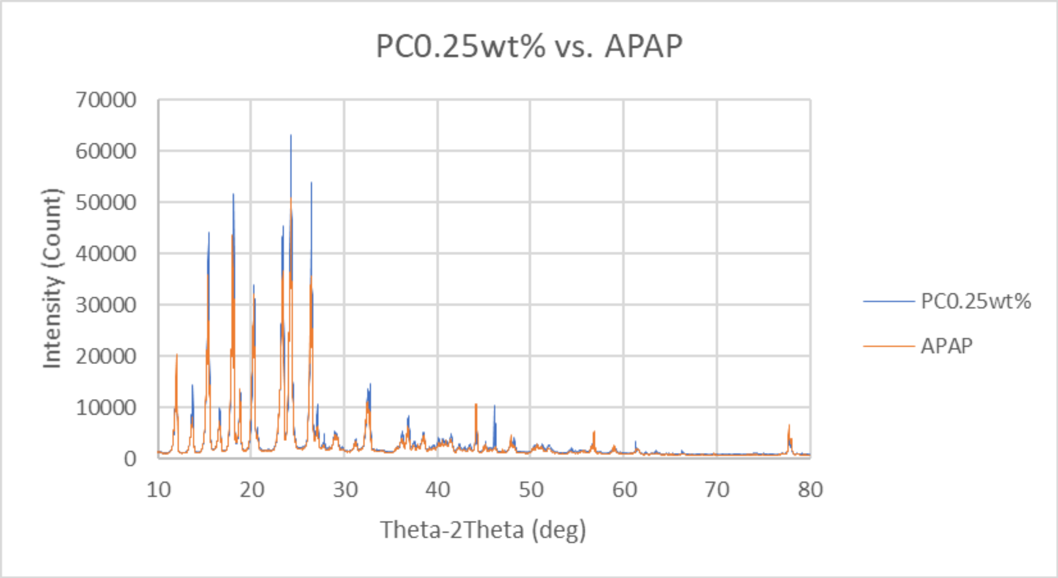

Figure E.17: XRD Raw Scan: PC0.25wt% vs APAP between 10° ≤ 2θ ≤ 80°

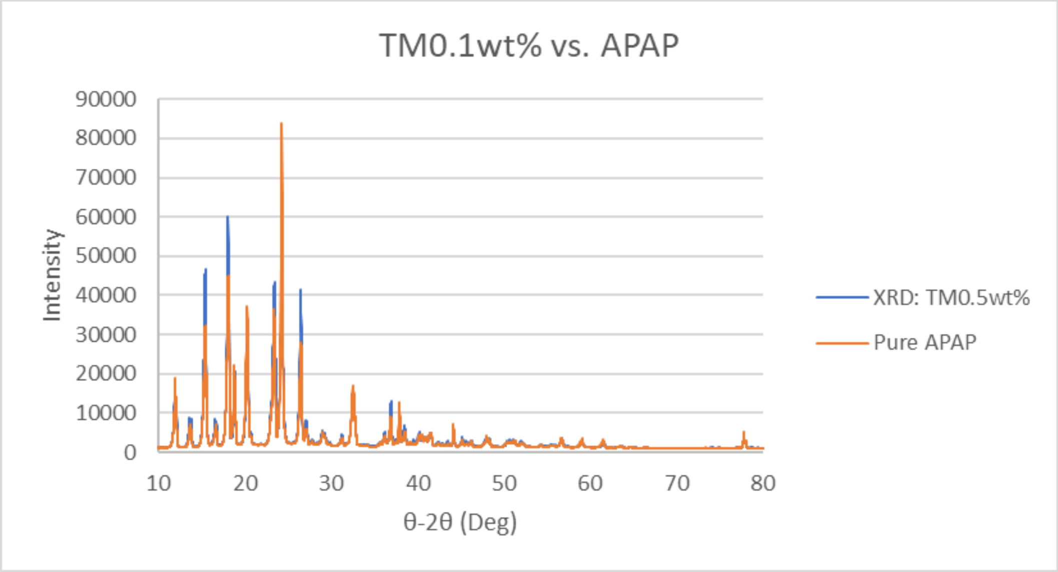

Figure E.18: XRD Raw Scan: TM0.5wt% vs APAP between 10° ≤ 2θ ≤ 80

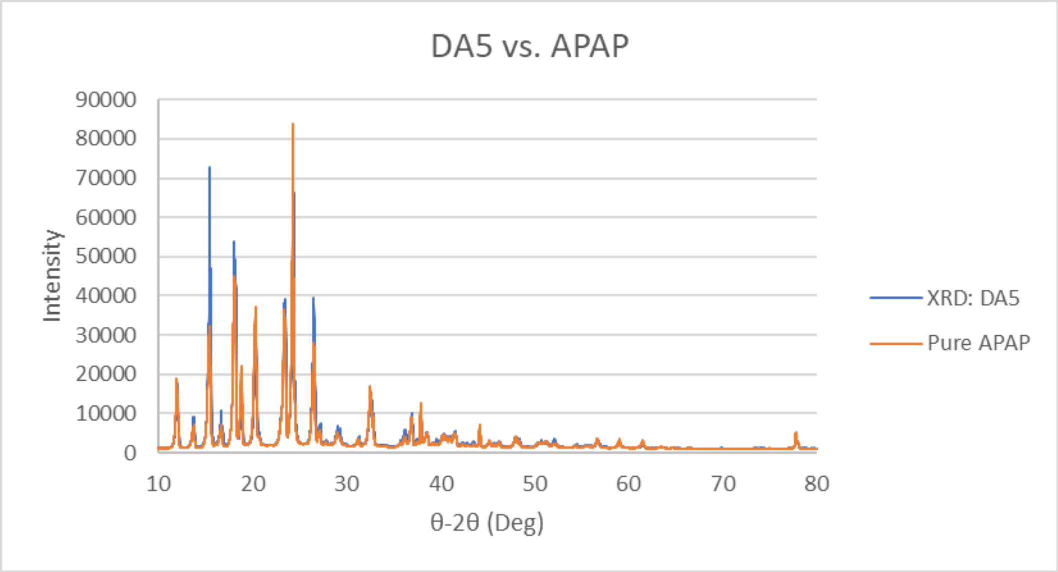

Figure E.19: XRD Raw Scan: DA5 vs APAP between 10° ≤ 2θ ≤ 80°

Table E.1: XRD Sample Peak Comparison

Compound	APAP	DS50			TM			PEG		
Weight %	APAP	4.33wt%	8.67wt%	13wt%	0.1wt%	0.25wt%	0.5wt%	3wt%	6wt%	9wt%
Peak Locations	12.09	12.07	12.06	12.10	12.07	12.04	12.09	12.04	12.12	12.12
	13.81	13.79	13.78	13.83	13.79	13.76	13.81	13.76	13.83	13.83
	15.52	15.50	15.47	15.52	15.50	15.48	15.52	15.47	15.54	15.54
	16.74	16.73	16.71	16.75	16.72	16.69	16.74	16.69	16.77	16.77
	18.18	18.16	18.14	18.19	18.16	18.13	18.19	18.12	18.20	18.20
	18.91	18.92	18.87	18.97	18.91	18.86	18.93	18.91	18.99	19.00
	20.37	20.38	20.35	20.41	20.36	20.34	20.38	20.34	20.42	20.43
	20.81	20.78	20.78	20.77	20.78	20.77	20.78	20.75	20.85	20.83
	23.08	23.01	23.00	23.06	22.91	23.06	23.03	22.81	22.95	22.98
	23.48	23.46	23.45	23.49	23.45	23.44	23.48	23.43	23.49	23.50
	24.36	24.35	24.34	24.39	24.36	24.32	24.37	24.32	24.40	24.40
	26.56	26.55	26.52	26.57	26.53	26.52	26.56	26.51	26.58	26.58
	27.20	27.17	27.16	27.20	27.16	27.15	27.19	27.12	27.21	27.21
	29.07	29.08	29.06	29.10	29.01	29.04	29.07	29.02	29.10	29.10
	29.31	29.32	29.31	29.35	29.28	29.29	29.31	29.27	29.35	29.34

Table E.2 Peak Comparison DA, GG, PC, and XN

Compound	**DA**	**GG**	**PC**	**XN**
Weight %	13.86wt%	0.36wt%	0.5wt%	0.25wt%
Peak Locations	12.11	12.11	12.08	12.07
	13.85	13.83	13.80	13.79
	15.57	15.54	15.50	15.50
	16.76	16.76	16.73	16.72
	18.22	18.21	18.17	18.15
	18.95	18.97	18.90	18.90
	20.41	20.40	20.37	20.35
	20.89	20.83	20.79	20.82
	23.03	23.04	23.03	23.03
	23.50	23.48	23.48	23.46
	24.41	24.39	24.36	24.36
	26.59	26.57	26.55	26.54
	27.24	27.22	27.18	27.17
	29.07	29.09	29.06	29.04
	29.33	29.37	29.32	29.31

Appendix F: Tablet Saturation and Weight Comparison

Table F.1 Tablet Saturation and Weight % Equivalent

Excipient Saturation	Weight Percent
PEG5	PEG 3.0wt%
PEG10	PEG 6.0wt%
PEG15	PEG 9.0wt%
DS25	DS 4.3wt%
DS50	DS 8.7wt%
DS75	DS 13.0wt%
DA5	DA 13.86wt%
GG15 (WAC)	GG 0.36wt%